

# Low-frequency inter-ELM pedestal modes at ASDEX upgrade

**Citation for published version (APA):**

Vanovac, B. (2019). *Low-frequency inter-ELM pedestal modes at ASDEX upgrade*. [Phd Thesis 1 (Research TU/e / Graduation TU/e), Applied Physics and Science Education]. Technische Universiteit Eindhoven.

**Document status and date:**

Published: 30/01/2019

**Document Version:**

Publisher's PDF, also known as Version of Record (includes final page, issue and volume numbers)

**Please check the document version of this publication:**

- A submitted manuscript is the version of the article upon submission and before peer-review. There can be important differences between the submitted version and the official published version of record. People interested in the research are advised to contact the author for the final version of the publication, or visit the DOI to the publisher's website.
- The final author version and the galley proof are versions of the publication after peer review.
- The final published version features the final layout of the paper including the volume, issue and page numbers.

[Link to publication](#)

**General rights**

Copyright and moral rights for the publications made accessible in the public portal are retained by the authors and/or other copyright owners and it is a condition of accessing publications that users recognise and abide by the legal requirements associated with these rights.

- Users may download and print one copy of any publication from the public portal for the purpose of private study or research.
- You may not further distribute the material or use it for any profit-making activity or commercial gain
- You may freely distribute the URL identifying the publication in the public portal.

If the publication is distributed under the terms of Article 25fa of the Dutch Copyright Act, indicated by the "Taverne" license above, please follow below link for the End User Agreement:

[www.tue.nl/taverne](http://www.tue.nl/taverne)

**Take down policy**

If you believe that this document breaches copyright please contact us at:

[openaccess@tue.nl](mailto:openaccess@tue.nl)

providing details and we will investigate your claim.

# **Low-frequency inter-ELM pedestal modes at ASDEX Upgrade**

Branka Vanovac



DIFFER is part of the institutes organisation of NWO. This work has been carried out within the framework of the EUROfusion Consortium and has received funding from the Euratom research and training programme 2014-2018 and 2019-2020 under grant agreement No 633053. The views and opinions expressed herein do not necessarily reflect those of the European Commission.

A catalogue record is available from the Eindhoven University of Technology Library  
ISBN: 978-90-386-4687-9

*Cover page designed by B. Vanovac. It shows the data from AUG shot # 33616. Front cover displays time resolved measurements of ECEI channels vertically distributed along a single flux surface and a cross-correlation with reference channel. In this way the poloidal mode velocities, mode structure and mode propagation direction are assessed. Modified from figure 5.8. Back cover depicts poloidally distributed channels calculated with radiation transport forward model and are shown in this dissertation in figure 5.7.*

©2018 by Branka Vanovac. All right reserved.

# **Low-frequency inter-ELM pedestal modes at ASDEX Upgrade**

PROEFSCHRIFT

ter verkrijging van de graad van doctor aan de Technische Universiteit Eindhoven,  
op gezag van de rector magnificus prof.dr.ir. F.P.T. Baaijens, voor een commissie  
aangewezen door het College voor Promoties, in het openbaar te verdedigen op  
donderdag 30 januari 2019 om 16:00 uur

door

**Branka Vanovac**

geboren te Zenica, Bosnië-Herzegovina



Dit proefschrift is goedgekeurd door de promotoren en de samenstelling van de promotiecommissie is als volgt:

Voorzitter: prof. dr. ir. G. M. W. Kroesen  
Promotor: prof. dr. A. J. H. Donné (TU/e, EUROfusion, Garching, DE)  
1e copromotor: dr. E. Wolfrum (IPP, Garching, DE)  
2e copromotor: dr. H. J. de Blank (DIFFER, Eindhoven, NL)  
leden: prof. dr. P. Hennequin (LPP, Palaiseau, FR)  
prof. dr. ir. G. T. A. Huijsmans (TU/e, CEA-IRFM, Cadarache, FR)  
prof. dr. M. R. de Baar (TU/e, DIFFER, Eindhoven, NL)  
dr. B. Dudson (Univ. of York, UK)

Het onderzoek of ontwerp dat in dit proefschrift wordt beschreven is uitgevoerd in overeenstemming met de TU/e Gedragscode Wetenschapsbeoefening.

Ground Control to Major Tom  
Ground Control to Major Tom  
Take your protein pills  
and put your helmet on  
Ground Control to Major Tom  
commencing countdown, engines on  
Check ignition  
and may God's love be with you....

*Space Oddity, David Bowie*



# Summary

## **Low-frequency inter-ELM pedestal modes at ASDEX Upgrade**

A promising long-term energy solution is the realization of steady state nuclear fusion under terrestrial conditions. For doing so, the fusion fuel is heated up to more than 100 million degrees required for the fusion reactions and at the same time this fusion fuel has to be confined for sufficiently long time. As at such high temperatures, the electrons are completely stripped from their nuclei, the gas is in the plasma state. In magnetically confined fusion (MCF) those charged particles are confined via magnetic fields and gyrate around the magnetic field lines in a toroidally shaped vessel.

To achieve fusion gain, high pressure in the plasma core has to be achieved. This is realized by heating the plasma above certain threshold after which plasma naturally enters into the regime of high confinement, the so-called H-mode. This mode of operation is characterized by the formation of Edge Transport Barrier, which as its name suggests, is a pure edge effect and occurs in the last few centimetres of the confined region. As the formation of the Edge Transport Barrier reduces the transport, the edge pressure profile builds up in the form of the pedestal thus increasing the core pressure.

The pedestal pressure values are limited by the appearance of large MHD instabilities. Once the critical pressure value is achieved modes become unstable allowing heat and particles to be transported across the field lines towards the wall. These events are called Edge Localized Modes (ELMs). Edge Localized Modes are an intermittent instability affecting the plasma edge in tokamaks. They can cause a sudden loss between 5 to 30 % of the plasma stored energy. This outburst of heat and particles

across the separatrix is preceded by a variety of turbulent and MHD instabilities localized in the narrow pedestal region determining the transport in the edge. Instabilities appear in the form of inter-ELM modes, and precursors, both having a distinct signature regarding toroidal and poloidal structure, amplitude, location, and velocity. To understand the transport caused by the inter-ELM modes as well as the ELM triggering mechanisms, the characterization of these inter-ELM modes as well as the conditions under which they develop, are essential.

The work presented in this thesis focuses on the exploration of the inter-ELM modes appearing in the low-frequency part of the spectrum ( $\sim 10$  kHz). At the ASDEX Upgrade tokamak, a variety of edge diagnostics are exploited to access the characteristics of the mode. The particular focus lies on the Electron Cyclotron Emission Imaging (ECEI) diagnostic that measures the electron temperature fluctuations. It delivers information on the spatial structure and mode velocity due to its excellent poloidal resolution. The final upgrade and commissioning of the ECEI diagnostic has been performed during this thesis work. With an additional array, toroidally separated by about  $\sim 40$  cm from the first one, the system's lines of sight are oblique to the magnetic field lines. With such a geometry, the Doppler shift- and relativistic broadening are enhanced. These effects degrade the radial resolution of the diagnostic and because of the narrow pedestal, interpretation of the measurements is not unambiguous. The diagnostic response is evaluated with an electron cyclotron radiation transport forward model and shows a Doppler shift of about 1.5 cm for channels resonant inside the separatrix due to the toroidal observation angle. The channels resonant in the scrape-off layer region are mostly affected by a relativistic down-shift; hence the so-called 'shine-through' effect is dominant outside the separatrix. Additionally, it is shown that the presence of density fluctuations in the pedestal alters the channel's position. In the steep gradient region, a small change in position means a significant change in amplitude. Hence the ECEI measurements can be solely affected by the density. Thus, the forward model together with knowledge of the density fluctuation amplitude is necessary to assess the electron temperature fluctuations associated with inter-ELM modes.

In the phase between ELMs a mode appearing in the range of 2-14 kHz dominates the ECEI measurements within the majority of the H-mode discharges analyzed in this work. The mode has been characterized with high accuracy. It appears in the

electron density and temperature, and causes perturbations in the radial magnetic field, simultaneously. The toroidal mode number spans between 11-14. The mode is located in the upper part of the steep gradient region and rotates with the  $E \times B$  velocity in the electron diamagnetic direction. Its phase velocity cannot be resolved within the measurement uncertainties. The mode frequency decreases with an increase in the NBI driven toroidal rotation, leading to the conclusion that the rotation of the mode is determined by the pressure gradient dominated term and toroidal rotation simultaneously.

The work of this thesis presents a systematic study of the ECEI diagnostic response when measuring in the pedestal and enabling the experimental characterization of the inter-ELM phase which serves as a valuable input for non-linear modeling that can assess transport associated with inter-ELM modes.



# Table of contents

<b>1</b>	<b>Fusion and tokamaks</b>	<b>1</b>
1.1	Thermonuclear fusion . . . . .	1
1.2	Magnetic confinement - tokamak . . . . .	3
1.3	High confinement regime . . . . .	7
1.4	Aim of this thesis . . . . .	8
<b>2</b>	<b>The ELM cycle</b>	<b>13</b>
2.1	Pedestal Stability . . . . .	14
2.2	Edge Localized modes (ELMs) and ELM cycles . . . . .	17
2.3	The peeling-ballooning model in connection to the ELM cycle . . . . .	19
2.4	Pedestal transport . . . . .	23
<b>3</b>	<b>ASDEX Upgrade experiment</b>	<b>27</b>
3.1	The tokamak . . . . .	27
3.2	Edge diagnostics . . . . .	28
3.2.1	Thomson scattering . . . . .	30
3.2.2	Lithium Beam Emission Spectroscopy (Li-BES) . . . . .	30
3.2.3	Edge charge exchange . . . . .	32
3.2.4	He beam emission spectroscopy . . . . .	32
3.2.5	Magnetic measurements . . . . .	33
3.2.6	Integrated data analysis (IDA) . . . . .	34
<b>4</b>	<b>Electron Cyclotron Emission</b>	<b>35</b>
4.1	Physical principles . . . . .	35



4.2	Wave propagation in magnetized plasmas . . . . .	38
4.3	ECE radiometry . . . . .	41
4.3.1	Basics of the heterodyne detection . . . . .	41
4.4	ECE based diagnostics at ASDEX Upgrade . . . . .	42
4.4.1	Profile ECE . . . . .	43
4.4.2	Correlation ECE (CECE) . . . . .	43
4.4.3	ECE Imaging (ECE imaging) . . . . .	44
4.5	Mode analysis limitations of ECE imaging & ECE . . . . .	48
4.5.1	Geometry effect: Doppler shift-broadening . . . . .	50
4.5.2	Shine-through emission . . . . .	51
4.5.3	Density variation . . . . .	52
4.6	Summary and discussion . . . . .	57
<b>5</b>	<b>Density effects on ECE imaging edge measurements</b>	<b>59</b>
5.1	Introduction . . . . .	60
5.2	ECE imaging at ASDEX Upgrade . . . . .	62
5.3	Forward modeling of the radiation detected by the ECE imaging . . . . .	64
5.4	Observations of the modes between ELM crashes . . . . .	69
5.5	Spatial localization . . . . .	73
5.6	Forward model of the EC radiation with density fluctuations . . . . .	75
5.7	Mode velocities and comparison to the $v_{E \times B}$ velocity . . . . .	76
5.8	Summary and Discussion . . . . .	78
<b>6</b>	<b>Characterization of low-frequency modes</b>	<b>81</b>
6.1	Introduction . . . . .	82
6.2	Overview of the discharge . . . . .	83
6.3	Magnetic properties of modes . . . . .	87
6.4	Localization . . . . .	89
6.5	Mode structure and poloidal velocity of the mode . . . . .	92
6.6	Interaction between inter-ELM modes . . . . .	95
6.7	Summary and Discussion . . . . .	98

---

<b>7</b>	<b>Parameter space of low-frequency modes</b>	<b>101</b>
7.1	Power spectrum of modes . . . . .	101
7.2	Mode frequency in comparison with plasma parameters . . . . .	103
7.2.1	Database overview . . . . .	103
7.2.2	Input power dependency . . . . .	104
7.2.3	Mode velocity . . . . .	108
7.2.4	Mode frequency in relation to the global $\beta_p$ . . . . .	110
7.3	Discussion . . . . .	111
<b>8</b>	<b>Conclusions and outlook</b>	<b>113</b>
8.1	Conclusions . . . . .	113
8.2	Outlook . . . . .	118
	<b>Bibliography</b>	<b>121</b>
	<b>Acknowledgments</b>	<b>135</b>
	<b>Curriculum Vitae</b>	<b>139</b>
	<b>List of publications</b>	<b>141</b>



# Chapter 1

## Fusion and tokamaks

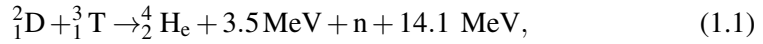
One of the primary drivers of the economic and social development is energy. This energy is used amongst others for transport, heating, and electricity. A doubling of the world's energy demand is foreseen until 2050 with an expected increase of the CO<sub>2</sub> emission, as the current leading energy resources are fossil fuels [International Energy Agency, 2017]. However, when compared to the last three decades, an increase renewable energy capacity and more efficient energy consumption became a trend, but with renewable energy sources being intermittent, a steady base-load cannot be fulfilled. Nuclear fusion is a promising candidate to provide this base-load electricity with abundant fuel resources.

In this chapter, the concept of thermonuclear fusion as a new energy source is introduced with a focus on magnetic confinement fusion. As the leading design in magnetic confinement research is a tokamak, the tokamak concept is explained in detail. In the last section of this chapter, the aim of the thesis is presented.

### 1.1 Thermonuclear fusion

Nuclear fusion is a process in which light nuclei fuse thus forming heavier nuclei and subatomic particles (neutrons or protons). The mass difference between the final products of the reaction and the reactants is converted into energy. Nuclear fusion is the mechanism that powers the stars [Eddington, 1920]. In the sun, for example, hydrogen atoms, are fused into helium in the proton-proton chain reaction,

and millions of tons of hydrogen are converted into helium every second. Nuclear fusion in terrestrial conditions relies on the nuclear reaction between isotopes of hydrogen; deuterium and tritium as it has the most efficient reaction-rate among other possible candidates. Thus, the reaction



is a leading candidate for the international fusion program. The products of this reaction are  ${}^4_2\text{He}$  carrying a kinetic energy of 3.5 MeV and a neutron  $n$ , carrying 14.1 MeV of kinetic energy. The fusion fuel deuterium ( ${}^2_1\text{D}$ ) has natural abundance in oceans of about one atom in 6420 of hydrogen [Wikipedia contributors, 2018] while tritium ( ${}^3_1\text{T}$ ) is a radioactive hydrogen isotope whose half-life is 12.32 years, hence naturally occurring tritium is extremely rare. Tritium can be produced by irradiating lithium (Li) with neutrons generated in a fusion reaction. The highest cross section for the reaction described by equation 1.1 is at a temperature of several tens of keV \*. When atoms are brought to those temperatures, the electrons are completely stripped from their nuclei, and the gas is in a plasma state. The Coulomb repulsive forces between like-charged nuclei are acting against nuclear attractive forces. Therefore, particles have to be brought to the required conditions to fuse. Those conditions mean temperature  $T$  high enough to overcome the repulsive Coulomb forces, moreover, a sufficiently large number of particles (density  $n$ ) has to be confined for a long enough time to allow for the plasma heating by alpha-particles to overcome the conductive and Bremsstrahlung energy losses from the hot plasma [Lawson, 1957]. This requirement is expressed as the Lawson-criterium:

$$n\tau_E T > 5 \times 10^{21} \text{m}^{-3} \text{s keV}, \quad (1.2)$$

where the energy confinement time  $\tau_E = W/P_{\text{loss}}$  is defined as the ratio of the plasma stored energy  $W$  and the power losses from the plasma  $P_{\text{loss}}$ .

In the case of massive stars, the plasma is confined via gravitational forces while the inertial and magnetic confinement tend to achieve fusion in controlled conditions on

---

\*1 eV  $\sim$  11 605 K

earth. The main focus of this work is Magnetic Confinement Fusion (MCF) where the charged particles are confined with magnetic fields in a toroidal vacuum chamber.

## 1.2 Magnetic confinement - tokamak

A tokamak is a machine where the plasma gas is induced in a toroidally shaped metallic vessel and confined with magnetic fields. It was invented in the mid-20th century in the Soviet Union and has been a leading magnetic confinement concept ever since. Currently, the world's best-known tokamak is ITER<sup>†</sup> [Martin et al., 2008], with its first experiment being less than a decade away. The stellarator is another advanced concept with so-far poorer performance properties, but the advantage of steady-state operation. This thesis focuses on tokamaks [Wesson and Campbell, 1997].

The tokamak configuration with its main constituents is shown in figure 1.1. The strongest component of the magnetic field is a toroidal field (its direction is indicated as a blue arrow) and is generated by a set of external D-shaped coils, distributed around the vessel as shown in figure 1.1 in blue. Toroidicity of the main field imposes a gradient of the field and induces its curvature hence the charged particles undergo curvature and  $\nabla\mathbf{B}$  drifts with drift velocity  $\mathbf{v}_d$  defined as:

$$\mathbf{v}_d = \left( \frac{mv_{\parallel}^2}{q} + \frac{mv_{\perp}^2}{2q} \right) \frac{\mathbf{B} \times \nabla\mathbf{B}}{B^3}, \quad (1.3)$$

where  $m$  is the mass of the charged particle,  $q$  is the charge and  $v_{\parallel}$ , and  $v_{\perp}$  are the velocities parallel and perpendicular to the magnetic field  $B$ , respectively. As the drifts are dependent on the charge state, this drift motion will act on ions and electrons in different directions and perpendicular to both, the gradient of the field and its curvature. Hence, electrons and ions undergo a vertical motion in opposite directions. This then leads to charge separation and generation of an electric field  $\mathbf{E}$ . Due to the electric field, an additional  $\mathbf{E} \times \mathbf{B}$  drift emerges with velocity:

$$\mathbf{v}_{\mathbf{E} \times \mathbf{B}} = \frac{\mathbf{E} \times \mathbf{B}}{B^2}. \quad (1.4)$$

---

<sup>†</sup>"The Way" in Latin

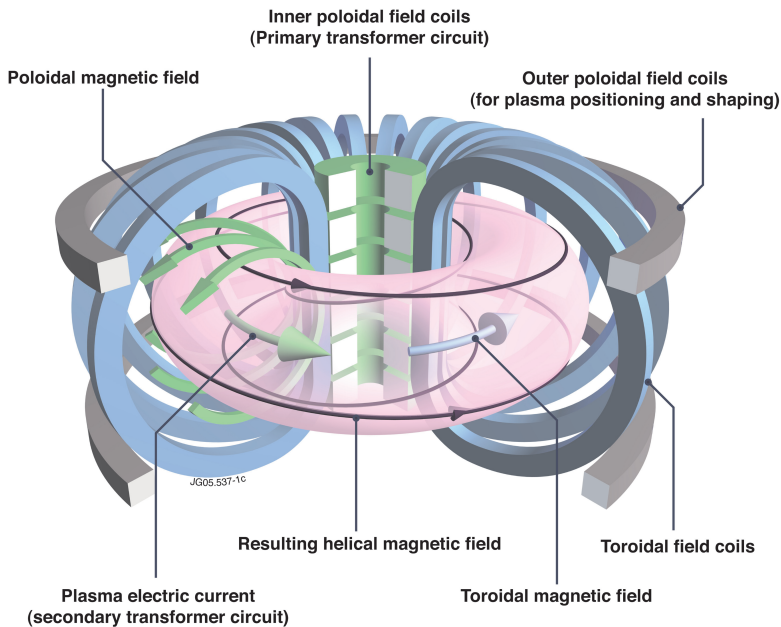


Figure 1.1: Tokamak principle: the plasma column is displayed as the magenta surface with the shape of the vacuum vessel. The toroidal field coils are shown in blue, and the poloidal field is created by the plasma current (in green). Vertical field coils are used for plasma shaping and positioning (shown in grey). Figure reference: [EUROfusion, 2011]

As this drift is independent of the charge, it leads to a very fast radial outward motion of all particles and thus prevents plasma confinement. In tokamaks, the poloidal field  $B_p$  is generated by a toroidal plasma current (as shown in green in figure 1.1) acting as a secondary winding of a transformer. This current is produced by a central solenoid (primary winding). The solenoid induces a loop voltage inside the vessel in a toroidal direction, hence inducing the toroidal current in the plasma. An additional set of coils (grey in figure 1.1) is used to produce a vertical magnetic field and for plasma control. The combination of toroidal and poloidal field generates helical field lines (as shown in black lines in figure 1.1) that wind around the torus and cancel the vertical drift by guiding particles from above to below the plasma equator and vice versa.

In a tokamak, plasma confinement is achieved by a balance of the plasma pressure that tends to expand the plasma and the magnetic field pressure trying to confine it. The confinement efficiency can be expressed as the ratio between the two:

$$\beta = \frac{\langle p \rangle_V}{\langle B^2 \rangle_V / 2\mu_0}, \quad (1.5)$$

where  $\langle p \rangle_V$  is the plasma pressure averaged over the total plasma volume  $V$ ,  $B$  is the total magnetic field and  $\mu_0$  is the vacuum permeability. A similar quantity, the poloidal beta  $\beta_p$ , approximates the feature of the plasma to enhance or diminish the externally applied magnetic field:

$$\beta_p = \frac{\langle p \rangle_s}{\langle B_p^2 \rangle_s / 2\mu_0}, \quad (1.6)$$

where  $s$  and  $B_p$  are averaged over the plasma surface area at the separatrix  $s$  which is the outermost closed flux surface (see figure 1.2).  $B_p$  is the poloidal field, i.e., the field from toroidal plasma current and poloidal field coils alone. An alternative definition of  $\beta_p$  uses the volume averaged pressure. In this context, an equilibrium is reached once the net forces acting upon the plasma are zero. This is expressed as a force-balance equation:

$$\mathbf{j} \times \mathbf{B} = \nabla p. \quad (1.7)$$

Thus, there is no pressure gradient along the magnetic field lines ( $\mathbf{B} \cdot \nabla p = 0$ ) and there is no radial current in equilibrium ( $\mathbf{j} \cdot \nabla p = 0$ ). The magnetic field lines are embedded into concentric magnetic surfaces of constant pressure and current. Nested magnetic flux surfaces with magnetic field lines covering them are shown in figure 1.2(a). As the magnetic surfaces are nested with constant properties along them, it is convenient to introduce a poloidal flux coordinate where all the quantities are flux functions. A normalised poloidal flux  $\rho_{\text{pol}}$  is defined as:

$$\rho_{\text{pol}} = \sqrt{\frac{\Psi - \Psi_0}{\Psi_S - \Psi_0}}, \quad (1.8)$$

where  $\Psi_0$  is the flux in the plasma centre and  $\Psi_S$  at the separatrix. The value of  $\rho_{\text{pol}}$  is 0 in the plasma centre whilst it is 1 at the separatrix, as depicted in figure



1.2(b). The separatrix is the outer most flux surface where the magnetic field lines are not in contact with the elements of the machine. The region outside the separatrix, scrape-off Layer (SOL), is the region of the opened field lines that guide the particles towards the divertor target plates. Usually, the divertor plates are installed at the bottom and the top of the machine, and they have to withstand high particle and heat loads.

Each magnetic field line twists around the torus making many poloidal ( $m$ ), and

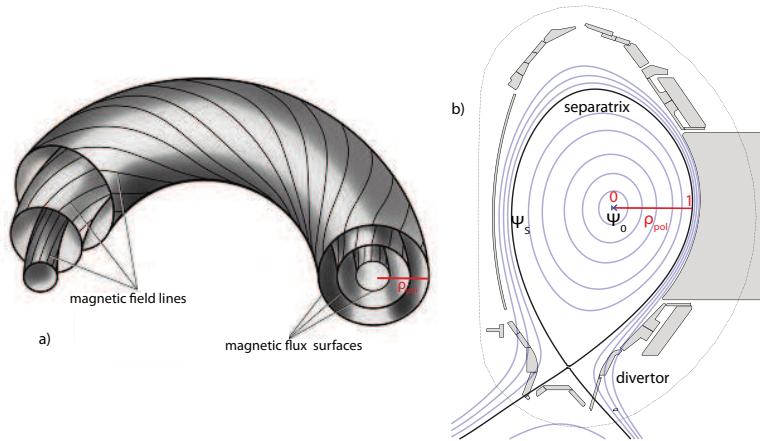


Figure 1.2: Toroidal geometry: a) nested flux surfaces with overlaid magnetic field lines. b) a poloidal cross-section of the tokamak flux surfaces.

toroidal ( $n$ ) turns simultaneously. After multiple turns, the field line might close in itself. It means that for one turn in toroidal direction  $\Delta\theta$  a field line moved for an angle  $\Delta\phi$  in poloidal direction. This is expressed as the safety factor  $q$  which is also a flux function:

$$q = \frac{\Delta\phi}{2\pi} = \frac{d\phi}{d\theta} = \frac{m}{n}. \quad (1.9)$$

The safety factor can also be expressed as the rate of change of toroidal flux with poloidal flux. If, after a finite number of helical turns, the field line closes in itself,  $q$  will be rational. For irrational  $q$  values, the field lines wind around the flux surface for an infinite number of turns thus covering the whole flux surface. Rational flux surfaces are more unstable as non-axisymmetric deformations of flux surfaces can be produced without bending field lines, and helical magnetic flux modulations

(magnetic islands) are possible. Typically the  $q$  profile ranges from 1 near the plasma centre to 7-8 at the plasma edge. As  $q$  is inversely proportional to the plasma current  $I_p$ , a larger  $q$  means a smaller current, hence, the plasma is more stable to current-driven instabilities. The stability of the plasma is often expressed in terms of the safety factor evaluated at 95% of the plasma flux,  $q_{95}$ .

### 1.3 High confinement regime

The high confinement mode (H-mode) is the most promising regime for the future fusion reactor ITER because its energy confinement time is a factor of two higher than that of its counterpart the L-mode (low confinement mode). The H-mode has been discovered in the ASDEX Upgrade predecessor ASDEX [Wagner et al., 1982]. It is a natural improvement in the confinement and happens when a certain power threshold is reached [Ryter et al., 2009]. The reason for the transition from a low to a high

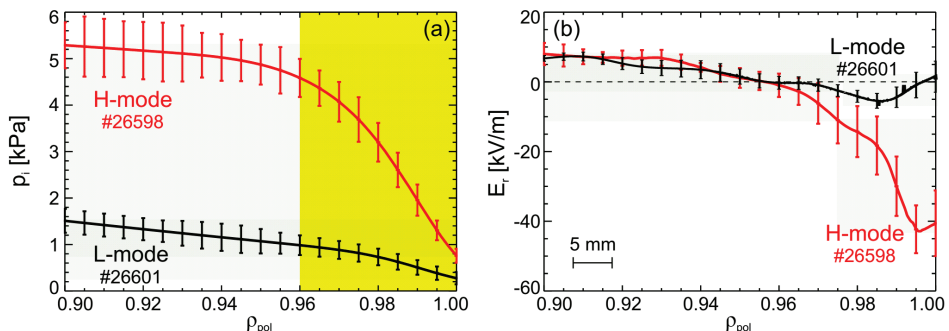


Figure 1.3: Pressure profiles in L and H mode with their characteristic radial electric field profiles. The pedestal region corresponds to the shaded area. Figure taken from [Viezza, 2013].

confinement regime is not yet fully understood, but a popular explanation is based on suppression of the turbulence induced-transport by a radially sheared  $E \times B$  flow [Biglari et al., 1990]. This flow is a consequence of the steepening of the  $E_r$  profile well that is formed during the H-mode (see figure 1.3(b)). As the cross-field transport is suppressed, the pressure profiles increase in a very narrow region, hence forming an Edge Transport Barrier (ETB) indicated by the shaded area in figure 1.3(a). The

gradients are steepening within the ETB forming a pedestal [Wagner et al., 1985]. As the pedestal values are now elevated, they largely influence the core profiles and hence, the fusion gain. Neoclassical theory argues that the edge  $E_r$  is essentially induced by the main ion species [Viezzler et al., 2014] which means that it is mainly determined by the gradient of the main ion pressure,  $E_r \approx \nabla p_i / (e \cdot n_i)$ , where  $\nabla p_i$  is the ion pressure,  $n_i$  is the ion density and  $e$  the elementary charge .

A unique feature of the high confinement regime is the occurrence of repetitive instabilities at the plasma edge, called Edge Localized Modes (ELMs). The ELMs are periodic relaxations, in the form of a crash of the edge transport barrier allowing heat and particles to escape radially from the confined plasma and in the scrape-off layer along the magnetic field into the divertor. ELMs are of major concern for future fusion reactors [Loarte et al., 2007] as they degrade the pedestal values necessary to maintain the core conditions for fusion, and they can be as well detrimental for the machine, as their power deposition might damage the divertor. A variety of ELM types has been identified by now, with type-I or large ELMs being the most detrimental for plasma facing components. A common way to differentiate between different ELM types is to track the behaviour of the ELM repetition frequency ( $f_{\text{ELM}}$ ) concerning the power across the separatrix  $P_{\text{sep}}$  [Zohm, 2014].  $P_{\text{sep}}$  is defined as  $P_{\text{sep}} = P_{\text{tot}} - P_{\text{rad}} - dW/dt$ , where the  $P_{\text{rad}}$  is the power radiated from the confined plasma and  $W$  is the plasma kinetic energy. Normally this criterion is used for type-I and type-III ELMs. The frequency of type-I ELMs increases as the  $P_{\text{sep}}$  increases, while for the type-III ELMs,  $f_{\text{ELM}}$  decreases. Type-II ELMs  $f_{\text{ELM}}$  show no clear dependence on  $P_{\text{sep}}$ , and are appearing in highly shaped plasmas.

The focus of this work is on type-I ELMs and coherent modes associated with them. Before an ELM crash, there is a spectrum of instabilities in the form of inter-ELM fluctuations and precursors that contains information on the boundary conditions for the ELM crash. The ELM crash itself is a part of a more global dynamics called ELM cycle that is reviewed in the following chapter.

## 1.4 Aim of this thesis

The complexity of the ELM cycle lies in its non-linearity, appearance of different instabilities, and complex transport properties. All of these are fast events spanning

time scales from microseconds to milliseconds. Furthermore, much of the physics related to the ELM cycle occurs within the last  $\sim 2$  cm of plasma, the pedestal. Therefore, in order to contribute to the understanding of processes determining the shape of the pedestal, its transport, and its stability, the experimental diagnostic tools must be compelling regarding temporal and spatial resolution. Their interpretation is especially demanding as steep gradients, and non-linear dependences must be taken into account.

In this work, the established diagnostic of electron cyclotron emission imaging (ECEI) is exploited to contribute to the understanding of transport and stability in the edge transport barrier of tokamak H-modes. An edge instability, which is dominantly visible in the ECEI diagnostic, is characterised with unprecedented accuracy. As the transport caused by such instabilities can only be described by non-linear modelling with appropriate codes, the results of this thesis form an essential input to codes that model the pedestal instabilities and quantify transport related to them.

The work presented in this thesis is conducted at the ASDEX Upgrade tokamak. With well established H-mode discharges and well-diagnosed plasmas, this machine is ideally suited for plasma edge studies. The main diagnostic tool used in this work is the ECE imaging diagnostic whose final upgrade and commissioning was performed during this thesis work.

The main research questions that this thesis aims to answer are grouped within the two topics:

*The first part* of the thesis aims to establish and quantify the effects that influence the measurements in the pedestal region. As the diagnostic upgrade introduces an additional toroidal viewing angle, the component of the electron motion parallel to the magnetic field modifies the signal. As part of this work following research questions emerged:

- Are measurements in the Scrape-Off Layer feasible with the ECEI system and is it possible to associate relevant temperature fluctuations to the filamentary structures expelled during an ELM crash?
- Are the main kinetic broadening mechanisms like relativistic and Doppler shift-broadening enhanced due to the upgrade, and how do they reflect in the

radial resolution of the system? Are measurement positions affected by this change in the geometry of the system?

- How much of the fluctuation signal measured with the ECEI system, which is considered a temperature diagnostic, is affected by the variation of the density at the plasma edge?

*The second part* of the thesis is devoted to the exploration of the coherent fluctuation identified in the lower part of the frequency spectrum in H-mode plasmas during the inter-ELM period. The research questions related to the mode and to be answered are:

- What is the experimental signature of the low-frequency mode?
- What are characteristics of the mode regarding its position, velocity, spatial structure?
- What is the nature of the mode, is it resistive or ideal?
- How does the mode behave when changing plasma parameters such as pressure gradient, plasma heating? Is it possible to identify the upper and the lower threshold in plasma parameters where modes are not visible for the diagnostic?

To answer the above questions, the thesis is structured as follows: In the following chapter, chapter 2, the theoretical basis is introduced in which an overview of the ELM cycle is given from the present understanding point of view. Chapter 3 introduces the ASDEX Upgrade tokamak and its edge diagnostics that are utilised in this work. Chapter 4 is focused on the Electron Cyclotron Emission-based diagnostics. In this chapter, a brief overview of the profile ECE and Correlation ECE diagnostic is given with the focus on the ECE Imaging diagnostic. Furthermore, the sensitivity of the system is studied in detail using the electron cyclotron radiation transport forward model. Chapter 5 assesses the capabilities of the ECEI measurements in the SOL region by exploiting the synthetic diagnostic generated with the electron cyclotron forward model and using profiles generated with the MHD code JOEKE. Moreover, the

---

identified inter-ELM mode is introduced as a dominant mode in the ECEI signal. The detailed characterisation of the mode regarding its structure, position and velocities are presented in chapter 6. The connection of the mode characteristics with plasma parameters is described in chapter 7. The outlook of the thesis and proposals for future work are given in the last chapter.



## Chapter 2

# The ELM cycle

Since the discovery of the high confinement regime of plasma operation (H-mode) [Wagner et al., 1985], this has been a leading path in the design of the baseline scenarios [ITER Physics Basis Editors et al., 1999] for the operation of future fusion machines. The H-mode occurs naturally when a certain heating power threshold is reached [Keilhacker, 1987]. A sudden improvement in plasma confinement is then observed. The defining feature of the H-mode is a transport barrier forming near the edge, just within the last closed flux surface. This edge transport barrier (ETB) generally arise if the derivative of the radial electric field exceeds some critical value. The associated shear in the  $E \times B$  flow then exceeds the coherence time of the turbulence, leading to decorrelation of the turbulent eddies and suppression of the anomalous transport. This ETB can be viewed as a barricade preventing the outflow of heat and particles. The formation of the ETB leads to steepening of the pressure gradient, and the result is a systematic increase of the entire profile equal to the height of the profile across the ETB, in the form of the pedestal. The height and width of the pedestal play a crucial role in the core confinement as the pedestal height (which is a measure of the pressure at the top of the pedestal) is directly proportional to the core pressure. However, an ETB can reach a critical values such that instabilities, driven by this large pressure gradient and the associated large current density, the so-called bootstrap current, can rise. Depending on the pressure gradient and the current density, several types of instabilities may occur that cause a transient loss of particles and heat around the ETB. These edge localised modes (ELMs) thus cause repetitive bursts of



particles and heat out of the confined plasma, towards the divertor plates. Those bursts facilitate the impurity transport [Pütterich et al., 2011] thus preventing the radiative collapse of plasma. However, due to the detrimental effects that ELMs can have on the future fusion reactor (melting of the divertor components), avoidance, mitigation, and suppression of ELMs are one of the key research topics. The avoidance of ELMs is achieved by exploring new operational regimes without naturally occurring ELMs, such as the Quiescent H-mode [Burrell et al., 2016, Hu et al., 2015], and I-mode [Walk et al., 2014]. ELM mitigation is another possibility for tokamak operation and has been achieved with the application of external magnetic perturbation fields [Suttrop et al., 2011]. Another mitigating technique is ELM pacing via injecting pellets of frozen deuterium [Baylor et al., 2013]. In this way, the ELM crash is induced to happen at a higher rate than the natural ELM frequency. The ELMs with higher repetition frequency are known to deposit less power to the divertor. The full ELM suppression involves the application of an external magnetic perturbation and is a promising candidate. However, those scenarios are still in the experimental phase and are not easily reproducible. Although the research on ELM avoidance is ongoing, the ELM cycle is not yet well understood. In this chapter, the ELM cycle will be reviewed from the perspective of the present knowledge on the physics of the pedestal.

## 2.1 Pedestal Stability

A broad range of instabilities generated in the pedestal are classified as magneto-hydrodynamic (MHD) instabilities. The main features of the pedestal are strong gradients, and they are the main source of destabilizing forces. To understand the stability of the pedestal, the interconnection of stabilizing and destabilizing forces has to be addressed. This is the main task of linear stability theory that assesses the parameter space of stable and unstable regions. The non-linear stability is in charge of addressing the amplitudes of the MHD modes, non-linear coupling between modes, transport coefficients associated with them and the effects they have on plasma performance.

The starting point is a self consistent description of a macroscopic equilibrium that can be expressed within a fluid MHD picture [Freidberg, 1987, Zohm, 2014]. By

restricting attention to long-wavelength, low-frequency phenomena, the two-fluid model can be reduced to a single-fluid model known as MHD. In this picture, plasma is a conducting fluid exposed to the external magnetic fields acting upon the fluid. The motion of the plasma can then be described with a self consistent set of hydrodynamic equations supplemented with the Maxwell's equations. The single-fluid MHD variables are the mass density  $\rho$ , macroscopic velocity  $\mathbf{v}$ , current density  $\mathbf{j}$  and pressure  $p$  and the respective equations are:

Continuity equation :

$$\frac{\partial \rho}{\partial t} + \nabla \cdot (\rho \mathbf{v}) = 0. \quad (2.1)$$

Momentum or force-balance equation :

$$\rho \frac{d\mathbf{v}}{dt} = \mathbf{j} \times \mathbf{B} - \nabla p. \quad (2.2)$$

Ohm's law :

$$\mathbf{E} + \mathbf{v} \times \mathbf{B} = \eta_{\parallel} \mathbf{j}. \quad (2.3)$$

Adiabatic closure :

$$\frac{d}{dt} \left( \frac{p}{\rho^{\gamma}} \right) = 0. \quad (2.4)$$

Maxwell's equations:

$$\nabla \times \mathbf{E} = -\frac{\partial \mathbf{B}}{\partial t}, \quad (2.5a)$$

$$\nabla \times \mathbf{B} = \mu_0 \mathbf{j}, \quad (2.5b)$$

$$\nabla \cdot \mathbf{B} = 0. \quad (2.5c)$$

In a tokamak plasma the toroidal magnetic field is stronger than the poloidal components and is approximately time independent. The ideal MHD assumes zero

resistivity, and in this case eq. (2.3) becomes:

$$\mathbf{E} + \mathbf{v} \times \mathbf{B} = 0. \quad (2.6)$$

In ideal MHD the magnetic topology is not changing.

By solving the above equations, it is possible to determine the plasma equilibrium where the forces acting upon the plasma are balanced. Any perturbation of the plasma from its equilibrium will cause the system to oscillate. The equilibrium is stable or unstable according to whether small perturbations are damped or amplified. The force balance equation (eq. (2.2)) in an equilibrium state ( $d/dt \rightarrow 0$ ) describes the interplay between the pressure gradient forces  $\nabla p$  and forces due to the current density  $\mathbf{j}$  and magnetic field  $\mathbf{B}$  therefore, the pedestal equilibrium is determined by the topology of the magnetic field, achievable pressure gradient and currents in the pedestal.

The energy principle [I. B. Bernstein, 1958] is employed in the analysis of the stability of such a system. The approach is to apply a linear stability analysis of a system where the above equations are linearised after introducing a small displacement  $\xi$  around its equilibrium value. If the perturbation lowers the potential energy of the system, then the system is unstable. The change in the energy of the system  $\delta W$  resulting from a displacement  $\xi$  of the plasma is given by the volume integral over the plasma [Wesson and Campbell, 1997, Zohm, 2014]:

$$\delta W_F = \frac{1}{2} \int_{\text{Plasma}} \left( \frac{|B_{1\perp}|^2}{\mu_0} + \frac{B_0^2}{\mu_0} |\nabla \cdot \xi_{\perp} + 2\xi_{\perp} \cdot \kappa| + \gamma p_0 |\nabla \cdot \xi|^2 \right. \\ \left. - \underbrace{2(\xi_{\perp} \cdot \nabla p_0)(\kappa \cdot \xi_{\perp}^*)}_{\text{pressure}} - \underbrace{\frac{j_{0\parallel}}{B_0} (\xi_{\perp}^* \times \mathbf{B}_0) \cdot \mathbf{B}_1}_{\text{current}} \right) dV, \quad (2.7)$$

where 0 and 1 denotes the equilibrium and the perturbed values respectively,  $\kappa$  is the curvature vector of the equilibrium magnetic field and  $\xi$  the displacement. Parallel and perpendicular refer to the direction to the magnetic field. Here only the fluid (plasma) part of the energy change is given as the vacuum part is usually stabilising. The displacement can be non-zero, but the contribution to the energy change from

the surface integral goes to zero if there are no surface currents.

The first terms in eq. (2.7) describe the stabilising effects of the field line bending and corresponds to stable waves. The terms in the second line of eq. (2.7) are pressure, and current instabilities and those are destabilising. As the plasma is assumed to be perfectly conducting, this class of instabilities is assessed via ideal MHD theory. In this context, if an ideal MHD analysis results in instability, it does not exclude the appearance of its resistive analogue.

*Pressure driven instabilities* depend on the orientation between the pressure gradient and the torus curvature. The pressure gradient is oriented towards the centre of the plasma while the curvature of the field line is pointing towards the centre of the torus. The region where those two vectors are pointing in the same direction is a 'bad curvature' region, while a 'good curvature' region corresponds to a region where the two vectors are opposing each other. The bad curvature region is the low-field side of a tokamak, and the good curvature region is at high-field side. In the bad curvature region, the instabilities grow similar to a balloon. Hence the name 'ballooning mode'. *Current driven instabilities* are driven, as seen from the second destabilizing term in eq. (2.7), by the current density  $j_{\parallel}$  parallel to the field  $B_0$ . Such an instability leads to an external kink of the magnetic surfaces. The driving force of this instability is the edge current that consists of different sources: a negligible fraction of Ohmic current, Pfirsch-Schlüter currents and bootstrap currents [Coronado and Wobig, 1992, Bickerton et al., 1971]. The bootstrap current is the dominant contribution to the edge current density and couples the total edge current density to the pressure gradient. A magnetic shear stabilises the kink at the edge. As the plasma surface looks like 'peeled off' due to this external kink, peeling modes is the term regularly used.

## 2.2 Edge Localized modes (ELMs) and ELM cycles

Edge Localized Modes are a class of MHD instabilities affecting the last few centimetres of the confined region. As can be seen in figure 2.1, where a vertical dashed line marks the beginning of each ELM crash, the depicted quantities are displaying a sudden change at the crash. While an ELM refers to a crash only, an ELM cycle comprises the crash itself and all the phases in between two subsequent ELMs.

In figure 2.1, a signature of the global and plasma edge parameters during a typical type-I ELM cycle at ASDEX Upgrade is shown. The divertor shunt current ( $I_{\text{DIV}}$ ) is

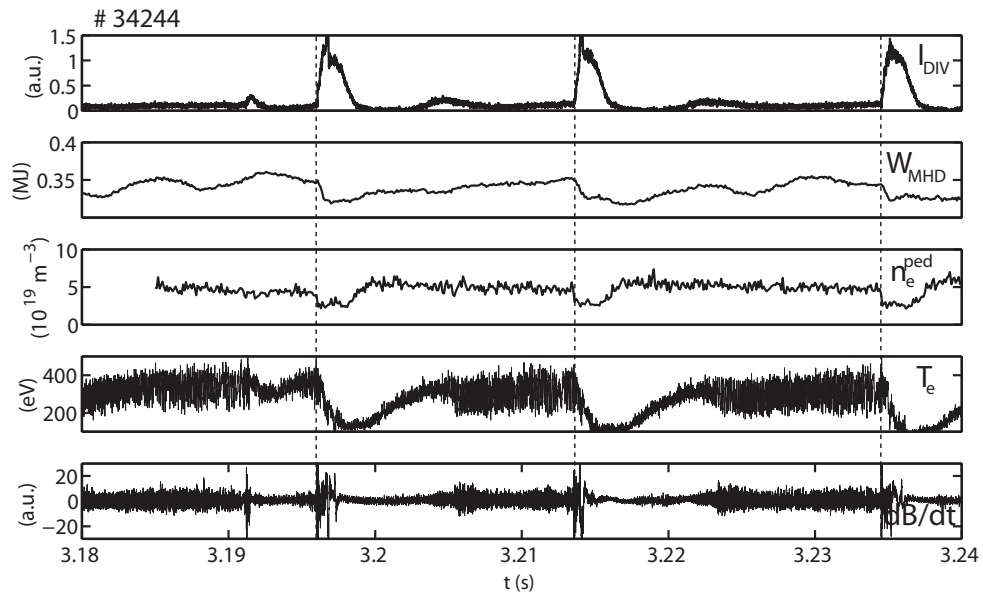


Figure 2.1: ELM cycles during ASDEX Upgrade shot #34244: Divertor shunt current ( $I_{\text{DIV}}$ ), plasma stored energy ( $W_{\text{MHD}}$ ), density at the pedestal top ( $n_e^{\text{ped}}$ ), the electron temperature in the steep gradient region ( $T_e$ ) and the magnetic signal ( $\text{dB}/\text{dt}$ ).

increased due to heat deposited in the divertor, the plasma stored energy ( $W_{\text{MHD}}$ ), pedestal top electron density ( $n_e^{\text{ped}}$ ), the electron temperature ( $T_e$ ) in the steep gradient region are dropping. This event is also seen in the magnetic measurements as the perturbation of the magnetic equilibrium ( $\text{dB}/\text{dt}$ ). After the crash, the recovery phase of each quantity is different. The depicted ELMs belong to a class of ELMs known as type-I or large ELMs. This type of ELMs is by far the most detrimental for the plasma facing components among all the other ELM types as it can expel 5 to 30 % of the total plasma thermal energy. For more details and the classification of ELM types, the reader is further directed to [Zohm, 1996, J W Connor, 1998, Leonard, 2014].

The linear stability boundary, i.e., the onset of the ELM crash, is often described by the coupling of peeling and ballooning modes in the pedestal. The peeling modes are driven by the local edge current density and the ballooning modes by the steep pres-

sure gradient. When the pedestal parameters reach the peeling-ballooning limit, an ELM crash occurs [Gohil et al., 1988]. However, before an ELM crash, there exists a broad spectrum of instabilities in the pedestal region, so-called inter-ELM modes [Diallo et al., 2015, Laggner et al., 2016]. These inter-ELM modes might cause transport and influence the pedestal structure. The pedestal structure determines the stability of coupled peeling-ballooning modes and therefore the achievable pedestal top pressure [Snyder et al., 2002, Wolfrum et al., 2015]. The inter-ELM modes and precursors are focus of ELM-directed research for decades. Both have been observed in different machines. MHD modes such as palm tree modes [Kosowski et al., 2005] and washboard modes [Perez et al., 2004b] have been detected at JET. ELM precursors have been observed at ASDEX Upgrade [Suttrop et al., 1996], COMPASS-D [Colton et al., 1996] and JET [Perez et al., 2004a]. At ASDEX Upgrade, simultaneous observations of high-frequency and low-frequency inter-ELM modes, related to type-I ELMs, have been reported [Bolzonella et al., 2004]. High (200-300 kHz) and mid-frequency (50-100 kHz) inter-ELM modes at ASDEX Upgrade have been characterized, and have been inferred from measurements of the toroidal and poloidal mode numbers to be resonant at  $q$ -surfaces near the minimum radial electric field  $E_r$  and at the separatrix, respectively [Laggner et al., 2016, Mink et al., 2016]. Quasi-coherent modes during an ELM cycle are observed in DIII-D [Diallo et al., 2015]. The inter-ELM pedestal evolution has the same sequence of recovery for different ion species [Laggner et al., 2017].

The inter-ELM modes and precursors are the critical ingredient of an ELM cycle, as they cause transport in the pedestal and influence the crash itself. Inter-ELM modes identified in the lower band of the frequency spectrum are the main focus of this work.

## **2.3 The peeling-ballooning model in connection to the ELM cycle**

The peeling-ballooning (P-B) model, derived from MHD is currently the leading model explaining the evolution of the pedestal leading to an ELM crash. It is based on the coupling between the pressure and current driven instabilities

[Snyder et al., 2002, J W Connor, 1998]. As the pedestal can be approximated by its width and height, the peeling-ballooning model is based on theoretical analysis of MHD modes that can limit the pedestal height and drive ELMs.

The illustration of the pedestal build-up derived from the EPED model and

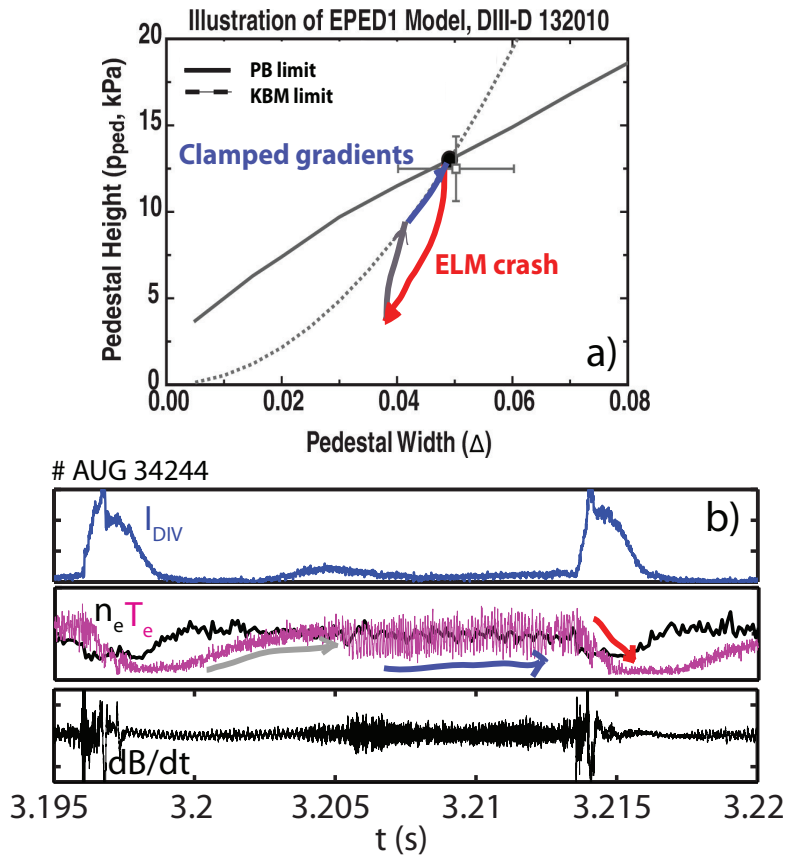


Figure 2.2: a) Following the initial recovery, the pedestal further evolves along the KBM limit until it hits the P-B boundary inducing an ELM crash. Figure modified from [Snyder et al., 2009]. b) Temporal evolution of the divertor current ( $I_{DIV}$ ), electron density ( $n_e$ ) and temperature ( $T_e$ ) in the pedestal and temporal magnetic oscillations  $dB/dt$  during an ELM cycle at ASDEX Upgrade.

correlation with the temporal evolution of  $n_e$  and  $T_e$  for a typical ASDEX Upgrade discharge featuring type-I ELMs is shown in figure 2.2. The EPED model

[Snyder et al., 2009, Snyder et al., 2011], a predictive model for the pedestal height and width, combines a width model with P-B stability calculations.

The recovery of plasma edge parameters follows the ELM crash. Soon after the crash, the pedestal density and temperature profiles start to build up, albeit on different time scales [Burckhart et al., 2010]. Such time evolution of the density and the temperature on different time scales, during an ELM cycle, impose constraints on two-fluid dynamics in MHD codes. The electron density recovers at a faster rate while the temperature increases gradually until the next ELM crash. After the ELM crash, the pedestal pressure rapidly builds up its height. According to the EPED model, a 'soft' limit is reached at the kinetic-ballooning mode (KBM) constraint. This setting of microturbulence in the pedestal allows for additional transport that keeps the gradients fixed. This corresponds to the evolution of the pedestal along the KBM limit as shown in figure 2.2(a), and to the established values of the  $n_e$  and  $T_e$  in the pedestal, shown in figure 2.2(b). Furthermore, pedestal width and height increase further until the P-B (hard) limit, is reached. This hard limit represents the ELM onset. The pressure gradient alone cannot be responsible for an ELM crash, as it has been observed that the pedestal can evolve along the KBM limit. This is because the current has a stabilising effect on ballooning modes. Therefore the pedestal width can increase further until it hits the P-B stability boundary. The stability space can be manipulated by plasma shaping, i.e., changing the shape of the plasma cross-section. As shown in figure 2.3, different cross sections are obtained by varying upper and lower triangularity of the plasma. The upper ( $\delta_u$ ) and lower ( $\delta_l$ ) triangularity are determined as the ratio of the radial distance between the highest and the lowest point of the plasma and the mid-radius of the plasma. The average value can, therefore, be defined as  $\langle \delta \rangle = (\delta_u + \delta_l)/2$ . It is a measure of the D-shape of the plasma. As shown the red curve is closest to the D-shape therefore, has the strongest shaping.

Figure 2.4 illustrates accessible stable regions due to change in the plasma shaping towards higher normalised pressure gradients ( $\alpha$ ) and current densities ( $j$ ). The normalized pressure gradient  $\alpha$  is defined as  $\alpha \sim -(2\mu_0 R_0 q^2 / B^2) \nabla p$ . Higher  $\delta$  stabilises the plasma edge by pushing the magnetic field lines towards the high field side region. The pedestal stability also improves with an increase in Shafranov shift. Shafranov shift is the displacement of the centre of flux surfaces with minor radius due to plasma pressure. As the  $\beta_p$  increases, the Shafranov shift increases thus



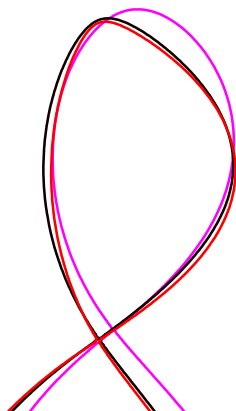


Figure 2.3: Three different plasma cross-sections obtained by varying the upper and the lower plasma triangularity. Low shaping corresponds to the magenta line, black to a moderate one, and the highest shaping is depicted in red.

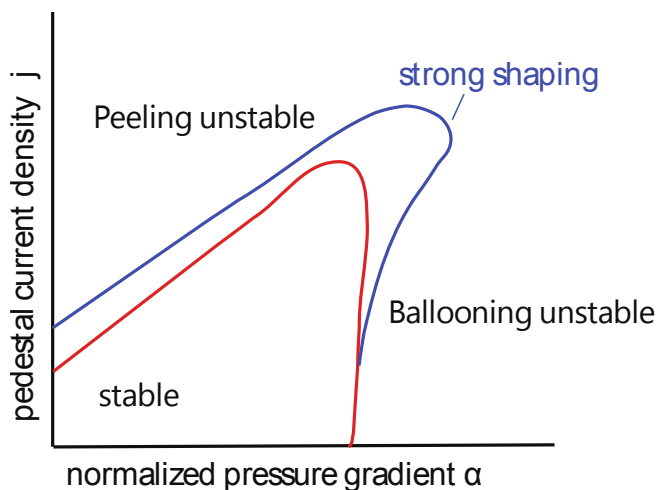


Figure 2.4: Stability boundary of plasma equilibrium for normalised plasma pressure gradient  $\alpha$  and current density in red. Illustration of plasma shaping effect in purple. Figure modified from [Snyder et al., 2009].

having a stabilising effect on P-B modes allowing for higher pedestal top pressures

[Maggi et al., 2007, Maggi, 2010]. Figure 2.5 shown the stability limit contours for different  $\beta_p$  values for high triangularity JET plasmas [Urano, 2014].

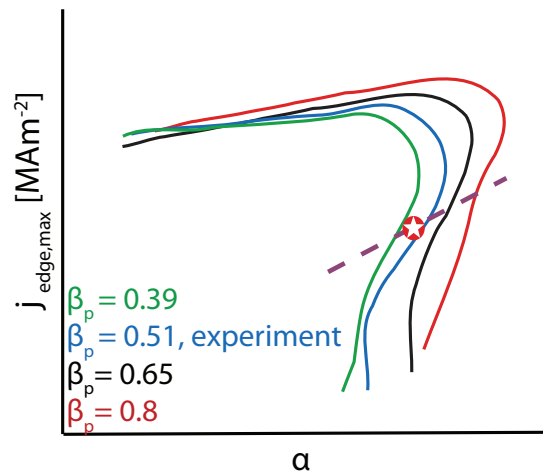


Figure 2.5: Illustration of the stability limit contours for different  $\beta_p$ . The stable regions are to the lower left of the curves. Figure modified from [Urano, 2014]

## 2.4 Pedestal transport

Although the P-B theory explains the phenomenology of the ELM cycle, the recovery period (evolution along the KBM limit) is not yet understood. Multiple precursors are observed, but no clear link between the linear phase (inter-ELM) and the ELM crash itself has been established. Predictions of the development of an ELM cycle is not possible from the linear analysis. Non-linear coupling of the peeling and ballooning modes is necessary, hence a non-linear theory has to be involved. Both, MHD modes and turbulence contribute to particle and heat transport in the pedestal.

The respective magnitudes are still an open question and can only be addressed by non-linear calculations.

## MHD

As seen from the P-B model, large-scale instability, like coupled peeling-ballooning modes, regulate the plasma and energy exhaust across the separatrix in inter-ELM regimes. The P-B model captures the essentials of the ELM dynamics but is missing a few key elements such as shear at the edge, resistivity, two-fluid MHD, fast particle effects. In recent years a non-linear MHD JOREK code [Huysmans and Czarny, 2007] has been developed to investigate large-scale MHD instabilities. It is based on robust fully implicit numerics, including neo-classical and diamagnetic effects, and includes divertor boundary conditions and resistive wall effects [Höelzl et al., 2012]. It also can be extended to include two-fluid effects and neoclassical flows. The key edge physics application with JOREK can be found in [Höelzl et al., 2018] and the validation with the experiment regarding the ELM crash in [Mink et al., 2018].

## Turbulence

Over the past few decades, gyrokinetic simulations have been brought to ever more realistic geometry and physics conditions, and different instabilities have been identified to play an essential role in the pedestal. In the gyrokinetic approximation the temporal scales of collective electrostatic and electromagnetic fluctuations are much longer ( $\sim$  kHz) than a period of a charged particle's cyclotron motion ( $\sim$  GHz); hence the cyclotron motion is neglected. However, the spatial scales of such fluctuations are much smaller than the scale lengths of the background magnetic-field inhomogeneity, and the amplitudes are much smaller than the thermal background noise. Properties of two types of modes that drive the turbulence in the pedestal are listed in table 2.1. A general theoretical survey on turbulence can be found in [Conner and Wilson, 1994] and below, only the two are briefly introduced.

*Kinetic ballooning modes (KBMs)* are the main candidates for driving the transport in the pedestal region. KBMs are driven by the pressure gradient, and they propagate in the ion diamagnetic direction [Tang et al., 1980, Frieman et al., 1980]. At JET, from local gyrokinetic simulations, the KBMs are found to be unstable only in the

Instability	Drive	Propagation	Parity
KBM	$\nabla p$	ion diamagnetic direction	Ballooning
MTM	$\nabla T_e, \nabla n_e$	electron diamagnetic direction	Tearing

Table 2.1: Candidate modes for driving tokamak turbulence in the pedestal [Manz et al., 2014]. Kinetic Ballooning Mode (KBM), Micro Tearing Mode (MTM). Propagation direction is in the ion diamagnetic direction or the electron diamagnetic direction. The parity denotes whether the fluctuation is ballooning or tearing.

extreme edge of the plasma and not in the whole pedestal [Saarelma et al., 2013]. From global gyrokinetic simulations, it is concluded that KBM modes are the dominant microinstabilities in the steep pedestal region at MAST and they can regulate the pressure gradient [Saarelma et al., 2017]. A good correlation is found between the region where KBMs dominate and the region that is unstable to infinite- $n$  ideal ballooning modes [Dickinson et al., 2011].

*Microtearing modes (MTM)* are mainly driven by the electron temperature gradient although it has been reported that there exists a preferred value of the density gradient for MTMs to grow [Told et al., 2008]. MTMs usually cause small-scale magnetic islands and therefore, enhanced radial electron heat transport. Their poloidal propagation is in the electron-diamagnetic direction. Analysis with gyrokinetic models shows that the MTMs exist at the pedestal top of MAST plasmas [Dickinson et al., 2013]. For ASDEX Upgrade MTMs have been verified to exist further inside the pedestal top [Told et al., 2008]. Both MTMs and KBMs are found to be unstable in the pedestal top of MAST plasmas. This suggests that the MTM at the pedestal top allows its widening, hence the steepening of the gradients that drive the KBM unstable [Dickinson et al., 2012].

As the amplitude caused by the turbulence is very low, experimental measurements in the pedestal region are extremely challenging. They require high-precision, high-sensitivity diagnostics. As a consequence, validation of gyrokinetic codes is lacking. To unfold such small amplitudes, correlation techniques are often used [Freethy et al., 2016, van Milligen et al., 1995]. Another disadvantage is that a slight variation in radial position can lead to a significant change in the gradients. Hence they result in hybrid turbulent structures that are difficult to detect. The onset of

an ELM crash can be described with sufficient reliability by linear P-B theory. In the inter-ELM period density and temperature recover on different time scales, and various phases can be identified, which are also characterised by distinct signatures in the magnetics. Both MHD modes and turbulence driven modes can influence transport in the pedestal. Quantification of the transport induced by the various instabilities is only possible with non-linear modelling. While electron heat transport in the pedestal is likely to be dominated by ETG modes, particle and heat transport could be caused by MTMs and KBMs as well as by MHD modes. To distinguish between the contributions and to validate the non-linear calculations, the experimental characterisation of modes in the pedestal is an essential contribution to the understanding of pedestal transport.

## Chapter 3

# ASDEX Upgrade experiment

The ASDEX Upgrade tokamak (Axial Symmetric Divertor EXperiment) has been operated by the Max-Planck Institute for Plasma Physics in Garching, near Munich in Germany since 1991. This tokamak is currently the second largest fusion machine in Germany, the first one being the stellarator Wendelstein 7-X. The ASDEX Upgrade tokamak has been made available to the European fusion research community since 2002, and since 2014 it is part of the EUROfusion mid-size tokamak (MST) programme, together with TCV (Swiss Plasma Center (SPC)) [S. Coda, 2017] and MAST-upgrade (Culham Centre for Fusion Energy (CCFE)) [H. Meyer, 2013]. The MST Programme complements the research programme of the current world's largest tokamak JET [F. Romanelli, 2015] (CCFE). A significant role for ASDEX Upgrade is to prepare physics input for design and operation of ITER [Martin et al., 2008] and DEMO [Zohm et al., 2017].

### 3.1 The tokamak

With a major radius of  $R = 1.65$  m and minor radius of  $a = 0.5$  m ASDEX Upgrade is a medium size machine. It is about half the size of the JET tokamak and one-quarter of the size of ITER. It has full tungsten walls and a heating system with a total input power of over 25 MW. The high ratio of heating power  $P_H$  to the machine size given by the major radius  $R$  is unique and closer to ITER than any other device worldwide. The poloidal field at ASDEX Upgrade is generated with a set of external

coils: the ohmic heating (OH) transformer coils, and the vertical field coils designed to produce different magnetic configurations (double null (DN) or single null (SN) configurations). Most of the ASDEX Upgrade plasma discharges are in the SN configuration. Vertical field coils regulate the shaping and position of the plasma. Additionally, a set of external coils is used to control the stability of elongated plasmas. The OH system consists of the central OH transformer coil and two coil pairs. The five OH coils in total, predominantly the central OH1, induce the toroidal plasma current  $I_p$  that confines the plasma. The achievable total magnetic field on axis is up to 3 T with the highest current of 1.2 MA. Typical plasma discharges are performed with  $B_t = 2.5$  T and  $I_p = 0.8$  MA to 1 MA with a maximum discharge length of 10 s. The heating of the plasma is realized by injection of neutral particles and waves inside the plasma [Streibl et al., 2003]. Neutral beam injection (NBI) is the primary heating system at AUG. It delivers 20 MW of power via two injectors. Each of the injectors has four sources. Neutrals (Deuterium or Helium) are first ionized and then accelerated by an electrical grid. The remaining ionized particles are deflected, and only the beam of highly energetic neutral particles is sent into plasma. Inside the plasma, the neutral particles will first be ionized by either electron impact ionization ( $D^0 + e^- \rightarrow D + 2e^-$ ), ion impact ionisation ( $D^0 + A^Z \rightarrow D + A^Z + e^-$ ), or charge exchange ( $D^0 + A^Z \rightarrow D + A^{Z-1}$ ). Then they will gradually be equilibrated via Coulomb collisions with the bulk plasma until they are slowed down to thermal energies thereby heating electrons as well as ions. The heating via injecting ion cyclotron and electron cyclotron waves delivers up to 4 MW for each mechanism. If the frequency of the injected waves matches the gyro-frequency of the electrons or ions inside the plasma at a specified location, then the energy of electromagnetic injected wave will be transmitted to the electrons or ions. Since the frequency of the gyration depends on the magnetic field strength, which varies over the plasma radius, it is possible to localize the position where the heating power is deposited.

### 3.2 Edge diagnostics

Progress, understanding, and prediction of plasma performance depend on the acquired knowledge about relevant plasma parameters. The measured parameters can be used in real time, i.e., for plasma control, for extrapolation to larger machines,

i.e., scaling laws, or fed into theoretical models. The access to plasma parameters is enabled via suitable diagnostic tools capable of capturing dynamics of the plasma processes on sub-ms timescales which is of special importance for the plasma edge region dominated by fast transport phenomena due to the steep gradients (see chapter 2). As the plasma edge is a very narrow region ( $\sim 2$  cm) compared to the plasma radius ( $\sim 50$  cm) high spatial resolution is of particular importance here. Although a single parameter can be a good first estimate of the quality of the plasma, a proper plasma diagnosis requires a holistic approach. The parameter or parameter sets measured by the diagnostics serve as a basis for modeling of the physics processes. The interplay between experiment and modeling is of crucial importance for progress in understanding the plasma performance, especially for understanding the non-linear dynamics such as the ELM crash. In this section, the diagnostics utilized in this work are reviewed. The position of each diagnostics in a toroidal and poloidal plane of ASDEX Upgrade are shown in figure 3.1.

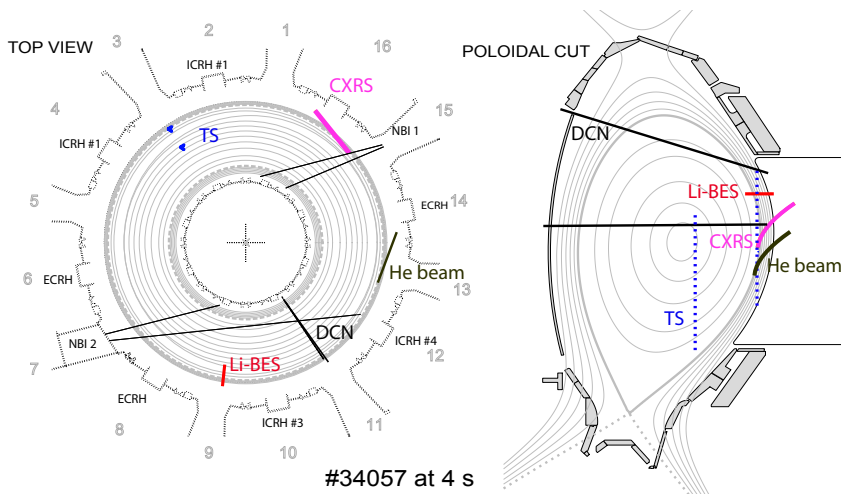


Figure 3.1: Position of various edge diagnostics utilized for this work: Charge Exchange Recombination Spectroscopy (CXRS), Li-beam Emission spectroscopy (Li-BES), thermal He-beam emission spectroscopy (He-beam) and Thomson Scattering (TS) shown from top view and in poloidal cross section of ASDEX Upgrade tokamak.



### 3.2.1 Thomson scattering

Thomson scattering (TS) is an active laser-aided diagnostic. It performs the measurements of electron density ( $n_e$ ) and electron temperature ( $T_e$ ) simultaneously, in the same plasma volume. The TS diagnostic measures the elastic scattering of an electromagnetic wave by an electron. The scattered EM wave undergoes Doppler spectral broadening. The temperature of the electrons is determined from the spectral width of the scattered signal, and the signal intensity gives information on the density of the electrons electron density ( $n_e$ ). The ASDEX Upgrade TS system has two parts; one for the edge and one for the core [Kurzan and Murmann, 2011]. Six Nd-YAG lasers with a pulse duration of 10 ns, a repetition rate of 20 Hz and energies below 1 J per pulse are available for the edge region and four for the core region of the plasma. The sampling rate of TS is 8 ms. The radial resolution of the edge system is 3 mm and of the core system is 25 mm. As other diagnostics determine either the electron temperature or the density and are usually on different locations, the primary advantage of TS diagnostic is that it can be used for the alignment of profiles relative to each other.

### 3.2.2 Lithium Beam Emission Spectroscopy (Li-BES)

This spectroscopic method of plasma diagnosis is based on the interaction between the plasma and an injected neutral lithium beam. Due to the collisions between the lithium atoms and electrons and protons, the Li atoms are excited or ionized. The emitted radiation can be measured and corresponds to radiative de-excitation of the  $\text{Li}_{2p}$  state which is the most populated excited state. The characteristic line intensity is measured along the lithium beam within the plasma. The spatial distribution of the emission line together with the collisional-radiative model allows for the determination of  $n_e$ . The injected Li beam is quickly attenuated due to atomic processes, and so it only allows measurements in the outermost 10 - 15 cm of the injection, which is the edge region. The ASDEX Upgrade system injects a neutral lithium beam with an energy of 35 keV to 60 keV from the low field side (LFS). The emission profile is viewed via 35 and 26 chords from two different optical systems with 5 to 6 mm spatial resolution along the beam, respectively. The maximum data acquisition rate is 200 kHz. Background light subtraction is realized via beam chopping typically

with 56 ms beam-on and 24 ms beam-off phases.

In this work, the Li-BES system is used as the profile diagnostics within the framework of Integrated Data Analysis (IDA) (explained later in this chapter) as well as a fluctuation diagnostic. The reliability of measured fluctuations with Li-BES is evaluated via a sensitivity study for one H-mode discharge. This evaluation is performed following the same procedure as discussed in [Willensdorfer et al., 2012]. A Gaussian with a full width at half maximum peak (FWHM) of 0.5 cm is added on

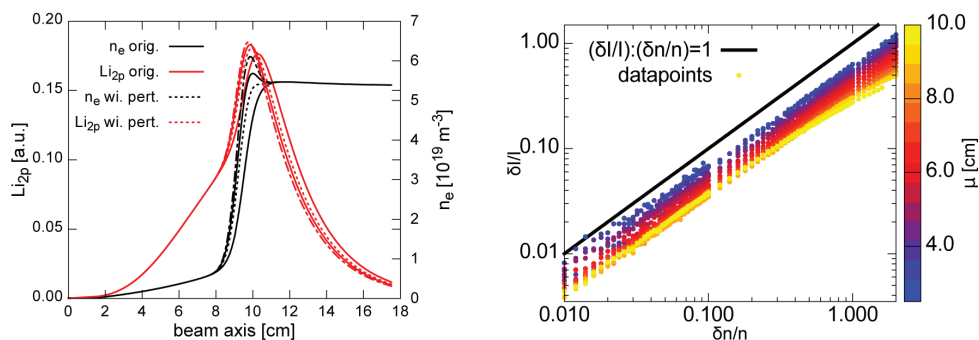


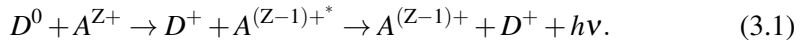
Figure 3.2: The sensitivity study for discharge # 33616. The normalized amplitude of the emission perturbation ( $\delta I/I$ ) as a function of the density perturbation ( $\delta n/n$ ) at different positions (color scaling) is shown on the right. Two cases of the density perturbation and the corresponding intensities of  $Li_{2p}$  are shown on the left. The maximum of the emission profile is at 9.5 cm. The black solid line indicates a ratio between  $\delta I/I$  and  $\delta n/n$  of 1.

top of the background profile evaluated with IDA to simulate the density perturbation observed in the experiment [Vanovac et al., 2018b]. The amplitude and the position are then varied, and the emission profile is calculated for each case until it matches the experimentally measured emission profile. Figure 3.2 (left) shows background and perturbed profiles (in black) with calculated emission  $Li_{2p}$  profiles (in red). The perturbation is located near the top of the pedestal. The calculated  $\delta I/I$  for each  $\delta n/n$  and position of the perturbation (color coded) is shown in figure 3.2 (right). The outermost Li-BES channel is at the position 0 cm (in the scrape-off layer (SOL)). The measuring position of the perturbation is at 9.5 cm (determined by the channel number) where the measured relative amplitude of the collected light is  $\delta I/I = 0.1$ .

This perturbation in the observed light intensity corresponds to a density perturbation  $\delta n/n$  of 30-80 % which is taken as the upper, and the lower limit as will be shown later in chapter 5.

### 3.2.3 Edge charge exchange

The Charge Exchange Recombination Spectroscopy (CXRS) system allows for spatially resolved measurements of the ion temperatures and poloidal and toroidal impurity velocities in the plasma. With combined poloidal toroidal measurements, it is possible to deduce the radial electric field profiles. The basic idea behind this spectroscopic method is measuring the spectral lines emitted in the process of charge exchange between neutrals and impurity ions. The impurity ions are in their excited states, and via a relaxation process they emit a photon of a specific wavelength:



The neutral atoms (D) are injected via Neutral Beam Injection (NBI). The charge exchange processes are induced between the injected neutral beam of D or He and existing impurities inside the plasma.

At ASDEX Upgrade, several CXRS systems are employed to measure the core and edge region [Viezzler et al., 2012]. The time resolution of the Edge CXRS is 2.3 ms which is not sufficient to study fast phenomena, hence is mostly used to provide profiles of the  $E \times B$  velocity. Recently, at ASDEX upgrade, a new type of spectrometer coupled to the edge CXRS system has been developed where measurements were provided with a time resolution of 50  $\mu$ s [Cavedon et al., 2017].

### 3.2.4 He beam emission spectroscopy

The steady state and transient effects can also be studied with a newly installed thermal helium beam spectroscopy [Griener et al., 2018]. This diagnostic, as the TS system, provides measurements of electron temperature and electron density simultaneously. It delivers profiles as well as fluctuation measurements. The neutral helium is locally injected into the plasma by a piezo valve, and the different line ratios are used together with a collisional-radiative model (CRM) to reconstruct  $n_e$  and

$T_e$  profiles. The profiles are reconstructed from the Scrape-off layer region into the pedestal. However, due to the ionization of the beam in the pedestal top, this region does not provide a reliable reconstruction. Therefore, the most accurate information from this diagnostic is used for measurements in the SOL and the separatrix. The radial resolution ranges from 3 mm for the outermost channels, to 7 mm for the innermost channels. The time resolution of the data is 5  $\mu$ s.

### 3.2.5 Magnetic measurements

A temporal changing magnetic field penetrating through the wire loop induces a current, and hence a voltage. The amplitude of this voltage is a quantitative measure of the change of the magnetic field. At ASDEX Upgrade multiple magnetic coils and flux loops are mounted to measure the poloidal, toroidal or radial magnetic fields [Gernhardt, 1992]. With such loops within the vessel, it is possible to observe magnetic fluctuations caused by MHD instabilities. With Mirnov loops, mode number analysis is performed as described in [Mink, 2018]. The sampling frequency of the Mirnov coils used in this work is 2 MHz.

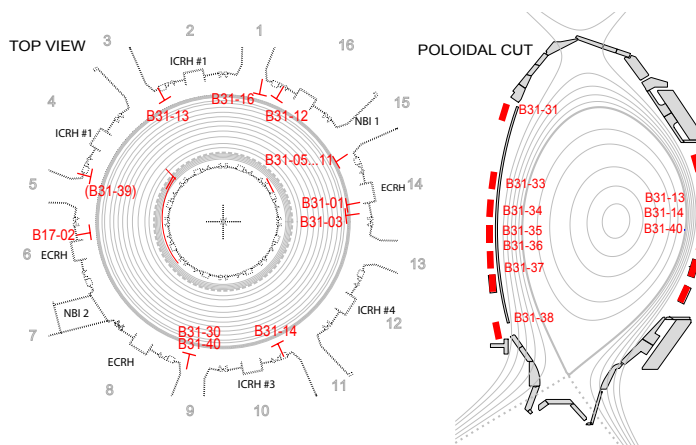


Figure 3.3: Distribution of Mirnov coils at ASDEX Upgrade mounted to measure radial and poloidal magnetic field. Figure modified from [ASDEX Upgrade web page, ].

### 3.2.6 Integrated data analysis (IDA)

At ASDEX Upgrade, a reliable simultaneous estimation of  $n_e$  and electron temperature ( $T_e$ ) profiles is obtained with an integrated data analysis (IDA) approach [Fischer et al., 2010]. The IDA concept within Bayesian probability theory takes all available raw data and their uncertainties into account. Common  $n_e$  and  $T_e$  profiles are defined and parametrized on the same magnetic coordinate system. In forward modeling, the expected measurement values are defined and then compared to the measured data and their uncertainties. The optimization algorithm determines those  $n_e$  and  $T_e$  profiles which result in the best match of modeled and measured data. The IDA concept is applied to lithium beam, interferometry (not described here), Thomson scattering and ECE (described in chapter 4). All of the diagnostic measurements are mapped onto the same magnetic coordinate system  $\rho_{\text{pol}}$  (see section 1.2). The profiles and the uncertainties are provided with a 1 ms time resolution.

## Chapter 4

# Electron Cyclotron Emission

Electron cyclotron emission (ECE) is perfectly suited for diagnosing the temperature of the plasma inside the tokamak and enables local measurements of electron temperature and electron temperature fluctuations ( $\delta T_e$ ) [Bornatici et al., 1983, N. C. Luhmann Jr. et al., 2008]. The measurements resolved along the plasma radius deliver the  $T_e$  profile (1D ECE diagnostic). First measurements of the power, polarization, and frequency spectrum of the electron cyclotron emission from a tokamak plasma are reported in [Costley et al., 1974].

When resolved in the poloidal plane, measurements provide 2D images of the plasma (ECE Imaging). In this chapter, the underlying physics that connects the measured radiation with the electron temperature, and the conditions at which this radiation is measured are discussed. An overview of the basics of heterodyne radiometry along with the detailed description of the current ECE Imaging system at ASDEX Upgrade is given. The focus of the last section is on the geometry and radiation transport effects, which are of particular importance for the interpretation of plasma edge measurements, relevant for this work.

### 4.1 Physical principles

In magnetically confined plasmas, electrons gyrate around magnetic field lines, emitting cyclotron radiation with a frequency that is proportional to the strength of

the magnetic field  $B$  [Bornatici et al., 1983]:

$$\omega_c(v) = \frac{eB(R)}{m_e c} \sqrt{1 - (v/c)^2}, \quad (4.1)$$

where  $e$  is the electric charge,  $m_e$  the electron rest mass,  $c$  the speed of light. For the radiation propagating perpendicular to the magnetic field (quasi-perpendicular propagation) the only kinetic broadening of the emitted line is relativistic broadening. Additionally, in the case of oblique propagation, the velocity component parallel to the magnetic field  $B$  has to be considered, leading to Doppler broadening:

$$\omega_{ce} = n\omega_c + k_{\parallel} v_{\parallel}. \quad (4.2)$$

Which of the broadening effects is dominant, depends on the plasma parameters and the geometry of the detection system. In most cases, for the high confinement plasmas at ASDEX Upgrade which are of interest for the work presented here, the two effects appear combined. The ECE Imaging system, used as the main diagnostic tool in this thesis, has a toroidal observation angle, that, as will be shown later in this chapter, enhances the Doppler broadening.

The magnetic field in a tokamak is a function of the major radius  $R$  ( $B_t = B_0 R_0 / R$ ), and the frequency of the electron cyclotron emission is a function of the magnetic field (see eq. (4.1)). Thus, the correlation between the frequency and position allows for the radially resolved measurements of the electron cyclotron radiation. The  $n^{\text{th}}$  harmonic will therefore be emitted from the radial position  $R$ :

$$R = \frac{neB_0R_0}{m_e\omega_{ce}}. \quad (4.3)$$

Equation 4.3 suggests that radiometry is a point-like measurement. However, this is not the case (see eq. (4.2)), and the measurement instead corresponds to a finite observation volume. At sufficiently high density and temperature, the plasma becomes optically thick such that the radiation of the optically thick harmonics reaches the black body radiation:

$$I_{\text{ECE}}(\omega, R) = I_{\text{BB}}(\omega, R) = \frac{\omega^2 T_e}{8\pi^3 c^2}. \quad (4.4)$$

Usually, in a tokamak, this radiation is of the order of 100 GHz and is in the mm wavelength range. For typical ASDEX Upgrade discharges with  $B_t = 2.5$  T, on axis, the electron cyclotron frequency of the second harmonic  $f_{ce} = 2\omega_{ce}/2\pi$  is 140 GHz. This is precisely the frequency of the electron cyclotron resonance heating (ECRH) system used for central heating of typical plasma discharges in ASDEX Upgrade. The optical depth  $\tau$  is a measure of the plasma absorption. The quantitative estimate of the optical thickness is the integrated absorption coefficient along the beam path.

$$\tau(\omega) = \int_0^R \alpha(\omega) ds, \quad (4.5)$$

where  $\alpha$  is the absorption coefficient and  $s$  is the path along the beam. For  $\tau \gg 1$  the plasma is optically thick so the intensity of the electron cyclotron emission is equal to that of a black body, and eq. (4.4) holds. In this case absorption and emission are equivalent processes

$$\frac{j(\omega)}{\alpha(\omega)} = I_{BB}(\omega). \quad (4.6)$$

In the case of a low optical depth ( $\tau \ll 1$ ) the wall reflections must be taken into account [Clark, 1983]. The emitted radiation  $I_0$  will reach the observer with intensity:

$$\frac{I_{BB}(\omega)}{I_0(\omega)} = \frac{1 - e^{-\tau}}{1 - \rho_{\text{refl}} e^{-\tau}}, \quad (4.7)$$

and the absorbed intensity will be reduced. Therefore in the case of an optically thin region the plasma is not fully absorbing and the radiation temperature  $T_{\text{rad}}$  no longer equals the electron temperature  $T_e$ :

$$I_{BB}(\omega) = \frac{\omega^2 T_{\text{rad}}}{8\pi^3 c^2}. \quad (4.8)$$

The optical depth of second harmonic extraordinary mode (X-mode) radiation (explained in the following section), used for diagnosing the electron temperature in ASDEX Upgrade, is proportional to the product of  $T_e$  and  $n_e$ . As those are low at the plasma edge, the optical depth is proportionally low. Therefore, inferring  $T_e$  from the radiation temperature ( $T_{\text{rad}}$ ) at the plasma edge is not unambiguous.



## 4.2 Wave propagation in magnetized plasmas

Once emitted, the radiation from the gyrating electrons needs to propagate freely through the plasma and reach the detection point to be measurable. On its way, the wave can be absorbed by the plasma, refracted from a region of higher density or reflected from a cut-off layer. In the following, we present the conditions at which those events occur. Derivations of the dispersion relations can be found in the literature such as [Bornatici et al., 1983, Chen, 1984]. Propagation of the waves through the magnetized plasma can be described by the Maxwell equations for electric  $\mathbf{E}(\mathbf{r}, t)$  and magnetic  $\mathbf{B}(\mathbf{r}, t)$  fields taking into account the plasma response. This yields a dispersion relation in the form:

$$\mathbf{k} \times \mathbf{k} \times \mathbf{E} + \frac{\omega^2}{c^2} \bar{\epsilon} \mathbf{E} = 0, \quad (4.9)$$

where  $\mathbf{k}$  is the wave vector and  $\bar{\epsilon}$  is the dielectric tensor containing the plasma response. The simplest form of the solutions come from the *cold plasma approximation* where the ion motion is ignored since the ion mass is much larger than the mass of the electron,  $m_i \gg m_e$ . The only species taken into account are the electrons and their thermal velocity is much smaller than the phase velocities of the propagating waves ( $v_t \ll c$ ). Then, the solution of eq. (4.9) is given as:

$$N^2 = 1 - \left(\frac{\omega_p}{\omega}\right)^2 \frac{2(\omega^2 - \omega_p^2)}{2(\omega^2 - \omega_p^2) - \omega(\sin^2 \theta \mp \rho)}, \quad (4.10)$$

with

$$\rho \equiv \sin^4 \theta + 4 \left(\frac{\omega^2 - \omega_p^2}{\omega \omega_{ce}}\right)^2 \cos^2 \theta, \quad (4.11)$$

which is the so called Appleton-Hartree formula for the refractive index.  $N$  is the refractive index defined as  $N \equiv kc/\omega$ ,  $\theta$  is the angle between the propagation vector  $\mathbf{k}$  and the direction of the magnetic field  $\mathbf{B}_0$ . Here  $\omega_p$  is the electron plasma frequency, defined as:

$$\omega_p = \sqrt{\frac{n_e e^2}{\epsilon_0 m_e}}. \quad (4.12)$$

The electron plasma frequency originates from the oscillation of the electrons around the ions with the electric field as a restoring force. There are two different types of propagation defined by the angle  $\theta$ . Perpendicular ( $\mathbf{k} \perp \mathbf{B}_0$ ) propagation is favourable because the emission is local. Whenever there is an angle different from  $\pi/2$  between  $\mathbf{k}$  and the direction of the magnetic field  $\mathbf{B}$  we have oblique wave propagation  $\theta \angle (\mathbf{k}, \mathbf{B})$  and some of the information on the parallel component is captured. Further more, whenever the refractive index goes to zero  $N \rightarrow 0$  ( $|\mathbf{k}| \rightarrow 0$ ), the propagating wave encounters a cut-off and is totally reflected. If  $N \rightarrow \infty$  radiation hits a resonant surface ( $|\mathbf{k}| \rightarrow \infty$ ) and is absorbed. For the wave to be able to propagate to the detection point, it must be neither reflected nor absorbed. However, since the plasma has a refractive index  $N$  between zero and one, this variation in the refractive index bends the beam, and the path can deviate from a straight line and introduce uncertainties in the measurement positions. In the Appleton-Hartree formula the symbol  $\mp$  describes two different modes of propagation. The minus sign describes the Ordinary mode (*O*-mode) of propagation where the electromagnetic wave oscillates parallel to the external magnetic field ( $\mathbf{E} \parallel \mathbf{B}_0$ ). For perpendicular wave propagation ( $\theta = \pi/2$ ) eq. (4.10) reduces to  $N^2 = 1 - (\omega_p/\omega)^2$ . Evaluating  $N \rightarrow 0$ , the only cut-off frequency for the *O*-mode is the plasma frequency  $\omega_p$ . The positive sign in the Appleton-Hartree formula corresponds to *X*-mode where the polarization of the electric field is perpendicular to the magnetic field ( $\mathbf{E} \perp \mathbf{B}_0$ ). Again, assuming that the propagation is perpendicular to the magnetic field ( $\mathbf{k} \perp \mathbf{B}_0$ ) one gets:

$$(N_{\perp}^X)^2 = 1 - \left(\frac{\omega_p}{\omega}\right)^2 \frac{\omega^2 - \omega_p^2}{\omega^2 - \omega_c^2 - \omega_p^2}. \quad (4.13)$$

From eq. (4.13) the cut-offs are derived to be at:

$$\omega_{R,L} = \sqrt{\omega_p^2 + \frac{\omega_c^2}{4}} \pm \frac{\omega_c}{2}. \quad (4.14)$$

The upper-hybrid ( $\omega_{UH}$ ) is a resonant frequency:

$$\omega_{UH} = \sqrt{\omega_c^2 + \omega_p^2}. \quad (4.15)$$

The radial dependencies of the cyclotron frequency  $\omega_{\text{CE}}$ , second  $2\omega_{\text{CE}}$  and third  $3\omega_{\text{CE}}$

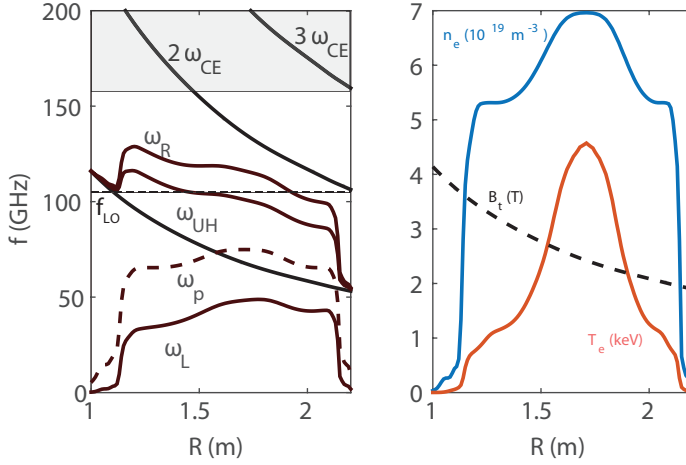


Figure 4.1: a) Radial dependence of the first ( $\omega_{\text{CE}}$ ), second harmonic ( $2\omega_{\text{CE}}$ ) and third harmonic ( $3\omega_{\text{CE}}$ ) of the cyclotron frequency for a typical H-mode plasma discharge at ASDEX Upgrade. The shaded area represents the region of the harmonic overlap, preventing measurements from the LFS of the 2nd harmonic for frequencies larger than 140 GHz. The frequencies of the local oscillators used by the ECE-imaging systems are also shown as horizontal dashed lines around  $f_{\text{LO}} = 106$  GHz. Cut-off frequencies for 2<sup>nd</sup> harmonic X-mode  $\omega_{\text{R}}$  and  $\omega_{\text{L}}$  are presented in grey as well as the resonant frequency for 2<sup>nd</sup> harmonic X-mode,  $\omega_{\text{UH}}$ . b) Profiles of  $n_e$ ,  $T_e$  and  $B_t$ .

harmonic  $3\omega_{\text{CE}}$  for the O- and X-mode are shown in figure 4.1(a) for typical high-confinement mode (H-mode) plasma parameters, with  $n_e$  and  $T_e$  profiles at ASDEX Upgrade shown in 4.1(b). The plasma frequency  $\omega_p$ , which is the cut-off frequency for the O1-mode, is also shown. The frequency  $2\omega_{\text{CE}}$  of the O2 radiation is not in cut-off but is optically thin. On the other hand, the  $\omega_{\text{CE}}$  radiation is entirely in cut-off for X1 -mode, while the  $2\omega_{\text{CE}}$  and  $3\omega_{\text{CE}}$ , for the X2 and X3 radiation respectively, are not. However, due to harmonic overlap, shown as the shaded region for frequencies from 140 GHz and above, the X2 high-field side (HFS) measurements are not feasible from the low-field side (LFS) at ASDEX Upgrade. In principle, measurements of the X2 radiation for the frequency range above 140 GHz are possible from the HFS. The X2 radiation has two different cut-off branches: a branch with a right-hand rotation

of the vector  $\mathbf{E}$ ,  $\omega_R$  and one with the left-hand rotation  $\omega_L$ . The cut-off frequency acts as a high-pass filter. The X2 can, therefore, propagate above  $\omega_L$  and  $\omega_R$ , but it cannot propagate in the region between  $\omega_{UH}$  and  $\omega_R$ . It can be seen that the fundamental harmonic of X-mode hits the resonance  $\omega_{UH}$  which means it is absorbed; therefore it cannot be used. The X2 can propagate freely to the detection point for frequencies higher than  $\omega_R$  and does not encounter absorption or reflection on its way. Probing frequencies of both local oscillators are shown ( $f_{LO}$ ).

## 4.3 ECE radiometry

### 4.3.1 Basics of the heterodyne detection

For typical plasma and machine parameters at ASDEX Upgrade, ECE radiation suitable for diagnosing the plasma is in the range of 100 - 140 GHz (see figure 4.1). These frequencies are too high for processing; therefore intermediate transformations to lower frequencies are necessary before the signal is detected. This process is done using a heterodyne scheme, commonly used in microwave diagnostics [Hartfuss et al., 1997]. The block diagram of a heterodyne detection system is shown in figure 4.2. In the mixing element M, the radio frequency RF signal from the plasma is mixed with emission from a local oscillator LO. The resulting signal is the beat wave in the intermediate frequency range. The mixing element M is linear in the sense that the resulting IF signal is proportional to that of the RF signal. In the IF section, the signal is adjusted to satisfy the requirements of the detector D. It is first amplified  $G_{if}$  to use the whole dynamic range of the sensor and then is bandpass filtered  $B_{if}$ . In the video section, the signal is low pass filtered  $B_v$  to match the sampling frequency of the data acquisition system. At a given LO frequency  $f$  two different RF input frequencies result in the same intermediate frequency  $f_0$ . If the ECE receiver is sensitive to both of these sideband frequencies, it is called a double-sideband receiver. If the input frequency is filtered with a sideband filter, the receiver is sensitive to one sideband only and is called a single-sideband receiver. Both possible RF signals are symmetric to the LO signal, and the remaining sideband is called the image frequency.

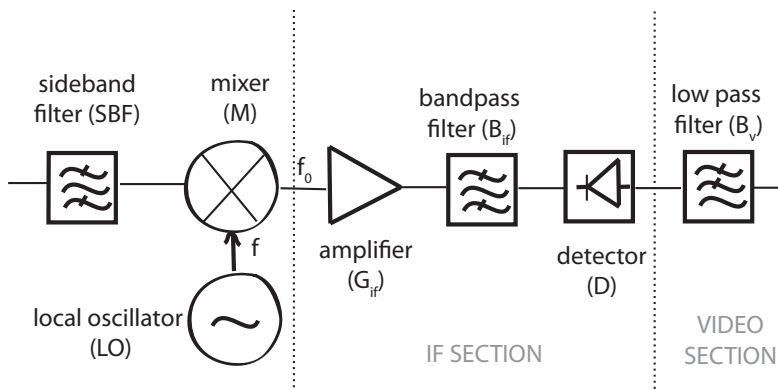


Figure 4.2: Diagram showing the basic scheme of heterodyne detection. The signal coming from the plasma is first filtered using a sideband filter (SBF), then it is mixed in the Mixer (M) with the signal from a local oscillator (LO) with frequency  $f$ . The output of the mixer is in the Intermediate Frequency (IF) range. In the IF section the signal with frequency  $f_0$  is amplified ( $G_{if}$ ), bandpass filtered ( $B_{if}$ ) and detected (D). Video filtering by a low pass filter ( $B_v$ ) is the last step in the conversion process.

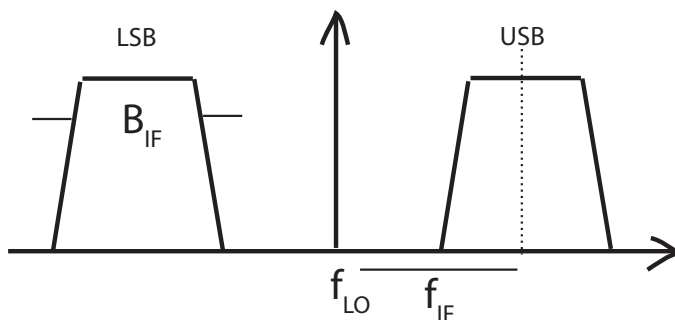


Figure 4.3: The IF frequency  $f_{IF}$  and the IF bandwidth  $B_{IF}$  together with the frequency of the local oscillator  $f_{LO}$  define the sensitivity range of the heterodyne receiver. A double-sideband ECE receiver is sensitive to both upper-sideband (USB) and the lower-sideband (LSB) radiation.

#### 4.4 ECE based diagnostics at ASDEX Upgrade

In the following section, the basic characteristics of the 1D ECE radiometer, newly installed correlation ECE diagnostic and the main tool of this work, ECE Imaging,

are introduced. Their respective positions in poloidal and toroidal plane are given in figure 4.4.

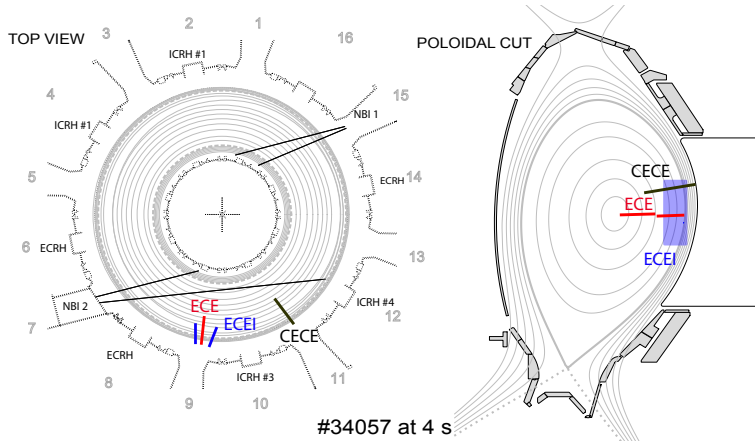


Figure 4.4: Position of Electron Cyclotron Emission (ECE) diagnostic in red, Electron Cyclotron Emission Imaging (ECE imaging) diagnostic in blue and Correlation Electron Cyclotron Emission (CECE) diagnostic in black shown from top view and in poloidal cross section of ASDEX Upgrade tokamak.

#### 4.4.1 Profile ECE

The profile ECE diagnostic at ASDEX Upgrade uses a heterodyne radiometer with 60 available channels. It measures the second harmonic X-mode radiation with 1 MHz sampling rate. For a standard 2.5 T field configuration, the radial resolution of the edge channels is about 5 mm. The intermediate frequency broadening for each edge channel is 300 MHz. With an IF bandwidth of 600 MHz the core channels have a spatial resolution of about 12 mm. Profile ECE is absolutely calibrated. In this work, a 1D ECE diagnostic is used for profile and fluctuations measurements.

#### 4.4.2 Correlation ECE (CECE)

A Correlation Electron Cyclotron Emission (CECE) diagnostic [Freethy et al., 2016] at ASDEX Upgrade, utilizes cross-correlation in order to resolve small, broadband temperature fluctuations on the account that the noise between the two signals will

be decorrelated while the actual correlated signal corresponds to the temperature fluctuations. This way, the turbulence levels, not measurable with classical ECE nor ECE Imaging, are captured. The CECE system is used in this work as a complementary confirmation to the ECE Imaging and the ECE observations. It also has the highest radial resolution among the three diagnostics. It resolves 2-3 mm of the plasma radius.

#### 4.4.3 ECE Imaging (ECE imaging)

The first installed ECE Imaging system on ASDEX Upgrade is a follow up of the system at the TEXTOR tokamak [Classen, 2007]. The ECE Imaging system is placed in sector 9 of ASDEX Upgrade on top of the standard 1D ECE diagnostic. Both diagnostics share the same vacuum window and part of the optical components. In contrary to the standard 1D ECE diagnostic, ECE Imaging enables 2D measurements, resolved radially and vertically. Each vertical position in the plasma corresponds to a single line-of-sight (LOS), and it is succeeded by quasi-optical imaging of the radiation onto an array of detectors. The schematic explaining the difference between 1D ECE and ECE imaging is shown in figure 4.5. An additional ECE imaging system

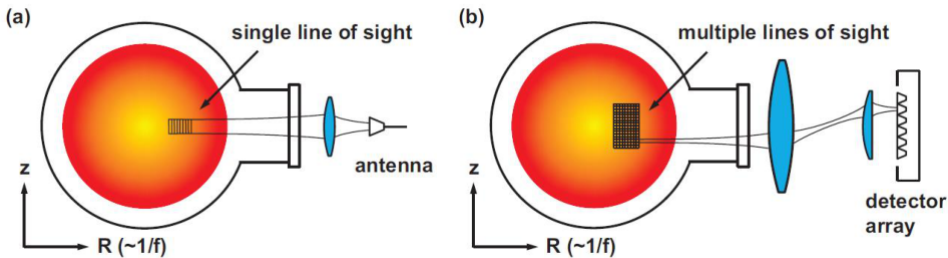


Figure 4.5: Illustration of the optical path for a) Conventional 1D radiometer as a method of measuring  $T_e$  profiles. b) ECE imaging case where optical imaging of multiple radiometers enable vertically resolved  $T_e$  measurements. Note that the optical path for the ECE imaging system is not realistic, for better view see figure 4.6

has been installed with characteristics that match the existing one. The upgraded ECE imaging system [Classen et al., 2014] has a total of 288 channels. Each array has eight radial channels. Array 1 has 16 vertical LOSs, and array 2 has 20 vertical

LOSs, respectively. The vertical coverage of array 1 is about 40 cm and 50 cm for the array 2. The radial extension of the ECE imaging window for both arrays is about 10 cm. For the typical edge settings ( $B_t = 2.5$  T and system focused at the edge) the toroidal viewing angle of array 1 is  $\sim 8^\circ$  while for array 2 it is  $\sim 6^\circ$ . The poloidal cross section of the ECE Imaging system at ASDEX Upgrade is given in figure 4.6.

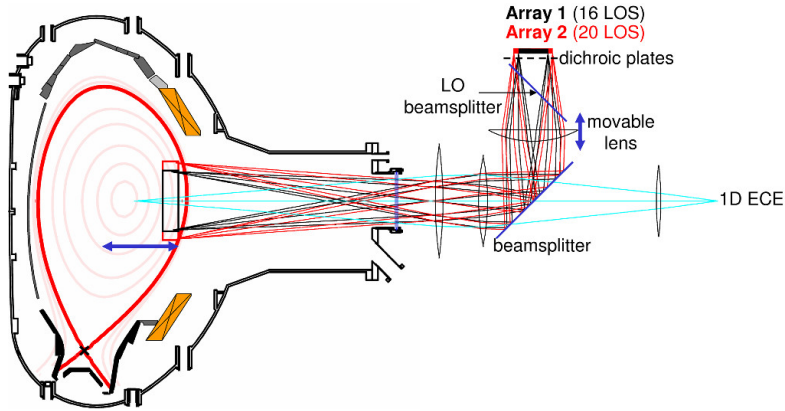


Figure 4.6: Overview of the optical path constructed with a lens set up of ECE and ECE imaging systems. The first two lenses after the vacuum window are common for both ECE and ECE imaging. Hence, the two diagnostics share the same optical path in this section. The first beam splitter separates the signal into two portions. The portion of the signal that is reflected goes into two arrays of detectors for the ECE Imaging. With the movable lens, it is possible to shift the focus in the plasma. Figure taken from [Classen et al., 2014].

### Front end optics

The first front side optics consists of three high-density polyethylene lenses. ECE imaging shares the two lenses with the 1D ECE radiometer. The signal is split into two portions with a beam splitter (with approximately 50/50 % reflection/transmittance). The ECE imaging half is reflected through movable lenses upwards. These movable lenses consist of two halves that can move, changing the focus of the beam, of both arrays, independently. The focus can be changed between the low field side (LFS) plasma edge and the plasma center to match the measurement position. The frequency



of the local oscillator (LO) determines this position. Filtering out the lower-sideband of the signal is performed using dichroic plates as a high-pass filter. The choice of the dichroic plates is limited and depends on the experimental requirements. There are five plates available for array 1 with cut-off frequencies of 99.1, 105.0, 111.7, 115.6 and 120.6 GHz and six plates for array 2 with a cut-off at 100, 105, 110, 115, 120 and 125 GHz. The choice of the LO frequency is limited to those that match the cut-off frequencies of the dichroic plates.

The whole system is protected from the unabsorbed stray radiation of the 140 GHz ECRH system using three notch filters with a combined rejection rate of 60 dB. Operation with unabsorbed 105 GHz ECRH radiation is also possible for the frequency of LOs above 105 GHz. In this case, dichroic plates are cut off for this radiation.

### **Local oscillators**

The microwave radiation from the LOs is imaged onto the two arrays of detectors independently. The signals from the local oscillators need to be in the form of elongated Gaussian beams to irradiate the entire array of diodes. This projection for array one is made using two lenses and two mirrors. Array one uses an external beam splitter to couple the signal from the local oscillator to the plasma signal. The local oscillator for array one is a synthesizer with integrated amplifier multiplier chain (AMC) and has an operational range of 100 to 130 GHz. It delivers a minimum of 100 mW of output radiation, but this output radiation is not a constant function of frequency. It is important to know 'sweet spots' of the synthesizer - points with the highest output power, and be aware that those can change over the lifetime of the synthesizer due to mechanical oscillations. Array 2 uses a backward wave oscillator (BWO) as LO source with a tunable frequency in the range of 90 - 140 GHz. The power output is about 100 mW. The output power of the BWO is coupled to the RF source using four mirrors and two lenses.

### **IF section and detection**

After the first down-conversion step, the signal from each detector (diode) is transmitted by 18 meters long coax cables to the IF section. One detector corresponds to one line of sight, hence one vertical point in the plasma. Each IF module consists of two

circuit boards enclosed in a shielded box. The first board is an RF circuit where the input signal is split into eight portions. Each portion of the signal mixes with a (voltage controlled) LO. For the first array the  $f_{LO}$  is in the range of 2.4-8 GHz, and for the second array  $f_{LO} = 3-8.6$  GHz with increments of 800 MHz for both arrays. Array 2 has an option of decreasing the inter-channel spacing to 550 MHz which would correspond to a  $f_{LO}$  in the range of 3.75-7.6 GHz. This down-conversion process is double-sided and collects the signal from both sides of the central LO frequency  $f_{LO}$  (see figure 4.3). Each portion corresponds to a single radial position in the plasma. A 6-bit attenuator on the RF board provides up to 31.5 dB of attenuation equally applied to all eight channels to account for the large variations in the signal levels. External DIP switches adjust the attenuation levels on the front of the panel. The second board is an IF circuit which has eight circuits to rectify the signal from the RF board and form eight video signals. Signals are amplified and bandpass filtered in a way that the signal remains proportional to the ECE signal level. Attenuation of the signals within the IF board can be controlled with internal DIP switches that provide 15 dB of gain control, and are adjusted to compensate for changes in the pre-amplifier gain and can be applied to each channel individually. However, bandpass filtering around the central LO frequency translates into an effective IF bandwidth. The bandwidth of the IF section of array 1 is 700 MHz and 390 MHz for array 2. The radial resolution of the system is however determined by the plasma broadening effects as well as the IF bandwidth. Signals are detected (D) and video filtered to match the sampling rate of the data acquisition system. Video filtering is controlled by a tenth-order switched capacitor filter with cut-off frequencies of 25, 50, 100, 200, or 400 kHz. Finally, a 14-bit data acquisition system collects the data sampled at 500 kHz for the entire duration of the discharge (generally up to 10 s).

### **Signal-to-noise ratio**

In thermal equilibrium, under the assumption that the plasma is optically thick, the radiation temperature coincides with the electron temperature within the error bars determined by the statistical fluctuations of the signal rECE imaged by the ECE radiometer. These fluctuations are associated with the wave noise because the emission from the plasma is a superposition of many incoherent waves, and is called

thermal noise. Usually, this wave noise dominates over the instrumental noise. The level of thermal noise is determined by the spatial  $B_{IF}$  and temporal  $B_V$  bandwidths of the system [Hartfuss et al., 1997]:

$$\frac{\delta T}{T} = \sqrt{\frac{2B_V}{B_{IF}}}. \quad (4.16)$$

It can be seen from eq. (4.16) that increasing  $B_V$  (better time resolution) and decreasing  $B_{IF}$  (better spatial resolution) increases the thermal noise level.  $B_V$  settings for both arrays are 200 kHz, whilst  $B_{IF}$  is 700 MHz for array 1 and 390 MHz for array 2. This translates into a relative noise level for array 1 of 2.4 % and for array 2 of 3.2 %.

### Radial resolution of the ECE at the plasma edge

The radial resolution of the ECE Imaging system is set by the IF broadening  $B_{IF}$  and relativistic and Doppler broadening. In first approximation, taking only the IF broadening, the frequency width of a single ECE imaging channel is evaluated as:

$$B_{IF} = n \frac{eB_0 R_0}{m_e (R + \Delta R)} - n \frac{eB_0 R_0}{m_e R} \approx - \frac{neB_0 R_0}{m_e R^2} \Delta R. \quad (4.17)$$

Array 1 has  $\Delta R = 1.2$  cm, and  $\Delta R = 0.6$  cm for the array 2. With an additional Doppler and relativistic broadening, the radial resolution of the ECE Imaging degrades. This is explained in the following section.

## 4.5 Mode analysis limitations of ECE imaging & ECE measurements at the plasma edge. \*

As described earlier the Electron Cyclotron diagnostic is widely used to measure the  $T_e$  and  $\delta T_e$  profiles [Hartfuss et al., 1997]. The electron cyclotron emission imaging (ECE imaging) diagnostic [Classen et al., 2014] uses the same principle, with the difference that it has multiple lines of sight (LOS)s, which allow measurements of  $T_e$  and  $\delta T_e$  in a poloidal plane. At ASDEX Upgrade, both diagnostics measure

---

\*Part of the work presented in this section is to appear on *EPJ Web of Conferences* under the title 'Mode analysis limitations of ECE imaging & ECE measurements at the plasma edge'

the  $X$ -mode microwave intensity, which can be converted into a radiation temperature  $T_{\text{rad}}$ . The calibrated  $T_{\text{rad}}$  can, in many cases, be directly related to  $T_e$  at the measuring position defined solely by the strength of the toroidal magnetic field. The measurement position defined in this way is called 'cold' resonance position. However, in specific plasma scenarios and plasma regions, the microwave radiation does not originate from the cold resonance. This ambiguity is of particular importance for measurements at the plasma edge. Various types of limitations of ECE radiometry at the plasma edge such as low and high-density limits, relativistic and Doppler broadening effects are reviewed in [Suttrop and Peeters, 1996]. Shine-through in ECE measurements at ASDEX Upgrade is studied in detail in [Rathgeber et al., 2013, Denk et al., 2017] and for the DIII-D ECE imaging system in [Tobias et al., 2012]. The ECE imaging diagnostic at ASDEX Upgrade has an oblique observation angle, and hence an enhanced Doppler shift of the emission frequency. It also suffers from an even higher relativistic downshift of the respective frequencies due to the oblique angle [Willensdorfer et al., 2016] which strongly limits the usability of ECE Imaging in the SOL. However, it has been shown that strong perturbations such as density filaments in the SOL can be detected but the reconstruction of an accurate  $T_e$  profile from  $T_{\text{rad}}$  is, in general, not possible [Vanovac et al., 2016]. In [Vanovac et al., 2018b] the slow variations in density measured with Lithium Beam Emission Spectroscopy (Li-BES)[Willensdorfer et al., 2012] are found to influence the changes in the  $T_{\text{rad}}$  signal measured by ECE imaging and ECE diagnostics in the pedestal. Hence, the knowledge of  $n_e$  plays a vital role in the interpretation of the ECE imaging measurements in this region. The same effect has been studied for the marginally optically thick plasmas at KSTAR [Ayub et al., 2017]. In this work, the response of the ECE and ECE imaging system to variations in the  $n_e$  profile in the optically thick ( $\tau > 3$ ) region is studied. To assess the emission volume for each channel and interpret the radiation temperature  $T_{\text{rad}}$  we use an electron cyclotron radiation transport model. In this way, detailed knowledge on the position of the channels and  $T_{\text{rad}}$  associated with it is acquired. This information is essential for the interpretation of measured variations in  $T_{\text{rad}}$ . Since the  $O$ -mode contribution to the ECE radiation is not perfectly blocked by the polarization filter at the ECE antennas in ASDEX Upgrade, the radiation transport model was extended to take this effect into account. To test the modeling of the  $O$ -mode contribution, a case was

examined where the  $O$ -mode contribution to the measured  $T_{\text{rad}}$  becomes significant. The results on the  $O$ -mode contribution can be found in [Vanovac et al., 2018a]. At ASDEX Upgrade the radiation transport model is routinely used for interpreting measurements of ECE and ECE imaging diagnostics [Denk, S. S. et al., 2017]. The radiation transport model accounts for the geometry of the detection systems and radiation transport effects. For a specific frequency, ray tracing is performed, and the radiation transport equation is solved backward until the ray reaches the antenna. This model can treat both  $X$ - and  $O$ -mode polarization.

#### 4.5.1 Geometry effect: Doppler shift-broadening

The radiation transport model delivers information on the location of the emitted radiation associated with a certain channel and the  $T_{\text{rad}}$  associated to that location. The lo-

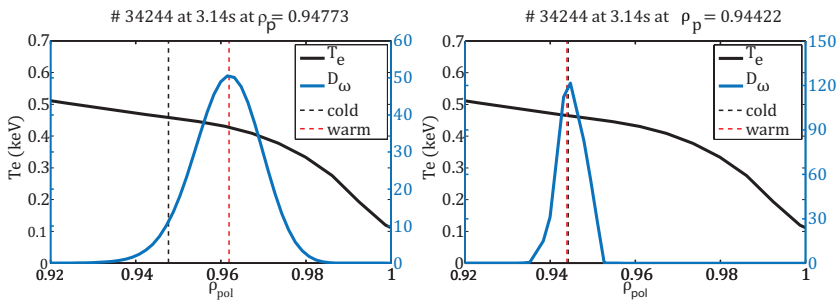


Figure 4.7: ASDEX Upgrade discharge # 34244 at  $t = 3.14$  s: Midplane edge channels of ECE imaging (left) and profile ECE (right) with frequency  $f = 110.4$  GHz and  $f = 110.27$  GHz, respectively. The cold resonance position is determined by the magnetic field strength and is shown as a black dashed line. The birthplace distribution of the observed intensity ( $D_\omega$ ) is shown in blue. The peak of the  $D_\omega$  represents the warm resonance of a channel. The IDA  $T_e$  profile is shown as a solid black line.

cation of the emitted radiation is determined as the peak of the birthplace distribution of the observed intensity ( $D_\omega$ ) (see figure 4.7), defined in [Denk, S. S. et al., 2017]. This peak is labeled as the 'warm' resonance position which can differ from the 'cold' resonance position. The cold resonance  $\omega = neB/m_e$ , where  $n$  is the harmonic of

the cyclotron emission, is determined solely by the strength of the magnetic field. The characteristic positions for a single ECE imaging midplane channel of frequency  $f = 110.27$  GHz are shown in figure 4.7 (left). The warm resonance (peak in  $D_\omega$ ) is shifted outwards in comparison to the cold resonance (black dashed line). The measured electron emission does not originate from a single location but rather from a broad portion of the plasma determined by the width of  $D_\omega$ . The most important broadening effects in the case of the ECE imaging system are instrumental and Doppler broadening. The Doppler broadening originates from the oblique observation angle of the ECE imaging diagnostic. The outward shift towards lower temperatures and lower magnetic field compared to the cold resonance (black dashed line) is about 0.5 cm which is half of the radial resolution of this channel (1.1 cm). The ECE system, on the other side, has almost negligible Doppler broadening (see figure 4.7 right). The observation angle is nearly perpendicular to the magnetic field lines. The radial resolution of this ECE channel, determined by the width of  $D_\omega$ , is about 5 mm. However, due to a small divergence of the antenna pattern, a slight Doppler broadening is also observed for the case of the ECE system. The distortion of ECE Image channels due to the Doppler shift is demonstrated comparing two simulations for the ECE Imaging channels, shown in figure 4.8. One case assumes no toroidal observation angle (figure 4.8(a)), and another considers the real geometry (figure 4.8(b)). The innermost channels are Doppler-shifted towards lower temperatures as shown in figure 4.8(b). The difference between the cold and the warm resonance for the most inner channel of the central LOS is about 1.5 cm which is of the order of the radial resolution of the diagnostics.

### 4.5.2 Shine-through emission

In H-mode discharges at ASDEX Upgrade, usually, temperatures of several hundreds of eV are measured in the ECE Imaging (see figure 4.9) and ECE channels with resonances near the scrape-off layer (SOL). This is physically not possible because the strong parallel heat transport would cause an immediate plasma extinction [Pitcher et al., 1997]. The origin of this enhanced emission outside the confined region is due to the relativistic mass increase of the electrons emitted at higher harmonics. For demonstration, a synthetic ECE Imaging  $T_{\text{rad}}$  profile mapped onto

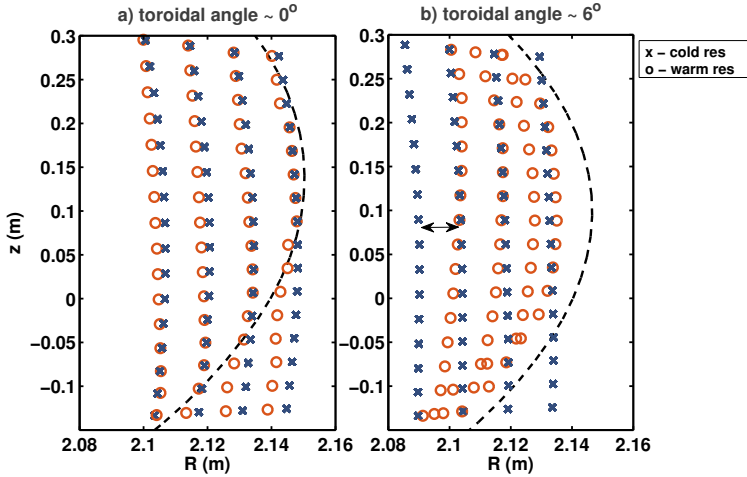


Figure 4.8: Study of the geometry effect on the ECE imaging system via modeling the cold and the warm resonances for a) perpendicular observation angle to the magnetic field lines, b) realistic geometry where the system has the toroidal observation angle of 6 degrees. The effect of the toroidal shift is seen in nearly all depicted channels. The bandwidth is not included in the modeling.

the cold resonances is shown in figure 4.9. The  $T_e$  profile obtained with Integrated Data analysis (IDA) [Fischer et al., 2010] is also shown. Inside the confined region radiation temperature is lower than the electron temperature  $T_{\text{rad}} < T_e$  due to Doppler shifted frequencies (see section above). Outside the confined region, the emission is strongly enhanced due to the relativistic frequency downshift. The birthplace distribution function (not shown here) suggests that the signal measured with those channels originates from the pedestal top and SOL simultaneously. Hence, those channels are discarded from further analysis.

### 4.5.3 Density variation

Outward bending of the observation line occurs due to the variation in refractive index ( $0 < N < 1$ ). Variations in the density profile can lead to oscillations in the position of the observation volume, leading to fluctuations in the temperature measurements [Clark, 1983]. This effect is studied by introducing a density profile variation, and

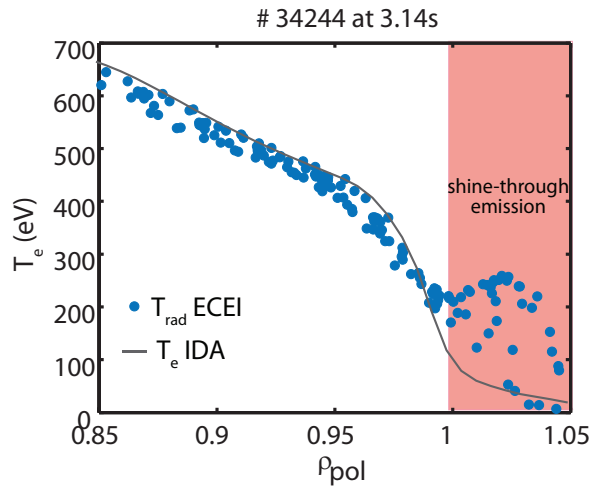


Figure 4.9: Synthetic ECE imaging  $T_{\text{rad}}$  mapped onto the cold resonance positions. A pronounced shine-through peak is observed outside the separatrix. The channels inside the separatrix underestimate temperature due to the outward Doppler shift of the resonances.

then the radiation transport model is applied to the case of the discharge # 34244 at 3.14 s. This discharge features strong inter-ELM activity in the low-frequency range measured as  $n_e$  and  $T_e$  fluctuations simultaneously. A background density profile is modified and used as the input for the electron cyclotron radiation transport forward model. A modified profile consists of the background profile with 10% Gaussian perturbation added on top of it. The forward modeling of the electron cyclotron radiation is performed for all ECE imaging and ECE channels. The  $T_e$  profile and the equilibrium mapping are kept the same for the two cases. The  $n_e$  and  $T_e$  profiles are shown in figure 4.10. The profiles are obtained with Integrated Data Analysis (IDA) within the framework of Bayesian probability theory [Fischer et al., 2010].

The background profile is displayed as a solid black line in figure 4.10. With added Gaussian perturbation on top of the background profile, we obtain the modulated  $n_e$  profile displayed in fig. 4.10 as a black dashed line. The position of the largest change in density profile corresponds to the position of the ECE and ECE-I channels that measure the mode activity. In the following, we use the notation as case 1 and



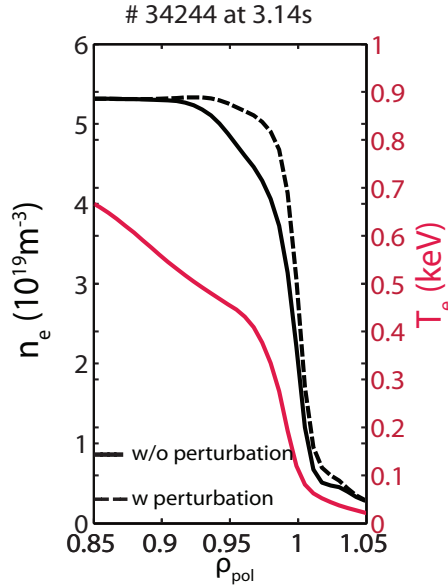


Figure 4.10: ASDEX Upgrade shot #34244 at 3.14 s: Input profiles of  $T_e$  (red) and  $n_e$  (black) used to model the response of ECEI and ECE channels to the presence of the density modulation. Background density profile is shown as a black solid line while the perturbed density profile is displayed as black dashed line. The temperature profile is kept the same for the two cases.

case 2. For case 1 we use the background density profile (black solid line in fig. 4.10), and for the case 2 we use a density profile with added perturbation (shown as dashed black line in fig. 4.10). Figure 4.11(a) shows the synthetic  $T_{\text{rad}}$  for all channels of the ECE imaging system for the two cases shown in figure 4.10. The channels are mapped onto the warm resonances, and they align with the profile of the electron temperature deduced from IDA inside the confined region. The channels with the cold resonances outside the separatrix obey a relativistic frequency downshift, and their warm resonances (gray crosses in figure 4.11(a)) shift towards the higher magnetic fields. The optical depth for the two cases is shown in figure 4.11(b). The effect of the modified density is reflected in the optical depth in the form of a displaced profile (blue profile in figure 4.11(b)). The background profile is shown in gray. In case 1 the channel position is at  $\rho_{\text{pol},1} = 0.978$ . It corresponds to the major radius

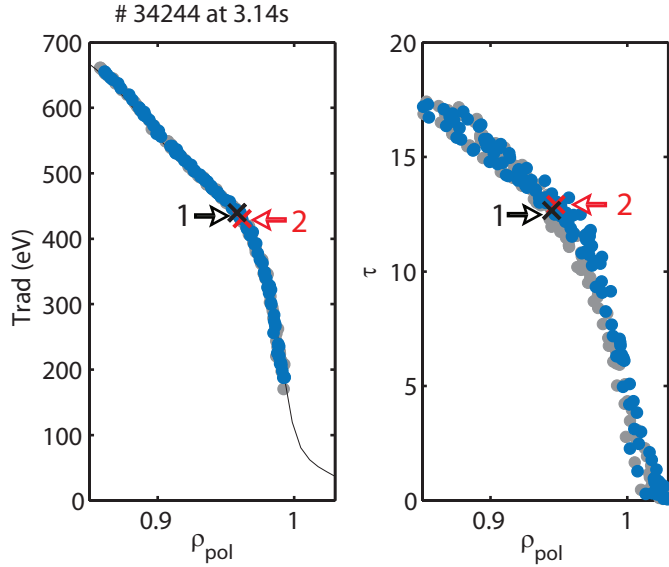


Figure 4.11: a) Modeled  $T_{\text{rad}}$  profile of the EC imaging system shown against warm resonances. The dark gray circles correspond to a case without density perturbation with input density profile shown as a solid black line in figure 4.10. The blue circles correspond to a case where the perturbed density profile, shown as a dashed black line in figure 4.10, was used. The channel analyzed in this manuscript is labeled as 1 for the case without perturbation, and 2 with perturbation present. b) Optical depth for ECEI channels for case 1 and 2, marked as gray and blue circles, respectively.

position of  $R_{\text{warm},1} = 2.138$  m. In case 2, the same channel has its warm resonance at  $\rho_{\text{pol},2} = 0.981$  with  $R_{\text{warm},2} = 2.14$  m. The  $T_{\text{rad},1} = 347$  eV in case 1, and  $T_{\text{rad},2} = 323$  eV in case 2. For  $\Delta R_{\text{warm}}$  of 2 mm the  $\Delta T_{\text{rad}}$  is about 20 eV. This makes 3% change in the  $T_{\text{rad}}$  and is comparable to the sensitivity level of the present ECE imaging system. The shift of 2 mm is within the radial resolution of the ECE imaging diagnostic. The FWHM for this channel is 11.4 mm. The result of the modeling for the profile ECE system is shown in figure 4.12. Here, in case 1 the position of the channel is  $\rho_{\text{pol},1} = 0.977$ . In major radius it is  $R_{\text{warm},1} = 2.135$  m. The warm resonance of the same channel for case 2 is  $\rho_{\text{pol},2} = 0.980$  and  $R_{\text{warm},2} = 2.137$  m. The  $T_{\text{rad},1} = 350$  eV, and  $T_{\text{rad},2} = 315$  eV. The  $\Delta R_{\text{warm}}$  is 2 mm, and is the same as for the ECE imaging system. However,  $\Delta T_{\text{rad}}$  is about 34 eV and is higher than that

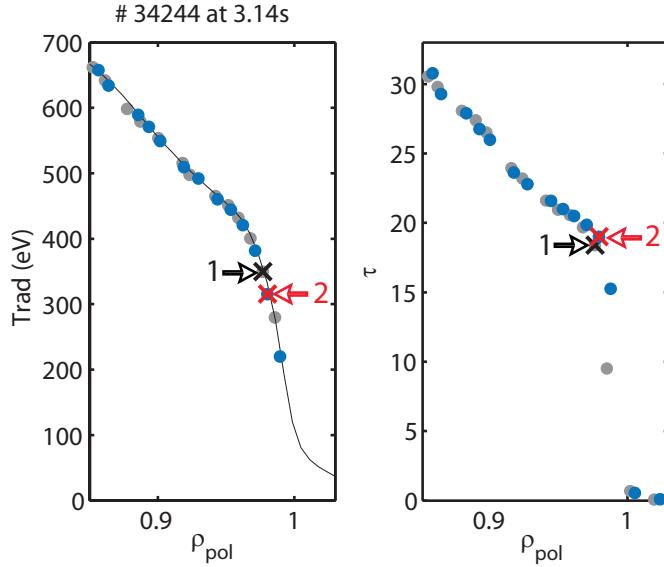


Figure 4.12: a) Modeled  $T_{\text{rad}}$  profile of the ECE system shown against warm resonances of respective channels. The dark gray circles correspond to a case with background density profile (displayed as black solid line in figure 4.10), and the blue circles correspond to a case with added Gaussian (dashed black profile in figure 4.10). The channel analysed in this manuscript is labeled as 1 for the case without perturbation, and 2 with perturbation present. b) Optical depth for ECE channels for case 1 and 2, marked as gray and blue circles, respectively.

of the ECE imaging channel. This makes about 5 % of  $T_e$  at the channel position. The radial resolution of this ECE channel is  $\sim 6$  mm thus, the radial shift of 2 mm is about half of the radial resolution of the diagnostic. Therefore, in both diagnostics, such a variation of the density profile (no  $T_e$  fluctuation in the modeling) leads to a modulation of the measured  $T_{\text{rad}}$  visible in a single channel, even though the plasma is optically thick. Increase in  $n_e$  leads to a decrease of  $T_e$ , hence if  $n_e$  and  $T_e$  are modulated in phase, then the ECE underestimates the measured amplitude. Since the density fluctuations during the inter-ELM modes are nearly almost always present, it is necessary to perform the measurements of the density fluctuations simultaneously. As shown, the effect on the channels that should be sensitive to  $T_e$  only (the optical

depth is high) is non-negligible and falls within the sensitivity of both ECE imaging and ECE diagnostics.

## 4.6 Summary and discussion

The radiation transport model makes it possible to model the response of the ECE imaging and ECE systems to different plasma scenarios in the ASDEX Upgrade tokamak. Of special interest are H-mode plasmas with pronounced density modulation at the plasma edge region during the inter-ELM periods. Such a scenario has been modelled, and the effect of the density at the pedestal top results in that both ECE imaging and ECE channels are shifted towards lower magnetic fields and lower radiation temperatures. The effective change in the radiation temperature seen by one channel due to the density is within the sensitivity for both ECE imaging and ECE systems and might, therefore, be erroneously interpreted as real temperature variation. This effect can have an impact when analyzing the cross phase between  $n_e$  and  $T_e$  fluctuations [Freethy et al., 2016]. It is not possible to disentangle  $n_e$  and  $T_e$  fluctuations with ECE imaging and ECE measurements only, however, the measurement of  $n_e$  fluctuations with another diagnostic allows quantification of their contribution to  $T_{\text{rad}}$  via the radiation transport model.



## Chapter 5

# Effects of density gradients and fluctuations at the plasma edge on ECE imaging measurements at ASDEX Upgrade\*

### Abstract

Electron Cyclotron Emission Imaging (ECE imaging) provides measurements of electron temperature ( $T_e$ ) and its fluctuations ( $\delta T_e$ ). However, when measuring at the plasma edge, in the steep gradient region, radiation transport effects must be taken into account. It is shown that due to these effects, the Scrape-Off Layer (SOL) region is not accessible to the ECE imaging measurements in steady state conditions and that the signal is dominated by the shine-through emission. Transient effects, such as filaments, can change the radiation transport locally, but cannot be distinguished from the shine-through. Local density measurements are essential for the correct interpretation of the electron cyclotron emission since the density fluctuations influence

---

\*The work presented in this chapter is published in *Plasma Physics and Controlled Fusion* in slightly modified form under the title 'Effects of density gradients and fluctuations at the plasma edge on ECE imaging measurements at ASDEX Upgrade'. B Vanovac et al. 2018 Plasma Phys. Control. Fusion 60 045002

the temperature measurements at the plasma edge. As an example, a low-frequency 8kHz mode, which causes 10 % to 15 % fluctuations in the signal level of the ECE imaging, is analyzed. The same mode has been measured with the Lithium Beam Emission Spectroscopy (Li-BES) density diagnostic and is very well correlated in time with high-frequency magnetic fluctuations. With radiation transport modeling of the electron cyclotron radiation in the ECE imaging geometry, it is shown that the density contributes significantly to the radiation temperature ( $T_{\text{rad}}$ ) and the experimental observations have shown the amplitude modulation in both density and temperature measurements. The poloidal velocity of the low-frequency mode measured by the ECE imaging is  $3 \text{ km s}^{-1}$ . The calculated velocity of the high-frequency mode measured with the magnetic pick-up coils is about  $25 \text{ km s}^{-1}$ . Velocities are compared with the  $E \times B$  background flow velocity and possible explanations for the origin of the low-frequency mode are discussed.

## 5.1 Introduction

H-mode plasmas [Wagner et al., 1982] are the foreseen scenario for the ITER operation [Martin et al., 2008]. This type of scenario is characterized by steep gradients and a pedestal build-up at the edge of the plasma. Edge Localized Modes (ELMs) [Zohm, 1996, Leonard, 2014] lead to periodic relaxations of the gradients including sudden losses of heat and particles into the unconfined region in  $\sim 1\text{-}2 \text{ ms}$  timescale. These periodic bursts can cause excessive heat loads on divertor target plates and the erosion of plasma facing components. In order to maintain the high confinement of heat and particles, but with no impurity accumulation and without large uncontrollable ELMs, ELMs need to be mitigated. For such a full control the dynamics of ELMs and associated phenomena should be better understood.

The Electron Cyclotron Emission Imaging (ECE imaging) diagnostic, with multiple lines of sight (LOS), where each LOS behaves like a conventional 1D radiometer, measures the radiation temperature and its fluctuations on  $\mu\text{s}$  timescales and is especially suitable for 2D or quasi-3D visualization of MHD phenomena. It can thus help to provide more insight into the behavior of the relative temperature fluctuations associated with the ELM cycle. To date, ECE imaging has been installed on many tokamaks including: ASDEX Upgrade [Classen et al., 2010], KSTAR [Yun et al., 2014],

EAST [Yu et al., 2012], DIII-D [Tobias et al., 2010] and HL-2A [Jiang et al., 2013]. In the case of optically thick plasmas, where the optical thickness is proportional to the product of electron density and temperature, the intensity of the cyclotron radiation equals the level of black body emission. In this case, under the condition that the electrons are in local thermodynamic equilibrium, the radiation temperature is equal to the electron temperature. However, when measuring at the plasma edge, where the density and temperatures are relatively low, the electron cyclotron emission no longer equals the blackbody radiation, and the density contribution cannot be neglected. In this case, the radiation transport equation is solved in order to obtain the radiation temperatures. It is important to note here that the geometry under which the light is collected plays a significant role. Under perpendicular observation of the plasma, where the line of sight is perpendicular to the magnetic field line, there is no significant parallel contribution of the cyclotron emission, and the Doppler broadening can be neglected. In this case, the radial resolution of the system is set by the band-pass filtering of the intermediate frequency (IF) signal around the central frequency in the second down-conversion process (the IF bandwidth). If, however, the observation angle is slightly oblique, as is the case with the present ECE imaging system on ASDEX Upgrade, the Doppler broadening must be taken into account. In this case, the radial resolution of the system is set by both IF broadening and Doppler broadening. Another critical point is related to hot H-mode plasmas where the relativistically down-shifted emission contributes significantly to the low field side emission. This effect shifts the peak of the resonance towards the higher magnetic field [Tobias et al., 2012]. When all the mentioned effects are taken into account, measurement positions in the case of oblique diagnostics can significantly differ from the cold resonance locations as shown in [Denk, S. S. et al., 2017]. In this work, we examine a particular H-mode discharge during the phase between two subsequent ELM crashes, where a large amplitude density fluctuations alongside the temperature fluctuations are measured. The main question to answer in this work is if and how much of the fluctuating signal measured with ECE imaging, which is considered a temperature diagnostic, is affected by the variation of the density at the plasma edge.

The paper is organized as follows. The ECE imaging diagnostic is described in more detail in section 5.2. Section 5.3 explains the forward model that is now rou-



tinely used for ECE Imaging at ASDEX Upgrade. Measurements of the temperature fluctuations and the mode analysis by ECE imaging is presented in section 5.4. Section 5.5 treats the spatial localization of the mode. Forward modeling of the electron cyclotron radiation with density fluctuations in the steep gradient region is described in section 5.6. In section 5.7 we compare measured mode velocities with the  $E \times B$  velocity. A summary is given in section 5.8.

## 5.2 ECE imaging at ASDEX Upgrade

The ECE imaging diagnostic at ASDEX Upgrade [Classen et al., 2014] is well suited for measurements of relative temperature fluctuations with two separate arrays looking at two toroidally separated locations inside the plasma under slightly different toroidal angles. Its poloidal extension covers the regions above, across, and below the midplane. The geometry of the ECE imaging system, configured for ASDEX Upgrade shot # 33616, is shown in figure 5.1. Figure 5.1(a) shows the  $q = 6$  flux surface in toroidal geometry as the grey transparent surface. The  $q = 6$  magnetic field line is shown as a solid white line on top of the  $q = 6$  flux surface. The two red regions are showing the two ECE imaging observation volumes and their toroidal location. The toroidal separation of the two ECE imaging systems is about  $\Delta\phi \sim 10^\circ$ . The position of the ECE imaging arrays relative to the 1D ECE radiometer is shown in figure 5.1(b) in Cartesian coordinates. The toroidal separation of  $10^\circ$  from figure 5.1(a) translates into 40 cm in Cartesian coordinates. The black circle ( $\bullet$ ) corresponds to the location of the ECE imaging channel used for the comparison with the magnetic measurements. Figure 5.1(c) shows the poloidal cross section of ASDEX Upgrade indicating the measurement positions for the different edge diagnostics used in this work: ECE Imaging, Li Beam Emission Diagnostic (Li-BES) [Willensdorfer et al., 2014], channels of the 1D ECE radiometer [Suttrop and Peeters, 1996] and magnetic pick-up coils (note that the  $R$  is defined as  $R = \sqrt{x^2 + y^2}$ ). ECE and ECE imaging are temperature diagnostics, and the Li-BES is an edge density profile diagnostic, and the magnetic pick-up coil measures magnetic fluctuations. The ECE imaging, ECE and Li-BES diagnostics are positioned in the same sector of ASDEX Upgrade, measuring at very close toroidal locations. The ECE imaging system has a toroidal observation angle. When focused at the edge, array 1 has a launching toroidal angle of 7 degrees,

and array 2 has an angle of 5.7 degrees with respect to the 1D ECE. As a consequence of the toroidal observation angle, the Doppler broadening of the emission lines is increased and therefore contributes to the radial resolution of the diagnostic. In this work, we use the data from array 2 with IF bandwidth of 390 MHz. The emission

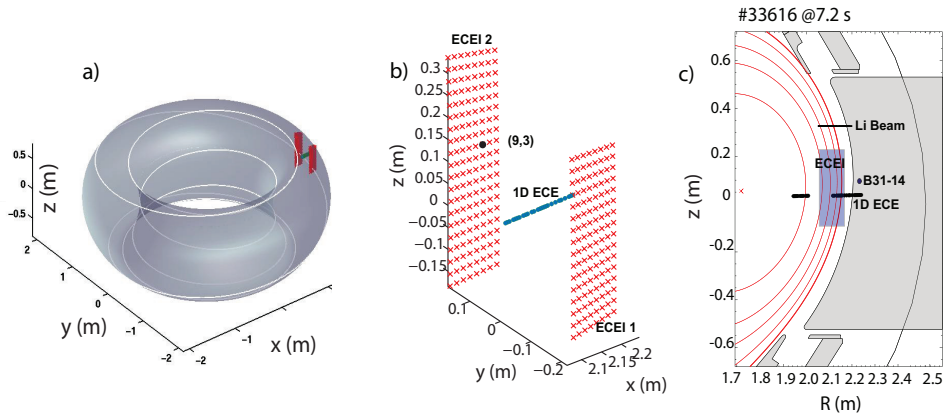


Figure 5.1: a)  $q = 6$  flux surface plotted as a gray shaded area for shot # 33616 at  $t=7.2$  s. Magnetic field line for this equilibrium is plotted as the solid white line. The red surfaces, intersecting the  $q = 6$  flux tube correspond to two ECE imaging systems. b) Absolute measurement positions of two toroidally separated ECE imaging arrays in Cartesian coordinates are shown as red crosses (X); edge channels of conventional ECE radiometer are shown as green dots. The ECE imaging channel of the ECE imaging 2 array that is used for comparison with the magnetic measurements is marked as a black circle (●). c) Poloidal cross section of ASDEX Upgrade indicating the measurement positions of the Lithium beam diagnostic, ECE Imaging, standard ECE radiometer and magnetic pick-up coil (B31-14).

of optically thick Maxwellian plasmas, when observed perpendicularly to the magnetic field, originates from a radially thin layer as is the case in the standard ECE diagnostic on ASDEX Upgrade. Therefore, for perpendicular propagation, the radial resolution of the system can be well approximated by the IF bandwidth of the system. ECE Imaging has a contribution of Doppler-broadened emission on top of the IF broadening. When observing high-density H-mode plasmas under an oblique angle,

the LOS can be approximated by a straight line for lower density cases, or a curved one due to the high-density gradient. Refraction of the beams causes ambiguity in the measurement positions. This is of particular importance for the channels at the top and the bottom of the ECE imaging arrays since they encounter the strong gradients under the largest angle. Also, due to the high temperature of the plasmas, relativistic effects cannot be neglected. Because of the relativistic mass increase of the resonant electrons, their frequency will be downshifted. When combined with the low optical depth at the plasma edge, these effects make the interpretation and the origin of the electron cyclotron radiation complicated and an extended Electron Cyclotron Forward Model (ECFM), including the radiation transport effects, needs to be used as a standard tool for determining the origin of the emitted radiation [Denk, S. S. et al., 2017].

### **5.3 Forward modeling of the radiation detected by the ECE imaging**

In order to get an idea of the diagnostic constraints and characteristics, we describe the forward modeling of the electron cyclotron radiation for an H-mode discharge where we calculate the expected radiation temperatures for a given equilibrium and electron density and temperature profiles. It is important to note that the IF bandwidth is included in this modeling, the beam is approximated with a single ray and possible influence of O-mode emission is neglected.

For a given  $T_e$  and  $n_e$  profiles, ray tracing, that accounts for refraction effects, is performed for each channel and then the radiation transport equation is solved along the line of sight until it reaches back to the antenna. The input electron density and temperature profiles are shown in figure 5.2(a). Ray tracing, with an example of 111.6 GHz channels for all 20 lines of sight, is shown in figure 5.2(b) alongside the CLISTE equilibrium reconstruction [Carthy, 2012]. The separatrix position is shown as a thick solid black line, while rays are shown as red dashed lines.

The characteristics of the emitted radiation as calculated by the ECFM of a single ECE imaging (111.6 kHz) channel at the midplane are given in figure 5.3. We distinguish two positions describing a single channel. The cold resonance position

is only dependent on the magnetic field. It is shown as a black dashed line. When radiation transport effects are taken into account, the emission position changes thus corresponding to a warm resonance position. The warm resonance is given by the peak of the birth-place distribution function  $D_\omega$ , depicted as a solid blue line. The red dashed line corresponds to the peak of  $D_\omega$  for this channel. Its resolution is determined by the width of  $D_\omega$  which corresponds to the radial extent of the plasma contributing to the emitted radiation.

The radiation transport equation is solved for every channel of one ECE imaging

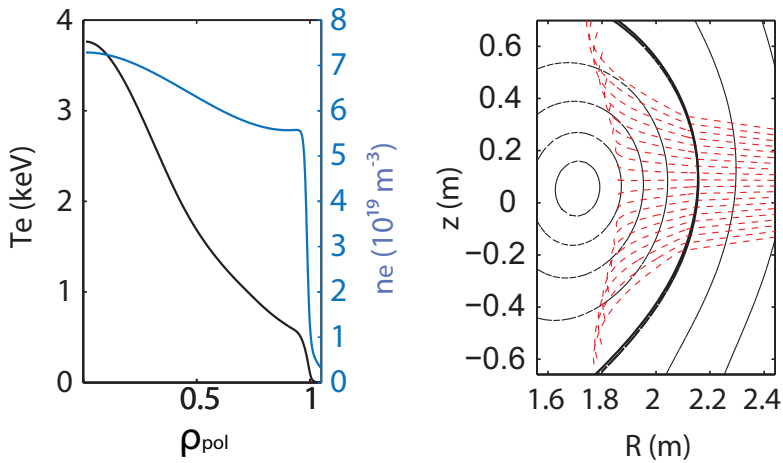


Figure 5.2: a)  $T_e$  and  $n_e$  profiles used to forward model the radiation transport. b) Ray tracing representing the lines of sight for 20 ECE imaging poloidally distributed channels.

array. The two-dimensional distribution of the cold and the warm resonances is shown in figure 5.4(a). It is observed that the innermost channels are Doppler shifted towards a larger major radius  $R$ . Therefore lower toroidal magnetic field, while the outer most channels (with the cold resonances outside the separatrix) are measuring the signal from the region inside the separatrix. This emission corresponds to the relativistically down shifted radiation. The expected radiation temperatures for ECE imaging channels mapped onto cold and warm resonance positions are shown in figure 5.4(b) and 5.4(c), respectively. It is observed that the measured surface area of the ECE imaging window, when mapped on the warm resonances, is smaller than

when mapped onto cold resonances, due to the shifts mentioned above. In the SOL region, only shine-through emission from the pedestal region can be observed in steady-state conditions.

The above analysis shows the effect of steady-state plasma conditions on the ECE

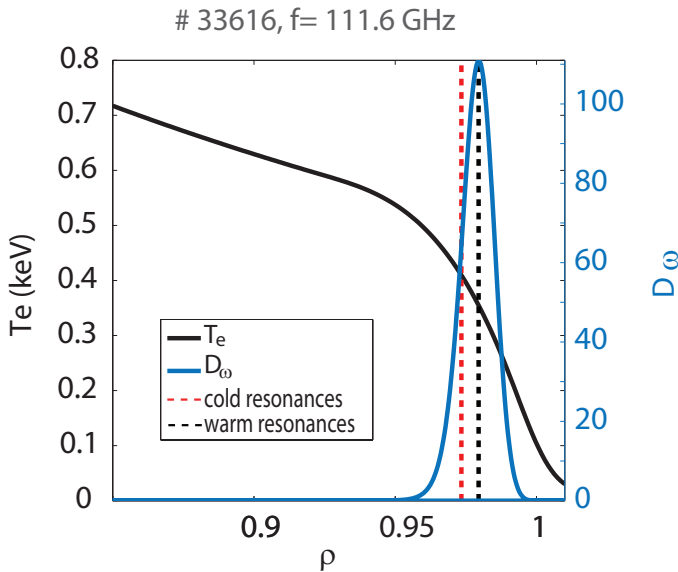


Figure 5.3: Origin of the observed emission (warm resonance) defined by the emitted intensity  $D_\omega$  for the 111.6 GHz ECE imaging channel, at the midplane. The corresponding input  $T_e$  profile is shown as a solid black line. The warm resonance position is shown as black dashed line and corresponds to a peak of  $D_\omega$ . The cold resonance is labeled as red dashed line and depends only on the magnetic field strength. The radial width of the plasma contributing to the measured signal is determined by the width (FWHM) of  $D_\omega$ .

imaging measurements. From this, one can conclude that measurements in the SOL region are not feasible with the ECE imaging diagnostics during steady state, and all the signal measured by channels in the SOL originate from the pedestal top. However, the presence of transient events, such as filaments, affects the location of the emitted radiation locally, as shown in figure 5.5. In order to examine the effect of filaments, we use the electron temperature and density distributions, instead of profiles. As the most realistic scenario we chose the distributions from a non-linear JOREK simulation [Huysmans and Czarny, 2007] during an ELM crash. It is

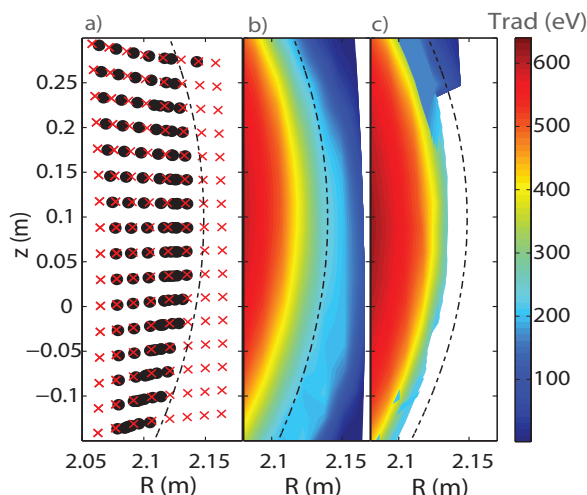


Figure 5.4: Shot # 33616 at 7.5 s. a) Calculated cold resonances are labeled as red crosses (X) and the warm resonances as black circles ( $\bullet$ ). The radiation temperature mapped onto positions of the cold resonances (b) and the warm resonances (c). The separatrix position is marked by the black dashed line.

a simulation with two fluid effects as described in [Orain et al., 2013], with a single temperature assuming that  $T = T_e = T_i$ . However, the JOREK distributions are scaled down uniformly by about 20% in order to match with the core electron density and the temperature values at the midplane of shot # 33195 at time  $t = 2.5872$  s. In this 'hybrid' simulation the steady-state equilibrium for shot # 33195 together with the electron density and the temperature distributions are used as an input for the forward model. As shown in figure 5.5(a) a  $n_e$  perturbation is abruptly crossing the separatrix, whilst  $T_e$  shown in figure 5.5(b) is smooth due to fast parallel heat losses on open field lines. Modelled cold and warm resonances for these input distributions are shown in figure 5.5(c) and 5.5(d), respectively. In figure 5.5(c) cold and warm resonances are plotted over the input electron density distribution. As seen, the positions of the outermost measurements match with the positions of the filaments. These outermost warm resonances of the LOSs at the midplane are in the SOL region. This shows that the presence of a perturbation influences the measurement position locally, shifting them towards the cold resonances. In figure 5.5(d), resonant positions are shown together with calculated radiation temperatures. Shine-Through radiation

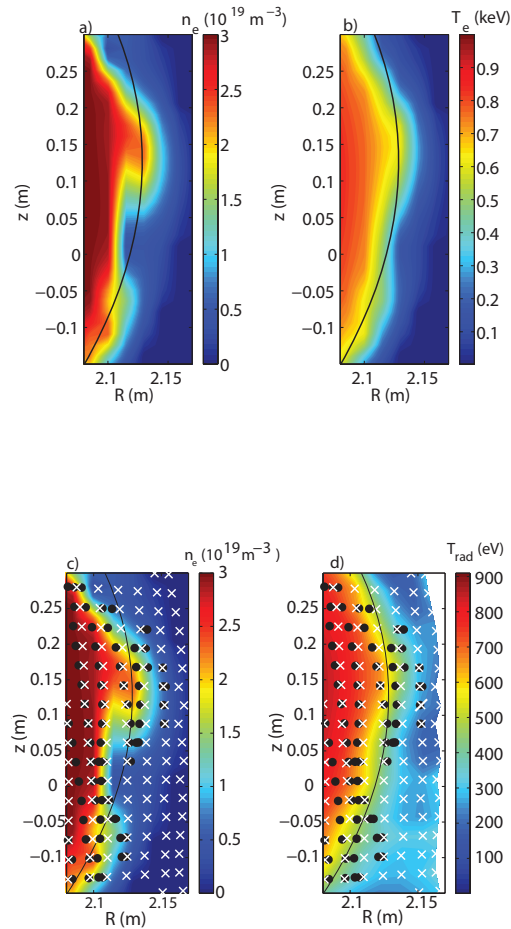


Figure 5.5: 2D JOREK profiles of: a) electron density; b) electron temperature. These profiles are matched to the values of the density and the temperature for shot # 33195 at time  $t = 2.5872$  s and used as an input for electron cyclotron forward model (ECFM). c) Warm resonance positions as calculated with the ECFM are marked as black circles ( $\bullet$ ) and the cold resonances labeled as white crosses ( $\times$ ) are mapped onto two-dimensional distribution of the input density profile that is color-coded. d) Warm resonance positions as calculated with the ECFM ( $\bullet$ ) and the cold resonances ( $\times$ ) are mapped onto a radiation temperature obtained with the forward model for the input electron density and temperature profiles shown in a) and b), respectively.

of about 300 eV is observed in the SOL region. This shine-through originates from the filamentary structures crossing the separatrix. Although, as shown, it is possible to probe the SOL in non-steady state conditions, both  $T_e$  and a shine-through is expected in this region. Thus, it is impossible to correctly interpret the measured signal without the knowledge of the local density fluctuations.

## 5.4 Observations of the modes between ELM crashes

Less violent transient events related to an ELM are inter-ELM modes. They play a crucial role in understanding an ELM cycle and may also be responsible for transport across the pedestal. So far, extensive research on this topic has been reported characterizing the dynamics of the temperature fluctuations during the inter-ELM period [Classen et al., 2013, Boom et al., 2011] with ECE imaging.

The magnetic signature also reveals high-frequency fluctuations with well-defined mode numbers. They are located in the steep gradient region [Mink et al., 2016] corresponding to the location of the minimum of the edge radial electric field [Laggner et al., 2016]. Evidence of a quasi-coherent mode during an inter-ELM period has been reported in [Diallo et al., 2015].

In order to obtain an ECE imaging signal capturing ELM and inter-ELM associated phenomena, measurements are conducted during H-mode plasmas, where steep density and temperature profiles are formed (pedestal). However, to obtain reliable measurements, the cut-off density limit is avoided by focusing on moderate pedestal top density discharges. At the same time the auxiliary heating power is adjusted to obtain ELM frequencies below 100 Hz, so that the inter-ELM dynamics of the temperature fluctuations can be measured.

From the analysis of the previous section, using the typical H-mode profiles shown in figure 5.2(a), we conclude that the radiation temperature equals the electron temperature  $T_r = T_e$  and the ECE imaging system delivers the information on the electron temperature  $T_e$  and its fluctuations inside the separatrix. In this work we will use the relative change of the electron temperature  $\delta T_e / \langle T_e \rangle$  with respect to its mean value. Here,  $\delta T_e$  is defined as  $T_e - \langle T_e \rangle$ , and  $\langle T_e \rangle$  is the time average. An example of the temporal evolution of  $\delta T_r / \langle T_r \rangle$  together with the divertor current as ELM indicator in a time period of 60 ms of discharge # 33616 is given in figure 5.6(a) and 5.6(b).



Spectrograms of the ECE imaging signal and the signal measured with the magnetic pick-up coil B31-14, are shown in 5.6 (c) and 6.4(d), respectively. The discharge was performed at a plasma current  $I_p = 800$  kA, toroidal magnetic field  $B_t = -2.52$  T (negative sign means opposite to  $I_p$ ), core density  $n_e = 7 \times 10^{19} \text{ m}^{-3}$  and with upper triangularity  $\delta_u = 0.128$  and the pedestal top collisionality  $\nu_{ped}^* \approx 1.05$ .

Figure 5.6(a) shows the temporal evolution of the divertor shunt current that

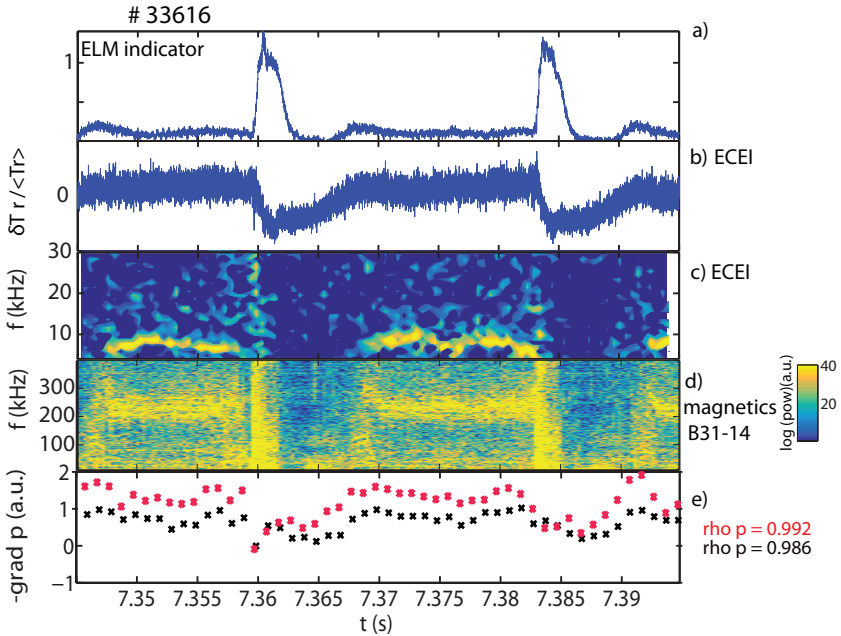


Figure 5.6: Shot #33616. Temporal evolution of the: a) Divertor current. b) Relative change of the radiation temperature ( $\delta T_r / \langle T_r \rangle$ ) measured by a single ECE imaging channel in the steep gradient region. Power spectral density comparison between: c) ECE imaging channel; d) magnetic pick-up coil; e) pressure gradient at two nearby radial locations in the steep gradient region. The position of both ECE imaging channel and the magnetic coil are indicated in figure 5.1.

consists of combined contributions of thermoelectric and Pfirsch-Schlüter currents [Kallenbach et al., 2001]. The bursts in the divertor current are correlated with the drop in  $\delta T_r / \langle T_r \rangle$  measured with the ECE imaging channel, shown in 5.6(b). Recovery of the temperature fluctuations after an ELM crash happens in two steps: a fast increase followed by a steady state phase. At the onset of the steady phase, a low

frequency ( $\sim 8$  kHz) narrow band mode sets in, see figure 5.6(c). The duration of the mode is about 10 ms and vanishes just at the onset of an ELM crash. This low frequency mode correlates well in time with the high frequency modes appearing in the magnetic measurements shown in figure 5.6(d). Both low and high frequency modes occur after the recovery of the maximum pressure gradient as shown in figure 5.6(e). In figure 5.6(e) the temporal evolution of the pressure gradient is shown at two nearby locations in the region of steepest gradients. Correlation of the clamping of the pressure gradient and the onset of the high frequency magnetic fluctuations has been studied in [Laggner et al., 2016]. The toroidal mode numbers of the high  $f$  modes, determined from the magnetics are -8, -9, -10 showing that there are multiple modes present in this frequency region. The negative sign corresponds to the rotation of the mode in the electron diamagnetic direction.

A closer look at the inter-ELM mode is presented in figure 5.7. The measurement positions of the edge ECE imaging channels are shown in figure 5.7(a). All channels distributed along the flux surface, marked as red crosses see the  $\sim 8$  kHz mode that modulates the relative temperature level up to 10 % - 15 %. The temporal evolution of  $\delta T_r / \langle T_r \rangle$  measured by the single ECE imaging channel at the vertical position  $z = 0.1$  m, corresponding to the magnetic midplane, is shown in figure 5.7(b). A spectrogram of the midplane measurement, presented in figure 5.7(c), shows the strong mode in the  $\sim 8$  kHz range. The observed mode slightly changes in frequency during its lifetime. The duration of the mode is  $\sim 10$  ms and  $\delta T_r / \langle T_r \rangle$  during its lifetime is about 10 %. Poloidally resolved measurements  $\delta T_r / \langle T_r \rangle$  expressed in percentage along the flux surface are shown in figure 5.7(d) in a form of vertically distributed time traces. This kind of visualization helps to follow the propagation direction of the mode. From here it can be seen that the mode propagates from the bottom to the top, corresponding to the electron diamagnetic direction.

Such poloidally resolved measurements enable the determination of the poloidal velocity of the observed mode. Figure 5.8(a) is a zoom into the phase of the constant frequency of the mode. Three channels at the midplane ( $z=0$ ) are set to zero. The quality of data for those channels was too poor due to electronics. Therefore they are omitted for better graphical representation. In order to determine the velocity of the mode in the vertical plane, we use the cross-correlation between a reference channel and all the other poloidally distributed channels along the flux surface as

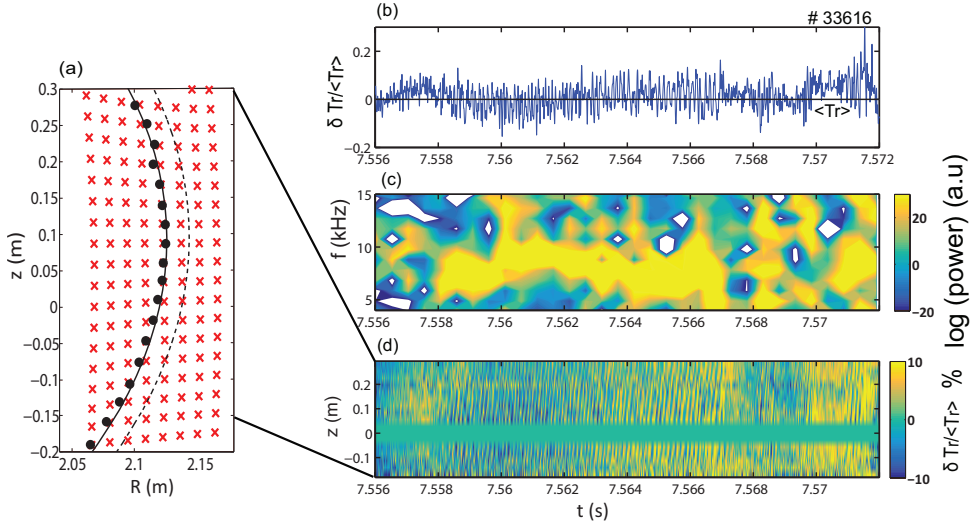


Figure 5.7: Localization and the temporal evolution of  $\delta T_r / \langle T_r \rangle$  seen in the ECE imaging observation window. a) Warm resonant channels ( $\bullet$ ) of array 2, that measure the modulation of the radiation temperature, are distributed along the flux surface at  $\rho_{\text{pol}} \sim 0.985$ . b) Relative temperature change of a single channel 10 cm above the midplane. c) Time resolved spectrogram of the channel as in (b) showing the presence of the strong mode in the 7 - 8 kHz range. d) Temporal evolution of  $\delta T_r / \langle T_r \rangle$  in percentage measured by the channels distributed along the flux surface with positions shown in (a) as black bullets. This representation visualize the propagation of  $\delta T_r / \langle T_r \rangle$  in the poloidal direction, from the bottom to the top channels, along the flux surface. Three channels at the midplane ( $z=0$ ) are set to zero due to the poor data quality.

shown in figure 5.8(b). The velocity measured this way, shows no variations along a flux surface, and follows the straight line as indicated by the black arrow. The calculated velocity of the mode is  $\sim 3 \text{ km s}^{-1}$  moving in the electron diamagnetic direction. Cross-correlation between three vertical positions indicates the structure with three maxima fitting in the ECE imaging observation window. The local poloidal wavelength of this mode, as measured on the low field side, therefore is  $\lambda_{\text{pol}} \sim 15 \text{ cm}$ .

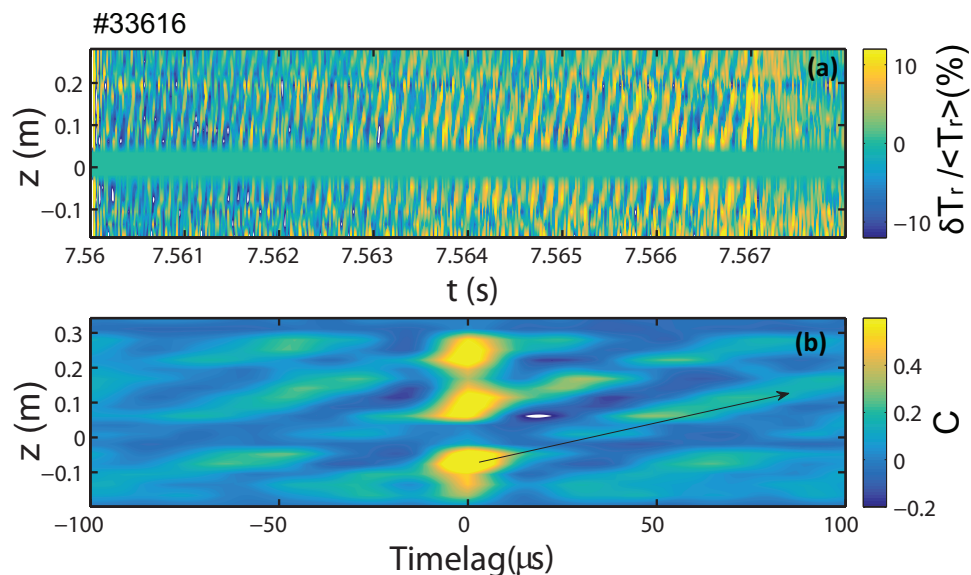


Figure 5.8: a) Vertically resolved  $\delta T_r / \langle T_r \rangle$  along the flux surface during the 8 kHz mode duration. b) Cross-correlation of the reference channel taken at the vertical position  $z = -0.1$  m with all other poloidal channels. The black arrow approximates the direction of the mode propagation in space and time.

## 5.5 Spatial localization

To complement the analysis of the modes observed with ECE imaging, data is compared with other edge diagnostics shown in figure 5.1(a). The Li-BES diagnostic that resolves the profiles of the electron density and its fluctuations at the plasma edge also observed the mode activity. It is also measured by the conventional 1D ECE radiometer. Comparison between conventional ECE, ECE Imaging and Li-BES measurements at the edge is shown in figure 5.9 in the form of spectrograms. All spectrograms show activity in the  $\sim 8$  kHz range indicating the mode is present in both density and temperature measurements.

The amplitude of the density fluctuations is estimated from the Li-BES forward model [Willensdorfer et al., 2014] in the following fashion: In order to obtain information on the relative change  $\delta n/n$  of the electron density, this quantity is varied in order to match measured fluctuations in the collected light  $\delta I/I$  of 10%. The deviation is assumed to be Gaussian in space, of the width that matches the radial

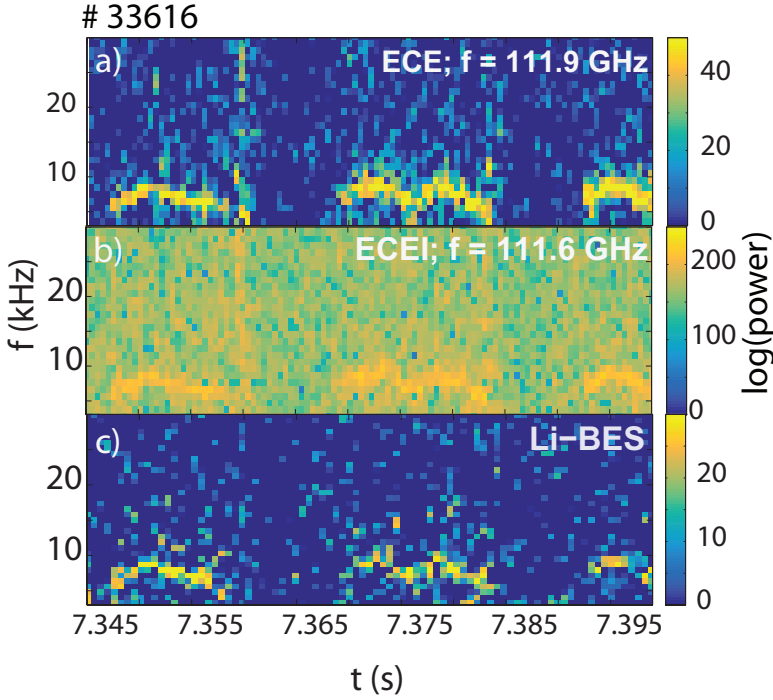


Figure 5.9: Power spectral density showing a narrow band mode; a) in the ECE channel, b) ECE imaging, c) Li beam channel.

resolution of the Li-BES system (5 mm). The location of the perturbation (center of the Gaussian) matches the channel where the mode is detected. The variation in the density is calculated to be between 20% - 40%. The background electron density at the position of the mode is between  $(4 - 5) \times 10^{19} \text{ m}^{-3}$ . The Li-BES and 1D ECE radial resolution of 5 mm allows for more accurate localization of the mode than the one from the ECE imaging. The 1D ECE channel at the same location as the Li-BES channel measures the mode activity. Therefore the position of the measurement corresponds to the position of its respective channels at  $\rho_{pol} = 0.983$ . At the separatrix position at  $\rho_{pol} = 1$ , the mode is not observed, while at the location  $\rho_{pol} = 0.97$  and inwards, ECE and ECE imaging do not observe the mode. The Li-BES diagnostic is not sensitive in this region.

This information is further used in the forward model of the electron cyclotron emission in order to qualitatively investigate the influence of the density on the

signal measured by the ECE imaging in the steep gradient region where the mode is measured.

## 5.6 Forward model of the EC radiation with density fluctuations

Following the result of the analysis of the Li-BES data, the variation in the density level is taken to be between 20% and 40%. Those limits are used for the electron cyclotron forward model in order to study the radiation temperature response to the changes in the density. In order to model the response of the radiation temperature

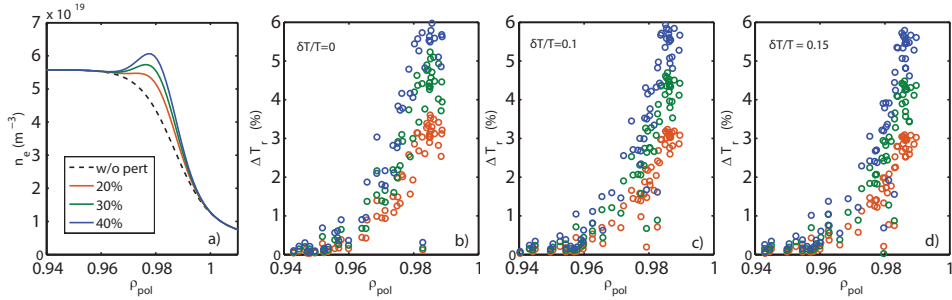


Figure 5.10: Radiation temperatures ( $\Delta T_r$ ) in percentage defined as  $\Delta T_r = \delta T_r / \langle T_r \rangle$  obtained with the ECFM for the different levels of density variations as shown in a). b) Radiation temperatures without input temperature variation. c) with the input temperature variation of 10%. d) with the input temperature variation of 15%.

to the density change, the same steps are applied as explained in Section 3. This study requires the input profiles with inserted density perturbation that mimics the one measured by the Li-BES diagnostic. The shape of the perturbation is the same as the one used in the Li-BES forward model. Modeling accounts for three different scenarios assuming that we have the cases where the temperature and the density are in phase but of different amplitudes. For this reason, the  $\delta T/T$  values of 0, 0.1, 0.15 is added on top of the background  $T_e$  profile. For each case, we varied the density profile as shown in figure 5.10. Figure 5.10 (a) shows the input density profiles used for the modelling. The density variation is between 20 - 40% and is color-coded.

Variations in the radiation temperatures cannot be distinguished between the three cases for  $\delta T_e/T_e$  of 0, 0.1, 0.15 shown in figure 5.10(a), 5.10(b), 5.10(c), respectively. The variation in the density ( $\delta n_e/n_e$ ) for each case induces a change of the radiation temperature  $\Delta T_r$ . At the location of the mode ( $\rho_{\text{pol}} = 0.983$ ), we can see that 20 % of density perturbation is captured in the radiation temperatures inducing 3 % change in the radiation temperature. The  $T_r$  increases with the amplitude of the density variation. It is important to note that in the forward model we omitted the possible O-mode contribution and that the complex ECE imaging beams are approximated with a single array. Due to those simplifications, the modeled and measured amplitudes cannot be directly compared.

## 5.7 Mode velocities and comparison to the $v_{E \times B}$ velocity

The mode velocity in the ECE imaging reference frame is  $v_{\text{mode}} = v_{E \times B} + v_{\text{ph}}$ , where  $v_{E \times B}$  is governed by the radial electric field  $E_r$ , and  $v_{\text{ph}}$  is the intrinsic phase velocity of the mode. The  $E_r$  profile for this discharge is estimated using the neoclassical approximation for the poloidal flow of impurities [Viezzer et al., 2013], using experimental profiles of  $n_e$  and  $T_i$ . The  $n_e$  and reconstructed  $E_r$  profiles are shown in figure 5.11(a). The position of the highest perturbation in the signal, detected with different diagnostics, is within the color-coded areas and those areas represent the radial extent of the plasma contributing to this measurement. Grey corresponds to the radial resolution of the ECE imaging system and red to the Li-BES and ECE diagnostics, respectively. It can be seen that ECE imaging averages the signal over a much wider range of plasma radius. If we assume that the location of the mode is where the perturbation in the diagnostic measurements peaks, the radial resolution of the Li-BES and ECE then enable localization of the mode to a precision of 5 mm as explained in section 5.5. The background  $v_{E \times B}$  velocity is calculated as  $v_{E \times B}(r) = \frac{E(r) \times B(r)}{B(r)^2}$  and is shown in figure 5.11 (b). The evaluated  $v_{E \times B}$  at the position of the perturbation peak is about  $25 \text{ km s}^{-1}$  and matches with the minimum of the  $E_r$ . This is, however, not in agreement with the velocity obtained from the poloidally distributed ECE imaging channels, which is measured to be  $3 \text{ km s}^{-1}$ .

The high-frequency modes (see figure 5.6(d)) are observed at the same time as the low-frequency modes on the magnetic pick-up coils measuring at the low field

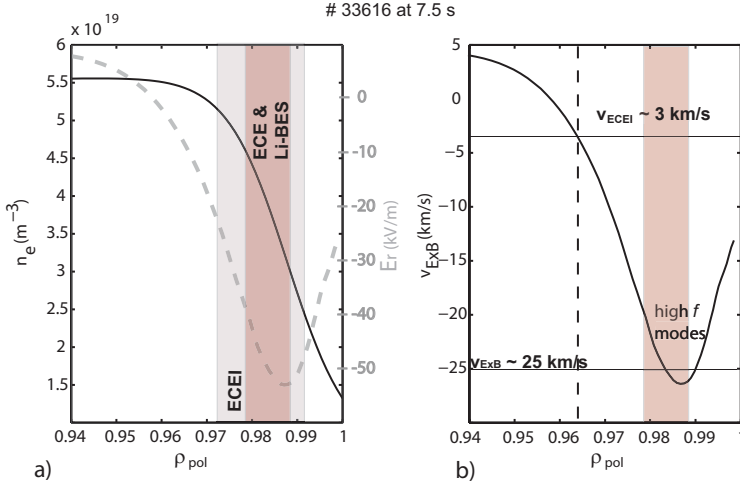


Figure 5.11: Shot #33616 at  $t = 7.5$  s. a) Density profile of the steep gradient edge region shown as a solid black line; radial electric field  $E_r$  estimated from the poloidal flow of impurities is presented as a dashed gray line. Radial resolution of the edge diagnostics used in this work is color-coded: red corresponding to the Li-BES and 1D ECE channel; grey corresponding to the ECE imaging channel. b)  $E \times B$  velocity calculated using the  $E_r$ . The vertical dashed line shows the position of the mode in case the velocity of the mode would match exactly the  $E \times B$  velocity.

side. As shown in [Laggner et al., 2016] the high-frequency modes measured by the pick-up coils are located in the minimum of  $E_r$ . From the measured frequency of the high frequency modes, if the mode is located on the rational surface  $q = \frac{m}{n}$ , one can determine its poloidal velocity as the  $v_{mode} = 2 \cdot \pi \cdot r \cdot \frac{f}{q \cdot n}$ , where  $r$  is the radial location of the mode and  $f$  its frequency. Using the following parameters of  $q = 5$ ,  $f = 240 \text{ kHz}$ ,  $n = 8$  and  $r = 0.6 \text{ m}$ , the calculated mode velocity is  $\sim 22 \text{ km s}^{-1}$  and is comparable with the  $E \times B$  velocity within the measurement uncertainties. The propagation direction of both low and high frequency modes is in the electron diamagnetic direction and their velocities differ by about a factor of 10. However, the maximum of the perturbation does not necessarily have to coincide with the position of the mode. The mode located at the pedestal top could cause the displacement in the region of the steepest gradients where the diagnostics are most sensitive. If the



mode is located at the pedestal top, the velocity of the mode will match the  $v_{E \times B}$  velocity within the measurements uncertainty. This would correspond to a  $\rho_{\text{pol}}$  of about 0.964, marked as the vertical dashed black line shown in figure 5.11(b). The background density at this position is  $5.5 \times 10^{19} \text{m}^{-3}$ . Thus the low sensitivity of the diagnostics at the pedestal top could cause the ambiguity in the measurement position. This effect will be further investigated.

## 5.8 Summary and Discussion

In summary, it is shown that SOL measurements with the ECE imaging system are not feasible in a steady state due to the shine-through emission in this region. The radiation temperature in the SOL region, which is a region of low optical depth, is down-shifted emission from the electrons in the tail of the Maxwellian originating in the pedestal region. However, the presence of ELM filaments in the SOL region can change the optical depth locally, due to the locally higher density and temperature. Therefore both, shine-through as well as the local emission can be observed simultaneously. In this case, it is difficult to distinguish between the two contributions without the local density measurements.

In the H-mode discharge examined in this work, a strong 8 kHz mode has been observed between ELMs, with different edge diagnostics. The mode is highly correlated with the high frequency ( $\sim 200$  kHz) inter-ELM modes detected on the magnetic pick-up coils since both branches set in the phase of the clamped pressure gradient before an ELM crash. Another interesting feature is that the high-frequency modes are localized at the position where the diagnostics measure a low-frequency amplitude modulation of 8 kHz. This position matches with the minimum of the radial electric field and the propagation direction of both low and high-frequency modes are in the electron diamagnetic direction, in agreement with the sign of  $E_r$ . The magnetic pick-up coils measure multiple modes with well defined toroidal mode numbers whilst the ECE imaging/ECE/Li-BES systems measure a single mode at low frequency. The low-frequency mode is also seen on the magnetic measurements, but of very low amplitude and its mode numbers remained undetermined.

The cross-correlation analysis from the ECE imaging measurements has shown the poloidal structure of the low-frequency mode with a local poloidal wavelength

$\lambda_p = 15$  cm. The poloidal mode velocity as calculated from the signals of the ECE imaging channels distributed along the flux surface is  $3 \text{ km s}^{-1}$ , rotating in the electron diamagnetic direction. With the high spatial resolution of the Li-BES and 1D ECE diagnostics, the peak of the perturbation in the signal amplitude is measured with higher accuracy than the one of the ECE imaging diagnostic. The same perturbation in between ELMs is observed in the density measurements with the Li-BES diagnostic. Since measurements of Li-BES are sensitive to changes in the density, it is concluded that  $n_e$  fluctuations contribute to the ECE imaging measurements. The forward model of the electron cyclotron emission is used with an added Gaussian perturbation in the pedestal region to mimic the density fluctuations in that region. This study has shown that the density fluctuation level can influence the measurements of ECE imaging and contribute to the measured radiation temperature  $T_r$ . Thus, knowledge about the local density values is necessary for correct interpretation of the measured signal. Taking into account the measurement facts and the ambiguities in measurements due to the diagnostics sensitivity, only hypotheses can be proposed as a possible explanation for the appearance of the low-frequency mode and those will be further investigated. One hypothesis supports the idea of non-linear interaction between two or more high-frequency modes that as a result give the low-frequency mode. This resulting mode is non linearly amplified in the low field side region where it is measured by the ECE imaging system. Experimental findings that support this theory have already been reported on different machines. Significant modification of the mode structure due to the non-linear coupling has been reported on TCV [Wenninger et al., 2013], and similar amplitude modulation has been observed in KSTAR [Kim et al., 2015] and explained by a superposition of two modes with different poloidal velocities. In the case studied in this manuscript, the result of the multiple mode interaction would be a wave with a measured group velocity of  $3 \text{ km s}^{-1}$ .

Another hypothesis is that the measured mode coexists together with the high-frequency modes, at the same position, but very weak in amplitude compared to the high-frequency modes. In this case, the  $E \times B$  velocity of  $25 \text{ km s}^{-1}$  and the measured mode velocity of  $3 \text{ km s}^{-1}$  would result in a mode with a large phase velocity  $v_{ph} = 22 \text{ km s}^{-1}$ , in the ion diamagnetic direction.

The third possibility is that the mode is located where the measured velocity of the mode matches the  $E \times B$  velocity. In this case, the position of the mode is at the

pedestal top, and the mode has no resolvable intrinsic phase velocity ( $v_{\text{ph}} = 0$ ). The mode has well-defined structure rotating in the electron diamagnetic direction in agreement with the  $E \times B$  velocity at that location. The nature of the mode could be assigned to the density fluctuation at the pedestal top that influences the steepest gradient region, where the diagnostics are most sensitive.

To distinguish between the possible explanations on the origin of the mode within the future work, the poloidal velocities of the low frequency modes with a variation of plasma parameters which are known to change the frequency of the high frequency modes, i.e. edge safety factor  $q$  and the ion pressure gradient  $\nabla p_i$ , will be examined. The dynamics of the fluctuations measured by ECE imaging with newest non-linear JOREK simulations comprising an inter-ELM period will be compared. Further investigation of the sensitivity of the measurements in the pedestal top region will be conducted. A possible effect of the low-frequency mode on transport will also be assessed in future analysis.

The ECE imaging diagnostic, with its excellent poloidal resolution, is a useful tool for characterizing fluctuations at the edge through their poloidal size and velocity. The signal, however, can be dominated by the changes in the density profile and does not necessarily reflect the amplitude of the  $T_e$  fluctuations.

## Chapter 6

# Characterization of low-frequency modes of H mode discharges at ASDEX Upgrade \*

**Abstract:** The steep edge gradient region of tokamak plasmas in the high confinement regime is known to drive instabilities, which cause transport. Several diagnostics are used to allow for a high degree of characterization of low-frequency modes appearing in between type-I Edge Localized Modes (ELMs). These modes are dominantly observed in Electron Cyclotron Emission (ECE) and ECE Imaging measurements as a modulation of radiation temperature ( $\delta T_{\text{rad}}$ ). In the radial magnetic field ( $\dot{B}_r$ ) measurements, the frequency range of 4 kHz to 12 kHz is observed. The position of the mode is determined to be at the upper part of the steep gradient region, the poloidal mode velocity is changing from  $1.5 \pm 0.5$  km/s to  $2.5 \pm 0.5$  km/s and the toroidal mode number is 13 to 14. A comparison with the measured  $E \times B$  velocity leads to the conclusion that the phase velocity of the mode is smaller than 3 km/s or zero. The poloidal structure of the modes is found to agree with the poloidal structure size associated with  $n = 13$  as estimated from equilibrium calculations. The modes are compared between two different heating phases during one discharge, and

---

\*The work presented in this chapter is published in *Nuclear Fusion* under the title 'Characterization of low-frequency modes of H-mode discharges at ASDEX Upgrade'. B. Vanovac et al 2018 Nucl. Fusion 58 112011

are found to differ in duration, velocity, frequency and toroidal mode number. The possibility of non-linear interaction between these modes and other, high-frequency modes existing in the narrow pedestal, is assessed via bicoherence analysis. The presented analysis gives an unprecedented picture of the mode, its position, its structure and its velocity, calling for comparison with non-linear modelling.

## 6.1 Introduction

The improved confinement mode of tokamak operation, referred to as H-mode [Wagner et al., 1982], is characterized by the formation of the Edge Transport Barrier (ETB) in the outermost part of the confined region. Characteristics for this region are steep gradients and the formation of a pedestal. The pedestal is, however, intermittently unstable and the ETB collapses in a quasi-periodic manner expelling heat and particles. These periodic events are called Edge Localized Modes (ELMs) [Zohm, 1996, J W Connor, 1998, Leonard, 2014]. The linear stability boundary, i.e., the onset of the ELM crash, is often described by the coupling of peeling and ballooning modes in the pedestal. The peeling modes are driven by the local edge current density and the ballooning modes by the steep pressure gradient. When the pedestal parameters reach the peeling-ballooning limit, an ELM crash occurs [Gohil et al., 1988]. However, before an ELM crash, there exists a broad spectrum of instabilities in the pedestal region, so-called inter-ELM modes [Diallo et al., 2015, Laggner et al., 2016]. These inter-ELM modes might cause transport and influence the pedestal structure. The pedestal structure determines the stability of coupled peeling-ballooning modes and therefore the achievable pedestal top pressure [Snyder et al., 2002, Wolfrum et al., 2015]. As the core plasma is determined mainly by the pedestal height, fusion gain is directly related to the pedestal pressure. The inter-ELM modes and precursors are the focus of ELM-directed research for decades. Both have been observed in different machines. MHD modes such as palm tree modes [Koslowski et al., 2005] and washboard modes [Perez et al., 2004b] have been detected at JET. ELM precursors have been observed at ASDEX Upgrade [Suttrop et al., 1996], COMPASS-D [Colton et al., 1996] and JET [Perez et al., 2004a]. At ASDEX Upgrade, simultaneous observations of high-frequency and low-frequency inter-ELM modes, related to type I ELMs, have been

reported [Bolzonella et al., 2004]. High (200-300 kHz) and mid-frequency (50-100 kHz) inter-ELM modes at ASDEX Upgrade have been characterized, and have been inferred from measurements of the toroidal and poloidal mode numbers to be resonant at  $q$ -surfaces near the minimum radial electric field ( $E_r$ ) field and at the separatrix, respectively [Laggner et al., 2016, Mink et al., 2016]. Both frequency branches were measured with magnetic pick-up coils. The ECE imaging diagnostic also measures the inter-ELM modes in the pedestal, in the low-frequency part of the spectrum at ASDEX Upgrade [Boom et al., 2011, Manz et al., 2014], and KSTAR [Kim et al., 2015]. With a careful analysis at the plasma edge, it is possible to distinguish between the different modes appearing in the narrow pedestal. To reliably employ ECE and ECE Imaging diagnostics, forward modeling of the electron cyclotron radiation is performed, to account for the effect of the density variation onto the radiation temperature at the plasma edge. This effect has been studied in ASDEX Upgrade [Vanovac et al., 2018a, Vanovac et al., 2018b], in DIII-D [Tobias et al., 2012], and in KSTAR [Ayub et al., 2017]. This manuscript focuses on characterization of the low frequency ( $\sim 10$  kHz) inter-ELM mode using edge measurements from several diagnostics at ASDEX Upgrade. The combination of spatial information, 2D structure,  $q$  profiles, the profile of  $E_r$ , poloidal velocity, and toroidal mode numbers allow characterizing inter-ELM modes in great detail. Section 6.2 describes the set-up of the experiment necessary to study inter-ELM modes. Magnetic properties are discussed in section 6.3. Methods used for the localization of the mode are described in section 6.4. Poloidal structure and poloidal velocity from the ECE imaging system are presented in section 6.5. Possibilities for mode interaction are discussed based on bicoherence analysis of the data from the magnetics in section 6.6. A summary and discussion are given in section 6.7.

## 6.2 Overview of the discharge

The ASDEX Upgrade discharge # 34244, used for the analysis in this manuscript, is taken from a set of discharges designed to study the fluctuations in between ELMs. The parameters of this discharge are shown in figure 6.1. A moderate pedestal top density  $n_e^{\text{ped}} < 5 \times 10^{19} \text{ m}^{-3}$  is chosen to avoid cut-off of the ECE and ECE imaging radiation. It is heated with a low auxiliary power to obtain a low repetition

frequency of ELMs ( $f_{\text{ELM}} \sim 50$  Hz), hence long inter-ELM periods. The constant toroidal magnetic field  $B_t = -2.5$  T and the plasma current  $I_p = 0.8$  MA are not shown. The value of  $q_{95}$  is constant throughout the discharge. The outer plasma boundary  $R_{\text{aus}}$  is varied to have a better resolution of edge diagnostics. The Neutral Beam Injection (NBI) power is increased at 6.1 s from 2.5 MW to 3.4 MW. The ECRH power of 1.2 MW is constant during the phases of interest. For the analysis of the low-frequency inter-ELM modes and the evaluation of the radial electric field, we use two-time windows. The radiated power is shown in the bottom plot and does not change significantly between the two heating phases. We mark the first window as (I), with the auxiliary heating power of 3.7 MW ( $P_{\text{NBI}} = 2.5$  MW and  $P_{\text{ECRH}} = 1.2$  MW). The second time window (II) has auxiliary heating of 4.6 MW ( $P_{\text{NBI}} = 3.4$  MW and the  $P_{\text{ECRH}} = 1.2$  MW). The repetition frequency of ELMs ( $f_{\text{ELM}}$ ) changes when going from phase one to phase two due to the difference in the input power. During phase one  $f_{\text{ELM}}$  is  $\sim 40$  Hz, and during the second phase, two frequency branches are detected, both with  $f_{\text{ELM}}$  below 100 Hz. The time windows where we show individual modes measured in the magnetics are chosen around phases in which the outer plasma boundary  $R_{\text{aus}}$  reaches its maximum value during one of its scans. Those time periods were selected because the magnetic measurements show a higher amplitude and hence a better signal due to the plasma being closer to the pick-up coils. There is no change in the signal quality of the other diagnostics when compared to the remainder of the time span in a constant heating phase. An example of different quantities characterizing the plasma edge during ELM cycles for discharge #34244 is given in figure 6.2. This time interval is chosen from the collection of time intervals where the Li-BES operated in beam 'on' phase. The depicted time interval shows three ELM crashes. As an indication of an ELM crash, a peak in the divertor current that consists of the combined contributions of thermo-electric and Pfirsch-Schlüter currents [Kallenbach et al., 2001], is used and is shown in figure 6.2(a). However, not only the divertor shunt current but all the other quantities exhibit an abrupt behaviour during an ELM crash. Figure 6.2(b) displays a Li-BES measurement [Willensdorfer et al., 2014] of the electron density at the pedestal top. A similar feature observed in the electron temperature is shown in figure 6.2(c). The  $T_e$  measurements are performed with the Electron Cyclotron Emission (ECE) diagnostic [Suttrop and Peeters, 1996]. Power spectral

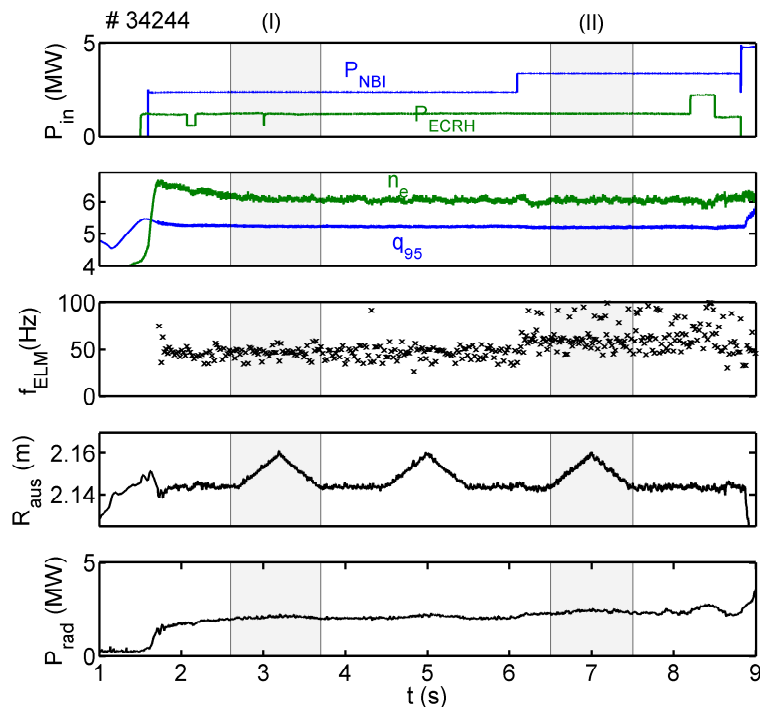


Figure 6.1: Overview of the parameters for discharge # 34244. From top to bottom: Auxiliary heating power, density and  $q_{95}$ , ELM frequency, a position of the outer plasma boundary ( $R_{\text{aus}}$ ) and radiative power. The phases used for the analysis of inter-ELM periods, and for comparison of the radial electric field are marked as (I) and (II), respectively.

densities of the magnetic and ECE signals are presented in figures 6.2(d), 6.2(e) and 6.2(f), respectively. The recovery of plasma edge parameters follows the ELM crash. Soon after the crash, the pedestal density and temperature profiles start to build up, albeit on different time scales [Burckhart et al., 2010]. The electron density recovers at a faster rate while the temperature increases gradually until the next ELM crash. From the spectrograms of magnetic and ECE data, we identify different magnetohydrodynamic (MHD) activities throughout an ELM cycle. MHD modes accompany an ELM crash [Mink et al., 2018]. While the edge  $n_e$  and  $T_e$  profiles recover, the electromagnetic signal is either quiet or shows an electromagnetic activity



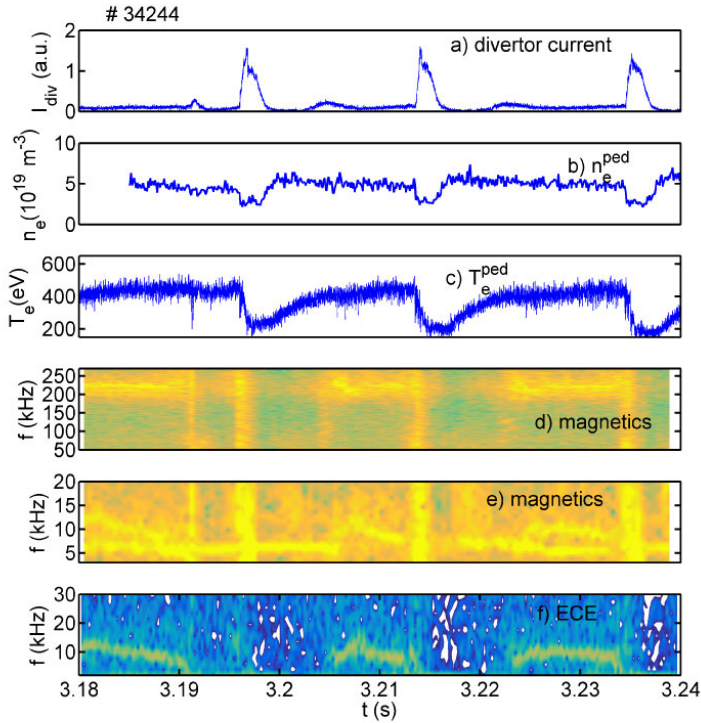


Figure 6.2: ELM cycles at ASDEX Upgrade: An example of the temporal evolution of different edge quantities during the discharge # 34244. a) Divertor shunt current as an ELM signature. b) Pedestal electron density measured with the Lithium Beam Emission Diagnostic. c) Pedestal electron temperature measured with the ECE radiometer. Spectrogram of the signal measured with a magnetic coil is displayed separately for the mid- to high- frequency range (50 kHz to 250 kHz ) as shown in d) and in the low-frequency range (4 kHz to 20 kHz) as shown in e). f) Spectrogram of an ECE edge channel.

of very low amplitude. As shown in figure 6.2(d), after the  $T_e$  recovery, the power spectral density of the magnetic signal peaks at a few frequency branches. The *high frequency branch*, studied in [Diallo et al., 2015, Laggner et al., 2016] is of the order of 200 kHz, with identified toroidal mode numbers of  $n \sim 11$  [Laggner et al., 2016]. This frequency branch is localized close to the minimum in  $E_r$ , and the modes

rotate with the velocity of the background  $E \times B$  flow at that position in the electron diamagnetic direction. The *mid-frequency branch* ( $\sim 50$  kHz to  $100$  kHz) is short-lived. It appears once the pressure gradients are established and clamped. They are characterized by low toroidal mode numbers of  $n = 4-6$  [Mink et al., 2016]. In the lowest part of the frequency spectrum a *low frequency mode*  $\sim 10$  kHz, as shown in the ECE power spectrum, is observed. This is the only MHD activity clearly visible on both ECE (figure 6.2(e)) and ECE imaging diagnostics during the inter-ELM period. The sampling rate of ECE is  $1$  MHz and the one for ECE imaging is  $500$  kHz. The observation of the low-frequency modes has previously been reported in [Vanovac et al., 2018b] and is measured as modulation in electron density, temperature and as MHD oscillations in Mirnov coils that measure the radial component of the magnetic field. In this manuscript, only data from the magnetics, ECE, and ECE imaging are analysed. The modes are, however, not always visible in the magnetic measurements and are obscured by a strongly visible core mode ( $\sim 5$  kHz in this experiment) or its first harmonic that is of a similar frequency as that of the low-frequency mode. Bandpass or low pass filtering to the ECE and ECE imaging data is applied in the analysis, and is specified when performed in the further sections. As the visibility of the low frequency mode in the magnetic spectrogram increases with the plasma being closer to the wall we make use of the scan of the outer plasma boundary to analyze the data from the magnetics, as already suggested earlier in this manuscript.

### 6.3 Magnetic properties of modes

Figure 6.3 shows measurements of the magnetic pick-up coil and the ECE diagnostic during the inter-ELM period for two isolated inter-ELMs in different heating phases, labelled as (I) and (II) as indicated in figure 6.1. The measurements are performed at the outboard midplane. No filtering to the data was applied. The top frame of figure 6.3(a) displays the high-frequency part in the magnetic measurements, while the middle one depicts the low-frequency region of the same magnetic signal. The bottom frame shows the low-frequency part of the spectrum measured by a single edge channel of the ECE diagnostic. The high-frequency branch starts as a broad mode in the frequency range of  $200 - 220$  kHz with toroidal mode number  $n = -8$  and

continues its evolution as a mode with more localized frequency at around 220 kHz with toroidal mode number of  $n = -9$ . The minus sign describes the rotation of the modes in the electron diamagnetic direction (or counter-current direction).

The low-frequency branch in the magnetic measurements displays the core mode with toroidal mode number  $n = 1$  and the edge mode with a strong indication of  $n = -13$ . The frequency of the edge mode changes. It starts at 8 kHz, subsequently increasing to 11 kHz, and then slightly decreases until it is interrupted by an ELM crash. Similar behaviour is observed during the second heating phase as shown in figure 6.3(b). The top frame shows the high-frequency branch of the magnetic signal with a single mode of frequency around 220 kHz and the toroidal mode number  $n = -9$ . The middle frame shows the core  $n = 1$  mode with a frequency of 9 kHz and the edge mode with starting frequency of 7 kHz that is decreasing to 4 kHz just before an ELM crash. The toroidal mode number associated with the low-frequency edge mode is  $n = -14$ . The low-frequency modes differ for the two heating phases. We

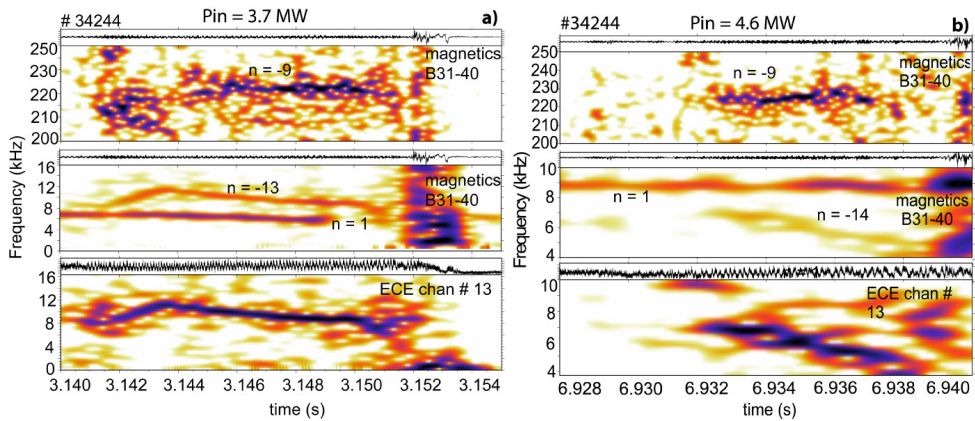


Figure 6.3: Spectrograms of magnetic (B31-40) and ECE (channel #13) measurements during an inter-ELM period for lower (a) and higher (b) heating phase of the discharge #34244 with respective toroidal mode numbers. A high-frequency mode appears as the fluctuation in the radial magnetic field. The low-frequency modes are measured as amplitude modulation in density, temperature and radial magnetic field.

observe changes in the frequency of the mode, toroidal mode number, and its lifetime. The frequency of the mode decreases by a factor of 2 as the input power increases.

Interestingly, for both phases a 'slowing-down' pattern is observed. The change in toroidal mode number  $n$  from -13 to -14 could point towards a change in the location or change in the poloidal structure of the mode. The lifetime of the low-frequency mode shortens with an increase in the input power. In the low heating phase, the duration of the mode is about 10 ms, while in the latter stage it decreases to about 6 ms. However, in the second phase the ELM frequency increases, therefore, the ELM cycle shortens on account of the phase of clamped gradients. Contrary to the low-frequency modes, the high-frequency modes do not change their frequency. They remain locked at 220 kHz in both heating phases. The lifetime of the high-frequency modes is shorter in the second phase. It is of interest to note that the core mode changes in frequency from 7 to 9 kHz with an increase in the input power as the plasma rotation increases.

## 6.4 Localization

For the localization of the low-frequency modes in the pedestal, we use measurements of the ECE diagnostics with a spatial resolution of about 6 mm. With the Electron Cyclotron Radiation transport forward model [Denk, S. S. et al., 2017, Rathgeber et al., 2013] we determine the radial extent of the plasma contributing to the measured signal for each radial channel determined by the birth-place distribution function ( $D_\omega$ ).  $D_\omega$  is defined as the normalized product of the emissivity  $j_\omega$  and transmittance  $T_\omega$ , normalized to its integral representation of the radiation transport equation between the starting  $s_1$  and end point  $s_2$  along the line of sight [Denk, S. S. et al., 2017]:

$$D_\omega = \frac{j_\omega T_\omega}{\int_{s_1}^{s_2} j_\omega T_\omega} \quad (6.1)$$

The radial resolution of a single channel is determined as the FWHM of  $D_\omega$  and its measurement position, so-called 'warm resonance', is determined at the peak of  $D_\omega$ . The plasma edge, is a narrow region of about 2 cm inside the separatrix. Therefore, to accurately diagnose it, a high spatial resolution of any suitable diagnostic is required in this configuration. With the ECE channels, whose spatial resolution is about 6 mm at best, the gradient region is covered by at least three channels, depending on the configuration. The ECE Imaging system on the other hand, with its radial resolution

of about 1.5 cm, comprises almost an entire gradient region within a single channel which is insufficient for precise radial localization. Its main feature, however, is the capability of poloidally resolved measurements (see section 6.5). Hence, for the localization we use measurements of the ECE diagnostic. On the top panels of figure 6.4 we show the radial contribution of the plasma to the measured signal for four adjacent ECE channels. The positions correspond to the peaks of  $D_\omega$  evaluated for each channel. The four channels are shown together with the  $T_e$  profiles 6.4(a) and  $n_e$  profiles 6.4(b) obtained with Integrated Data Analysis (IDA) within the framework of Bayesian probability theory [Fischer et al., 2010]. We show the mean profiles during an inter-ELM interval between 3.145 s to 3.15 s. The selected channels are distributed

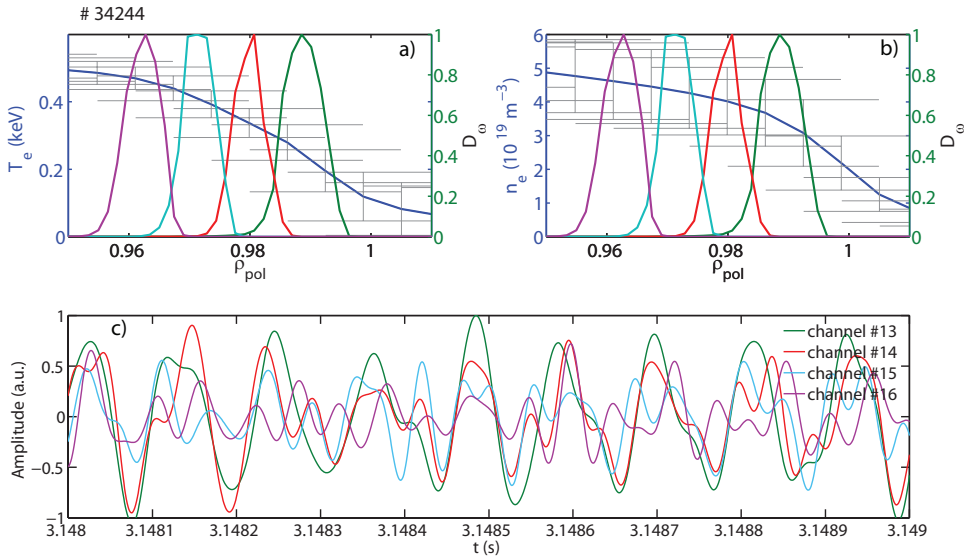


Figure 6.4: Phase relation between the four neighbouring ECE channels measuring in the pedestal. The birthplace distribution of the observed intensity ( $D_\omega$ ) together with  $T_e$  (a) and  $n_e$  (b) profiles. c) Time traces of filtered data measured with those four channels.

with respect to the density profile as shown in figure 6.4(b). The outermost channel #13 measures at  $\rho_{\text{pol}} \sim 0.99$ . Channel #14 is at the position  $\rho_{\text{pol}} \sim 0.98$  and channel #15 is further inside the pedestal top at the  $\rho_{\text{pol}} \sim 0.97$  location. In channel #16 at  $\rho_{\text{pol}} \sim 0.96$  the coherent modulation is vanishing. When compared to the temperature

profiles (see figure 6.4(a)), this translates into a region from the steepest gradients until the temperature pedestal top. The signals measured by those four channels are overlaid in figure 6.4(c) to reveal their relative phase during the 1 ms time interval. Here, a band-pass Fourier filter (7 kHz to 25 kHz ) is applied to the raw data. The correlation between the channels is given in the form of a correlation matrix shown in table 6.1.

Figure 6.5(a) is showing a relative amplitude modulation ( $\delta T/T$ ) measured with

$\rho_{\text{pol}}(\text{chan \#})$	0.96 (16)	0.97 (15)	0.98 (14)	0.99 (13)
0.96 (16)	1	0.25	0.267	0.264
0.97 (15)	0.25	1	0.490	0.397
0.98 (14)	0.267	0.490	1	0.81
0.99 (13)	0.264	0.397	0.81	1

Table 6.1: The correlation matrix between four adjacent channels.

ECE and averaged over the phase of constant frequency during the low-frequency mode. Depicted is the 8.8 kHz component of the signal, alongside with the neighbouring 6 kHz frequency displayed as a green shaded area representing the noise level. As shown, the fluctuation levels for channels #13, #14, #15 are above the noise level with the highest fluctuation amplitude of 14 % measured in channel #13. Channel #16 is within the noise of the system. The magnitude of the measured fluctuations cannot be attributed to the electron temperature fluctuations alone, as a large contribution to  $\delta T/T$  originates from the density modulation. This is shown in [Vanovac et al., 2018a] where 5 % of  $\delta T/T$  in the region of steep gradients is a consequence of a change in the position of the channel due to a density modulation of 10 %. Hence, for an accurate amplitude estimate, we would need absolute values of the density fluctuations associated with this mode in combination with the radiation transport forward model. The relative phase between the channels is depicted in 6.5(b). We do not observe a phase difference between the channels. However, one should be careful when evaluating the relative phase in the presence of density perturbation as the outward shift due to the density can influence the analysis. From the ECE measurements alone, it is only possible to say that the location of the mode is the upper corner of the steep gradient region, towards the pedestal top of the density.

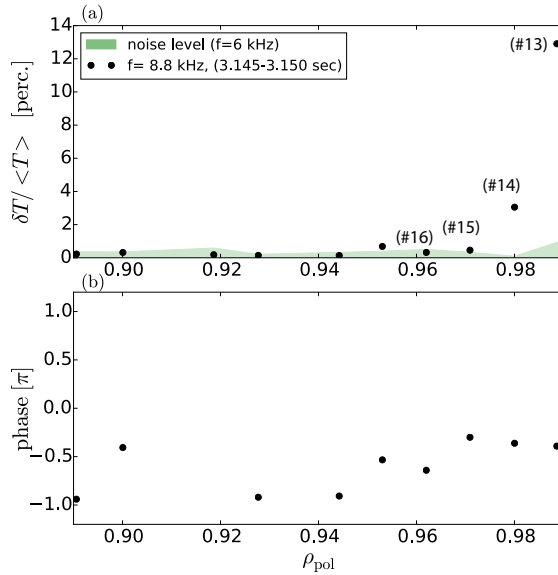


Figure 6.5: Shot # 34244. a) An amplitude of the edge ECE channels averaged over one inter-ELM cycle. b) The phase relation between neighbouring channels.

The amplitude itself is not sufficient for the mode width as small displacements in the steep gradient region will lead to significant relative amplitudes.

## 6.5 Mode structure and poloidal velocity of the mode

The poloidal velocity and the local poloidal wavelength can be determined from the measurements of poloidally distributed channels of the ECE Imaging system. For determination of the spatial structure and poloidal velocity, we use vertically distributed channels aligned along a single flux surface. The corresponding positions are obtained from the electron cyclotron radiation transport forward model. We compare the two different heating phases. This time, we chose two isolated inter-ELM periods, each corresponding to a specific heating phase during which the plasma boundary is kept at the same position. This ensures a stationary position of the mode during measurements. The temporal evolution of the poloidally distributed channels, above the midplane, for shot # 34244 is displayed in figure 6.6. The upper

image shows the mode propagation for the low heating and the bottom one, for the higher heating phase. In this representation, the mode is depicted as a structure (stripe) propagating from the bottom to the top in both cases. In the lab frame, this corresponds to propagation in the electron diamagnetic direction and is in-line with the negative sign of the mode numbers calculated from the magnetic measurements shown in section 6.3, schematically indicated with the black straight lines shown in figure 6.6. The apparent mode velocity measured by ECE imaging for phase I

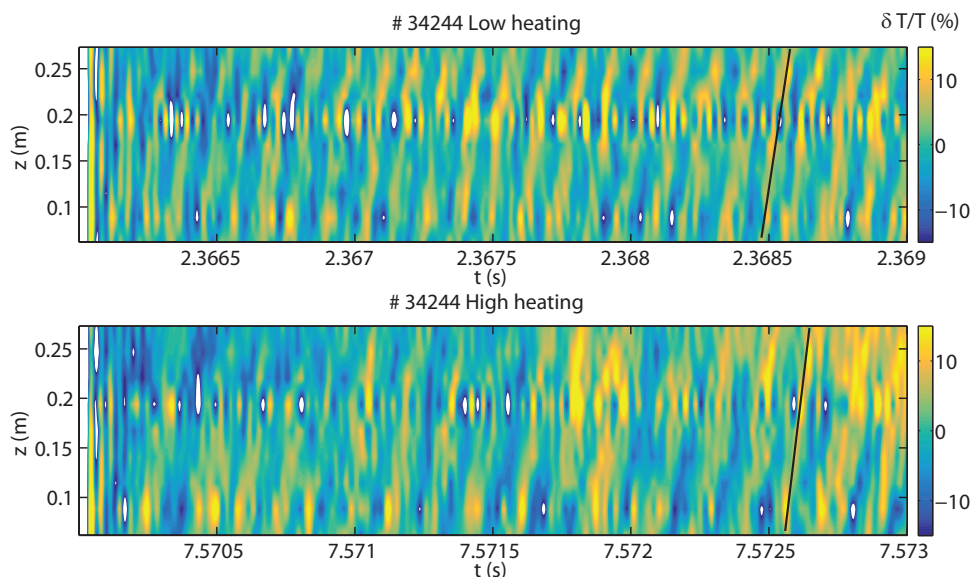


Figure 6.6: Time traces of the ECE imaging channels distributed poloidally along a single flux surface  $q \sim 5.5$  for discharge # 34244. The solid black lines mimic the inclination of the stripes representing the mode moving in the direction from the bottom to the top of the ECE imaging observation window.

is  $v_{\text{mode}} \sim 2.5 \pm 0.5$  km/s, and for the phase II it is  $v_{\text{mode}} \sim 1.5 \pm 0.5$  km/s. These velocities can be compared with the  $E \times B$  flow at the position of the modes. As the mode rotates with the velocity that consists of the velocity of the background flow and the intrinsic phase velocity,  $v_{\text{mode}} = v_{E \times B} + v_{\text{ph}}$ , the comparison would address the phase velocity of the mode. The  $E \times B$  velocity is obtained as  $v_{E \times B} = E_r/B$  where the  $E_r$  is measured by edge Charge Exchange Recombination Spectroscopy



[Viezzer et al., 2013]. For the case of discharge # 34244, the measured  $E \times B$  velocity profiles are shown in figure 6.7 for the two different heating phases. Here we show ELM synchronized data for the two phases labelled in figure 6.1. Note that the  $E_r$  measurements are ELM-synchronized in the time intervals of the scan of the outer plasma boundary. This significantly improves the radial resolution of the system. The radial span of the plasma, corresponding to the ECE imaging measurements from  $\rho_{\text{pol}}$  between 0.97 and 0.99, is over-plotted as the gray shaded vertical area. The horizontal shaded area corresponds to the mode velocity in the range of 1.5 - 3 km/s, measured with the ECE Imaging diagnostic. The cross-section of the two shaded areas corresponds to the region where the  $E \times B$  velocity matches the measured mode velocity of  $v_{E \times B}$  within the uncertainties. Thus, the combination of the two measurements: one from the ECE imaging and another of the  $E_r$  profile, allows for better determination of the position of the mode, which in our case would be in the upper half of the gradient region, closer to the pedestal top. In both cases the mode moves with the poloidal background flow ( $v_{\text{mode}} = v_{E \times B}$ ) and does not have a significant (measurable) intrinsic phase velocity ( $v_{\text{ph}} \sim 0$ ). In the low heating phase, a poloidal wavelength, shown in figure 6.9, is estimated to be  $\lambda_{\text{pol}} = 15 \pm 0.4$  cm, and in the case of the higher heating  $\lambda_{\text{pol}} = 24 \pm 0.4$  cm. This change in the poloidal wavelength is in-line with 50 % change in frequency. The  $q$  profiles for the two heating phases are shown in figure 6.8. Thus, for the first phase where the toroidal mode number is  $n = 13$  and  $q = 5.6$ , the poloidal mode number, calculated as  $m = q \cdot n$ , is  $m = 73$ . For the second phase, with  $n = 14$  and  $q = 5.55$ , the poloidal mode number changes to  $m = 78$ . Taking into account the straight field line angle for the same equilibrium as for the phase I, from the divergence of the field lines in the poloidal direction at the outer midplane, the expected poloidal blob size is about 8 cm at the mode location. The poloidal wavelength is about 16 cm. This matches the experimental findings quite well.

A 50 % change in mode frequency between the two heating phases is observed (see figure 6.3) and the poloidal wavelength changes ( $f = v_{\text{mode, pol}} / \lambda_{\text{pol}}$ ). Given the uncertainty of the  $E \times B$  measurements, it is not possible to determine whether the small change in measured mode velocity matches with the change in the  $E \times B$  velocity. However, the 20 % higher heating power introduces a higher torque and corresponding higher toroidal rotation velocity which can also be seen in a higher core

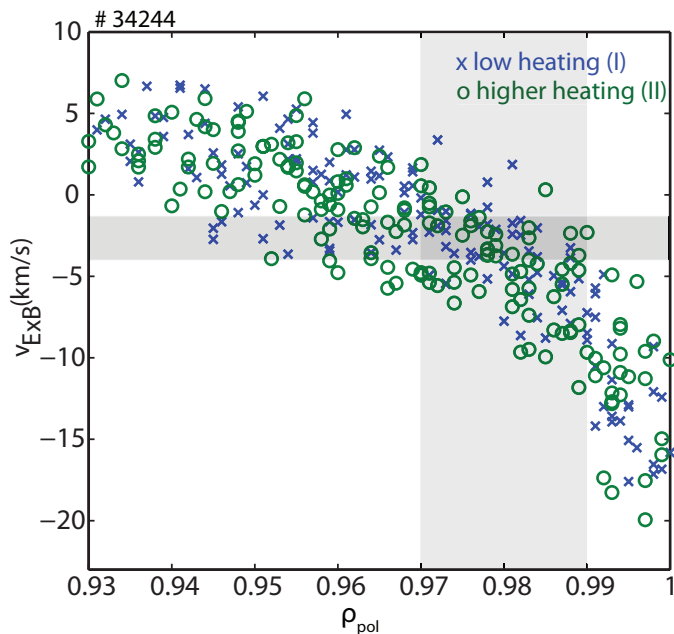


Figure 6.7: ELM synchronized  $E \times B$  velocity measured with the edge Charge Exchange Recombination Spectroscopy diagnostic for two different heating phases, phase I and phase II, shown in figure 6.1.

mode frequency (see figure 6.3). Moreover, the toroidal mode number changes from  $n=13$  to  $n=14$ , and the poloidal wavelength changes from 16 cm to 24 cm. It could be that the mode changes its position, which might still be within the uncertainties of measurements of the  $E \times B$ , mode velocity and its position.

## 6.6 Interaction between inter-ELM modes

As already shown, the location of the low-frequency mode is in the upper part of the gradient region towards the pedestal top in contrast to the high-frequency modes whose position is shown to correspond to the minimum of the  $E_r$  [Laggnier et al., 2016]. The mid-frequency modes are located even further outside - very close to the separatrix [Mink et al., 2016]. The pedestal top and the steepest gradient are separated by about 5 mm; the different modes, therefore, are spatially very close to each

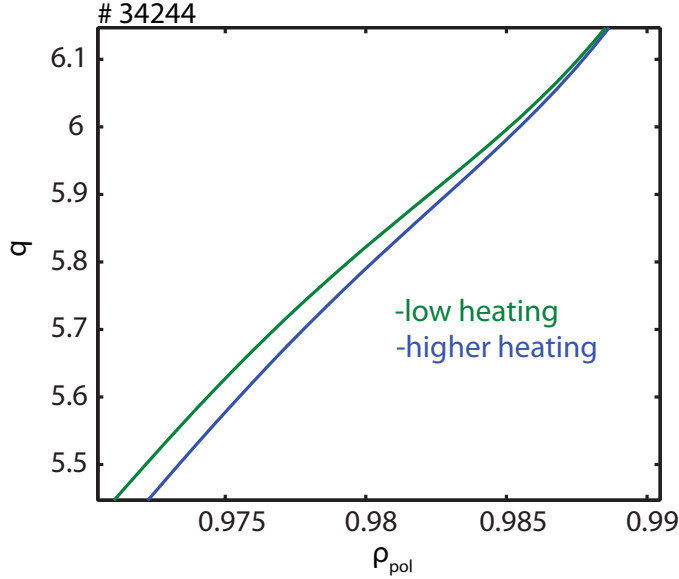


Figure 6.8: The  $q$  profile for two different time points of the discharge #34244. The profile corresponding to the phase of low heating shown in blue and the one during the higher heating phase, shown in green. Zoom into the region of the mode location.

other. If multiple modes spatially overlap, the probability for non-linear interaction between them increases. As the modes are observed in the magnetic signal, the auto-bicoherence analysis could show if there is an energy transfer between the modes (of certain frequency) located in the pedestal region. Auto-bicoherence is defined as:

$$BIC(f_1, f_2) = \frac{\langle |B(f_1, f_2)|^2 \rangle}{\langle |X(f_1 + f_2)|^2 \rangle \langle |X(f_1)|^2 |X(f_2)|^2 \rangle}, \quad (6.2)$$

where  $B(f_1, f_2)$  is defined as:

$$B(f_1, f_2) = X(f_1)X(f_2)X(f_1 + f_2)^* \quad (6.3)$$

For this test, we use the signal measured with the coil #B31-40, located at the outboard midplane. We shown the bicoherence result of one additional discharge #34245. Discharge #34245 is a repetition of discharge #34244. Examples of the

bicoherence results are shown in figure 6.9 and figure 6.10. Figure 6.9 shows the bicoherence calculated for two single inter-ELM phases during the discharge # 34245. As can be seen in figure 6.9(a) significant bicoherence between the triplet  $\sim 15$  kHz,

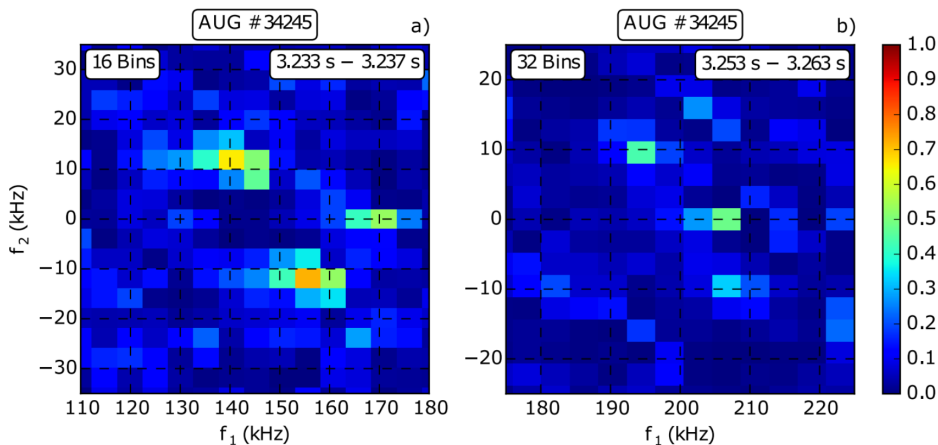


Figure 6.9: Bicoherence analysis for two different inter-ELM phases of single ELMs during the discharge # 34245. a) Coupling between mid and low frequency branches. b) Coupling between high and low frequency branches.

140kHz, and 155kHz is observed. It can also be noted that the maximum bicoherence corresponds to a somewhat lower frequency,  $\sim 12$  kHz which is the frequency of the harmonic of the core mode that is not strongly visible in the magnetic signal. As noted earlier in the manuscript this can largely influence any conclusion as the harmonic of the core mode and the low-frequency mode is in very close proximity. During the next inter-ELM phase, shown in figure 6.9(b), a coupling of the 10 kHz mode to the high frequency  $\sim 205$  kHz mode is observed, thus forming a triplet of frequencies  $\sim 10, 195,$  and  $205$  kHz. In both cases, we observe coupling of the high frequencies to the zero component of the Fourier spectrum. We show another example of coupling of the high-frequency mode to the low-frequency mode, during the discharge # 34244, in figure 6.10.

Increased bicoherence suggests a non-linear coupling between high and low-frequency branches detected in the magnetic signal during inter-ELM periods. The three wave coupling is observed for a few individual inter-ELM phases, and not for

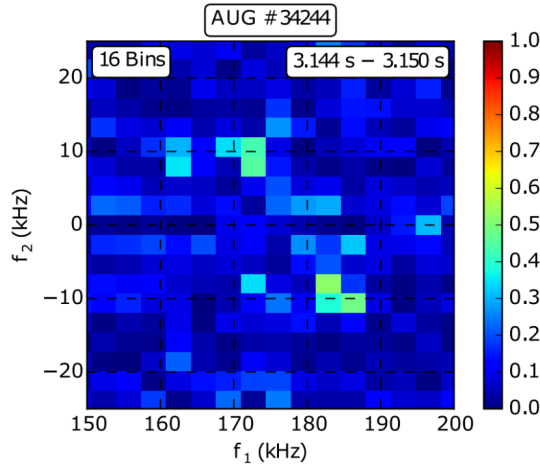


Figure 6.10: Bicoherence analysis for a single inter-ELM during the discharge # 34244.

all ELMs. One of the reasons could be that the low-frequency modes are not always visible in the  $\hat{B}_r$  signal. The results showing a bicoherence for a few individual inter-ELM phases suggest a non-linear coupling between the observed modes in bad curvature region, however, this does not always take place, and is, therefore, not a necessary condition for the appearance of the modes. Quadratic mode coupling at the outer midplane has also been discussed in [Krebs et al., 2013], although during an early stage of a non-linear ELM phase.

## 6.7 Summary and Discussion

This work focuses on the characterization of low-frequency MHD modes appearing in between ELMs. They exist alongside other modes all of which can coexist in close spatial proximity. Their detection and full characterization are therefore not so straightforward. As noted, in the magnetic measurements they can also be hidden behind a strong core mode and its harmonics. The mode of interest appears at a low frequency with slowing down frequency patterns. We measure the low-frequency modes in discharges featuring low-frequency ELMs and long ELM cycles. The low

frequency modes studied in this manuscript appear as the amplitude modulation of the radiation temperature ( $T_{\text{rad}}$ ), electron density ( $n_e$ ), and the radial magnetic field ( $\hat{B}_r$ ). ECE measurements show that the modes are localized in the upper half of the pedestal, unlike the high-frequency modes located in the region of steepest gradients [Laggner et al., 2016]. For the two cases shown in this manuscript, the frequency of the low-frequency modes inversely changes with input power, while the frequency of the high-frequency modes remains constant. This is also valid for all the other inter-ELMs within the two heating phases. The change in the frequency at higher heating power is attributed to a change in toroidal rotation and will be a subject of future work. Although the low- and the high-frequency modes exist in different radial locations inside the plasma edge, a non-linear interaction is possible. This is seen in the bicoherence of the magnetic signal. Possibilities for coupling derive from the fact that the modes are spatially very close, and their spatial structure does not differ significantly (m numbers are found to be very similar). The velocity of low-frequency modes matches the  $E \times B$  velocity at the location of the modes within the uncertainties and does not significantly change for individual ELM cycles. The fact that the low-frequency modes appear alongside the high-frequency modes points towards the same or similar plasma conditions required for those to exist. As it has already been reported in [Laggner et al., 2016], the high-frequency modes appear when the gradients are clamped to a fixed value. However, the low-frequency modes may also appear somewhat later in this phase. How the appearance of the low-frequency mode influences the pedestal evolution, and its stability remains an open question. Also, it remains unclear whether the modes are ideal or resistive. The studies made in Reference [Fitzpatrick, 1995] explore the temperature perturbations associated with tearing modes. From this reference, we use the expression for the critical island width ( $w_c$ ) that could cause a signature in the ECE data. The parallel heat conductivity is approximated by the Spitzer-Härm<sup>†</sup> formula [Spitzer and Harm, 1953] and values for perpendicular heat conductivity are estimated from the experiment and varied within one order of magnitude (see Table 6.2). The critical island widths,  $w_c$ , for a mode located at the pedestal top and toroidal mode number of  $n = 13$ , are shown in Table 6.2. In order to cause a temperature modulation and increased local transport,

---

<sup>†</sup>  $\chi_{\parallel,SH} = 3.6 \times 10^{29} \times \frac{T_e[\text{keV}]^{3/2}}{n_e[\text{m}^{-3}]} [\text{m}^2/\text{s}]$

$\chi_{\parallel} [m^2/s]$	$2 \times 10^7$	$1 \times 10^8$	$5 \times 10^8$
$\chi_{\perp} [m^2/s]$			
0.1	3.3mm	2 mm	1.5 mm
0.3	4.3 mm	2.9 mm	1.9 mm
1	5.8 mm	3.9 mm	2.6 mm

Table 6.2: Calculated critical island widths  $w_c$ , following [Fitzpatrick, 1995]

the island width  $w_d$ , has to be bigger then  $w_d > 1.5w_c$  [Hoelzl, 2010]. Only the larger island widths in this estimate would cause a phase jump in the ECE channels. The smaller ones cannot be resolved. From the observations of the neighbouring ECE channels, we have seen that the amplitudes are in phase (see figure 6.5). This points toward an ideal mode rather than a tearing mode. However, further probing is planned using the correlation ECE diagnostics [Freethy et al., 2016], with its better spatial resolution (2 - 3 mm) to clarify the possibility of an island at the pedestal top. The existence of such an island could prevent the pedestal top from growing further inwards, thus preventing an ELM from happening. A similar proposal on the existence of the 'wall' at the pedestal top has been made in [Snyder et al., 2012] although in a different plasma scenario where ELM suppression is achieved with 3D fields. The two scenarios are not directly comparable, but the phenomenology of the mechanism could be similar. Nevertheless, the very accurate characterization of a low-frequency mode near the pedestal top, regarding its amplitude, location, poloidal and toroidal structure and velocity, can serve as a basis for comparison between experiment and non-linear modeling as done for example in [Mink et al., 2018].

# Chapter 7

## Parameter space of low-frequency modes

In previous chapters, the study focused on the low-frequency modes in a limited range of plasma parameters. However, the low-frequency modes appear in many discharges featuring low ELM repetition rate ( $f_{\text{ELM}}$ ). In this chapter a broader parameter space of plasma parameters, in which the low-frequency modes appear is explored and discussed.

### 7.1 Power spectrum of modes

The ELM cycle of type-I ELMs consists of different phases characterized by the evolution of kinetic profiles on different time scales [Burckhart et al., 2010] and distinct MHD and turbulence activity. In the last phase of the ELM cycle, the pressure gradients are clamped. During this phase low [Vanovac et al., 2018b], medium [Mink et al., 2016] and high frequency [Laggner et al., 2016] MHD modes develop simultaneously in the steep gradient region. The high-frequency modes are located close to the minimum of the  $E_r$  well, and are measured as fluctuations in the radial magnetic field on both, low and high field side [Laggner et al., 2016]. As explained in the previous chapter the low-frequency modes are visible at the low field side and are located in the upper part of the steep gradient region [Vanovac et al., 2018c]. They appear as modulation in electron density, electron temperature and as magnetic



fluctuations. These modes rotate poloidally in the electron diamagnetic direction with the velocity of the background flow at that position [Vanovac et al., 2018c]. They show a slowing down frequency pattern (for example see figure 6.3) with a distinct peaking in frequency during their lifetime. The nature of this mode is not yet clear. An example of a power spectrum, in the low and the high-frequency range for inter-ELM synchronized measurements during the discharge #34347, is shown in figure 7.1. On the left panel, the mean amplitude of four different ECE radial channels is depicted, showing the activity in the low-frequency range of the spectrum during the inter-ELM phase. The resonant positions are color-coded and span from the Scrape-Off Layer region towards the confined region, close to the pedestal top. Increased power in the spectrum is measured in the range of 10 kHz in all shown channels. The outermost channel, resonant around the separatrix at  $\rho_{\text{pol}} = 1.007$ ,

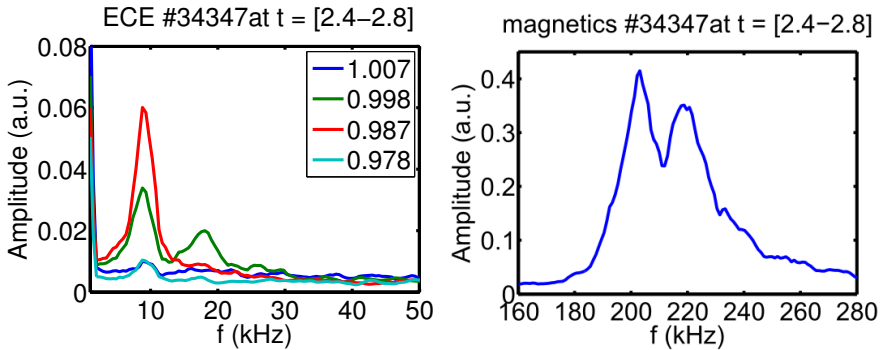


Figure 7.1: ELM synchronized amplitude spectrum of radially resolved ECE channels (left) for the low-f mode, and magnetic pick-up coil (right) for the high-f mode. The radial channels of the ECE are color-coded. Both diagnostics measure on the low field side.

measures the emission of the relativistically down-shifted electrons from the pedestal region [Denk et al., 2017]. The channel closest to the separatrix (in green), resonant inside the confined region, shows two prominent peaks. The first peak, at 10 kHz corresponds to the fundamental frequency of the mode, and the second one to its harmonic. The largest amplitude (shown in red) is measured in the signal resonant at the position of the steepest temperature gradient. The mode is also measured further inside, at  $\rho_{\text{pol}} = 0.978$ . The low-frequency modes appear at the clamping of the

pressure gradient, therefore, coinciding with the appearance of the high-frequency mode as discussed in chapter 6. In the right panel, an average spectral amplitude of high-frequency modes during an inter-ELM phase is shown. The high-frequency modes are measured only with the magnetic diagnostics. Multiple peaks in the Fourier spectrum of the magnetic signal appear, although there are two prominent ones; the one at 206 kHz and the one at 220 kHz.

The low-frequency modes can be characterized by their frequency, amplitude and toroidal mode numbers. The focus of this chapter is solely on their frequency obtained from ECE measurements in connection to the plasma parameters.

## 7.2 Mode frequency in comparison with plasma parameters

### 7.2.1 Database overview

The low-frequency modes differ for individual ELMs, which makes the ELM synchronized analysis quite difficult when it comes to examining the fine structure and temporal resolution during an inter-ELM phase. However, to examine the tendencies, the comparison with specific plasma parameters and discharge conditions is possible with the ELM-synchronization approach. Therefore, different phases of various discharges, where the low-frequency modes are detected in the average amplitude spectrum of the ECE diagnostic (see figure 7.1(left)) are identified and analyzed. The database features discharge phases with moderate pedestal top density  $n_e^{\text{ped}} < 5 \times 10^{19} \text{ m}^{-3}$  to avoid cut-off of the ECE signal (see chapter 4) and heated with low auxiliary power to obtain a low repetition frequency of ELMs ( $f_{\text{ELM}} \sim 50 \text{ Hz}$ ), hence long inter-ELM periods. The phases in which modes were not observed are also included in the analysis and are denoted with zero frequency. Parameters were constant during the  $\approx 200 \text{ ms}$  averaging time. The error bars associated with mode frequency correspond to the spreading around the central peak frequency. Figure 7.2 shows the distribution of mode frequency with the edge safety factor. The database is comprised of discharges with two different plasma currents ( $I_p \sim 0.6$  and  $0.8 \text{ MA}$ ) and same magnetic field ( $B_t \sim 2.5 \text{ T}$ ). As the  $q_{95} \sim B_t/I_p$  is a function of plasma current and magnetic field, the distribution is grouped around two values of the edge safety factor

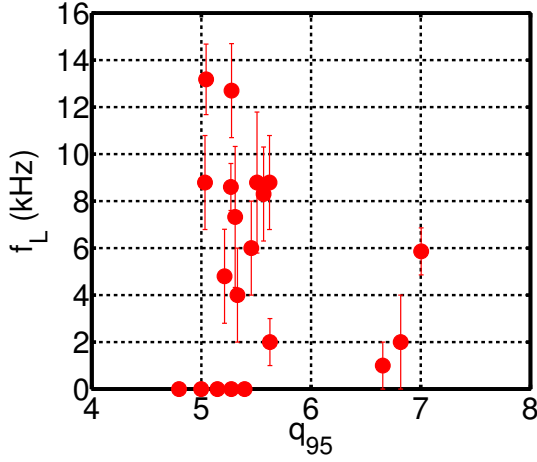


Figure 7.2: Mode frequency as a function of the edge safety factor  $q_{95}$ . The database covers two different values of the plasma current and, as the magnetic field is very similar for all the discharges, the data are grouped around two values of the edge safety factor.

$q_{95}$ . Overall there is no clear trend. For higher  $q_{95}$  the mode frequency does not go above 6 kHz within this database. The phases with no modes present are all identified within the discharges with  $I_p \sim 0.8$  MA.

### 7.2.2 Input power dependency

In the previous chapter, it has been noted that for two isolated inter-ELM modes, the frequency decreased by a factor of 2 for an increase in the input power of  $\sim 1$  MW. For the set of discharges presented in this chapter, the same tendency is observed. Figure 7.3 shows the dependency of the low-frequency  $f_L$  and high-frequency  $f_H$  modes on the input power  $P$ . Colour-coded is the Electron Cyclotron Resonance Heating (ECRH) in green, Neutral Beam Injection (NBI) in black and the total power ( $P_{TOT}$ ) shown in red. As shown in figure 7.3(a)  $f_L$  decreases with increasing NBI power. This change in frequency of the low-frequency modes is mainly driven by the increase in the toroidal rotation, as shown in figure 7.4, concomitant with the increase in NBI power which is consistent with previous observations reported in

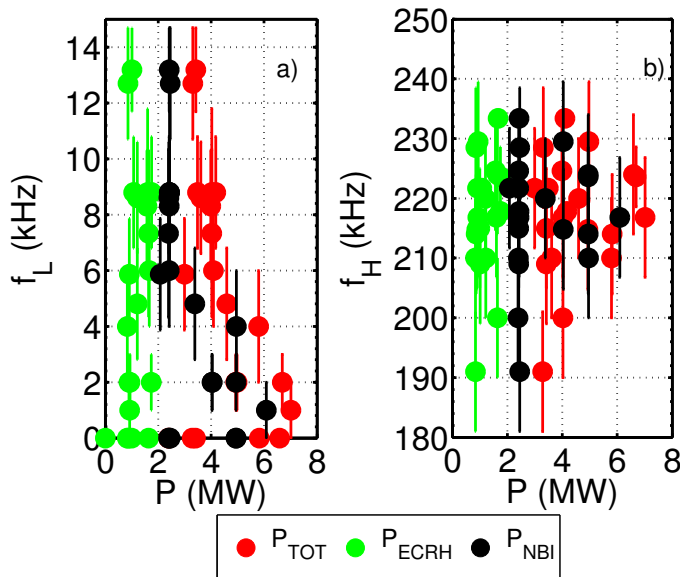


Figure 7.3: Mode frequency in relation to the input power, where the total input power is shown in red, ECRH power in green and NBI power in black for a) low frequency modes and b) high frequency modes.

[Vanovac et al., 2018c]. No explicit dependence on the ECRH power is observed. Contrary to this observation, the frequency of the high-frequency modes, shown in figure 7.3(b), does not show any dependence in the range of powers discussed in this work. Their frequency remains scattered in the range of 190 - 240 kHz with no clear trend. This observation suggests that the high-frequency modes are not affected by the change in toroidal rotation at all as they are located in the steep  $E_r$  well where the toroidal rotation has negligible contribution. At this location their frequency is mainly driven by the poloidal flow and for such a high frequency the toroidal component is negligible. Figure 7.4 shows the mode frequency as a function of toroidal rotation evaluated at  $\rho_{pol} = 0.96$ . Color-coded data points correspond to two different data sets of average triangularities. Here, the mean triangularity is defined as  $\langle \delta \rangle = (\delta_u + \delta_l)/2$ , where the  $\delta_u$  and  $\delta_l$  are upper and lower triangularity, respectively. High  $\langle \delta \rangle$  (blue dots) represents the values of  $\langle \delta \rangle$  larger than 0.26. Low  $\langle \delta \rangle$  (red dots) are smaller values. The constant 0.26 is the average value of  $\langle \delta \rangle$

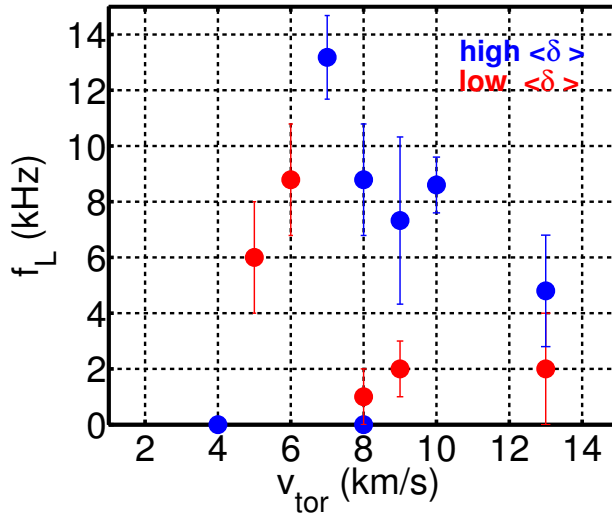


Figure 7.4: Mode frequency as a function of the toroidal rotation of the plasma measured with the CXRS diagnostic and evaluated at  $\rho_{\text{pol}} = 0.96$ . The colours denote phases corresponding to different mean triangularities  $\langle \delta \rangle$ . High  $\langle \delta \rangle$  (blue) is chosen for  $\langle \delta \rangle > 0.26$  and low  $\langle \delta \rangle$  (red) is chosen if  $\langle \delta \rangle < 0.26$ , with 0.26 being the average value of  $\langle \delta \rangle$  within the database. Note that the CXRS measurements are not available for the entire database.

within the database. The two zero-frequency phases are part of the dataset with high  $\langle \delta \rangle$ . Both, high and low triangularity show decrease of the mode frequency with increasing toroidal velocity.

Another parameter considered here is the ELM repetition frequency. The mode frequency decreases with an increase in the  $f_{\text{ELM}}$  as shown in figure 7.5. A decreasing trend in the mode frequency is also observed for an increasing plasma shaping  $\langle \delta \rangle$ , as shown in figure 7.6. Shaping (triangularity) of the plasma is known to change the stable region in the pressure gradient and edge current density space (for example see figure 2.4). With increased shaping, the bad curvature area is reduced, and the stable region is increased towards higher pressure gradients and edge current densities. Within the database, mode amplitudes are not assessed. Hence the stability regions cannot be discussed. Only the mode frequency, hence the location of the mode, is

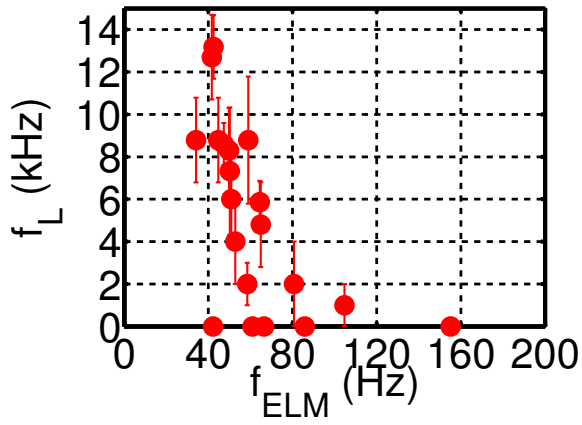


Figure 7.5: Mode frequency as a function of the ELM repetition rate  $f_{ELM}$ .

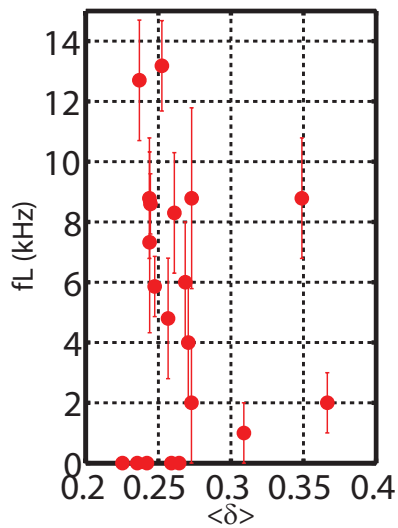


Figure 7.6: Mode frequency as a function of plasma shaping.

analyzed. As can be seen, in most cases, the low-frequency modes appear during the ELM cycles with low repetition rate  $\sim 50$  Hz and low average plasma triangularity  $\langle \delta \rangle$ , where the inter-ELM phases are long enough for modes to develop.

### 7.2.3 Mode velocity

As discussed in chapter 6 the low-frequency modes are localized in the upper part of the steep gradient region, close to the pedestal top, and they rotate with the  $E \times B$  velocity at that position. The  $E \times B$  velocity is determined as  $v_{E \times B} = E_r/B$  where the radial electric field  $E_r$  is an element of the force balance equation:

$$E_r = v_{i,\text{tor}} B_{\text{pol}} - \frac{\nabla p_i}{q \cdot n_i} - v_{i,\text{pol}} B_{\text{tor}}, \quad (7.1)$$

where  $v_{\text{tor}}$  and  $v_{\text{pol}}$  are toroidal and poloidal ion fluid velocities, and  $B_{\text{tor}}$  and  $B_{\text{pol}}$  are toroidal and poloidal magnetic field components, respectively.  $\nabla p_i$  is the ion pressure gradient,  $q$  the ion charge, and  $n_i$  the ion density. An illustration of the radial electric field profile along normalized plasma radius in the pedestal region is given in figure 7.7. The radial electric field outside the separatrix ( $\rho = 1$ ) is governed by the gradient of the electron temperature in the SOL region [Chankin et al., 2007, Stangeby, 2000]. In the plasma core the  $E_r$  profile is dominated by the toroidal velocity ( $v_{\text{tor}} B_\theta$ ) term whereas in the pedestal, the pressure gradient ( $\nabla p/qn$ ) term is more significant [Schirmer et al., 2006, Viezzer et al., 2013]. In between the two regions, the velocity is driven simultaneously by pressure gradient and toroidal rotation. As the mode discussed in this work is localized in between the two regions, both contributions are expected to be significant. For the case of the high frequency modes, as discussed in the work of Laggner et al (see [Laggner et al., 2016]), the mode frequency is a linear function of  $\nabla p/n_i$ . Hence, it is concluded that the high frequency modes are located in the minimum of the  $E_r$  well. As in this region the pressure gradient term is dominant, their velocity (frequency) can be expressed as:

$$v_{\text{mode}} = v_{E \times B} + v_{\text{ph}} \approx E_r/B + v_{\text{ph}} \approx \frac{1}{B} (\nabla p/en) + v_{\text{ph}}. \quad (7.2)$$

Contrary to this, the low frequency modes are localized in the region close to the pedestal top, where the influence of the core plasma parameters is not negligible. In this case the velocity (frequency) is determined as:

$$v_{\text{mode}} = v_{E \times B} + v_{\text{ph}} \approx E_r/B + v_{\text{ph}} \approx \frac{1}{B} (\nabla p/en - v_{\text{tor}} B_{\text{pol}}) + v_{\text{ph}}. \quad (7.3)$$

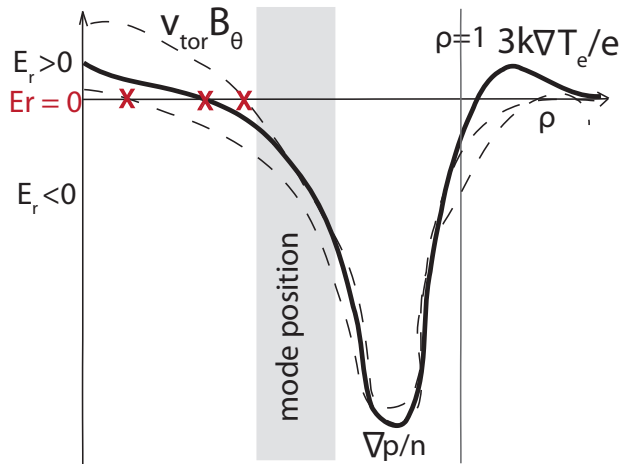


Figure 7.7: Illustration of the  $E_r$  profile as a dark solid line at the plasma edge, where a large variation of  $E_r$  is observed. The dashed black lines indicate possible variation of the  $E_r$ . At zero crossings the  $E \times B$  velocity is zero. Zero crossings of  $E_r$  are marked in red. The mode location is illustrated by the grey shaded area.

This is supported by the experimental findings shown in figure 7.3 where a change in mode frequency is observed for low frequency modes (see figure 7.3(a)) and not for high frequency modes (see figure 7.3(b)). The negative sign in front of the term  $v_{\text{tor}} B_{\text{pol}}$  means that an increase in the toroidal rotation will decrease the velocity of modes. The slowing down pattern with NBI heating power (see figure 7.3(a)) is attributed to the change in the rotation further inside the pedestal top. In the steep gradient region, for high collisionality regimes, the ion pressure gradient contributing to equation 7.1 can be approximated by the electron pressure gradient ( $\nabla p_i / en_i \sim \nabla p_e / en_e$ ). The frequency of low- and high-f modes, against the electron pressure gradient term  $\nabla p_e / en$ , where  $\nabla p_e$  is taken at its maximum is displayed in figure 7.8(a) and (b), respectively. The low-f modes slow down as the  $\nabla p_e / en$  term increases. In parallel, the high-f modes show no clear tendency as the  $\nabla p / en$  changes. In order to resolve a change in frequency of high-f modes, the input power range has to be larger than the ones comprised within this database.



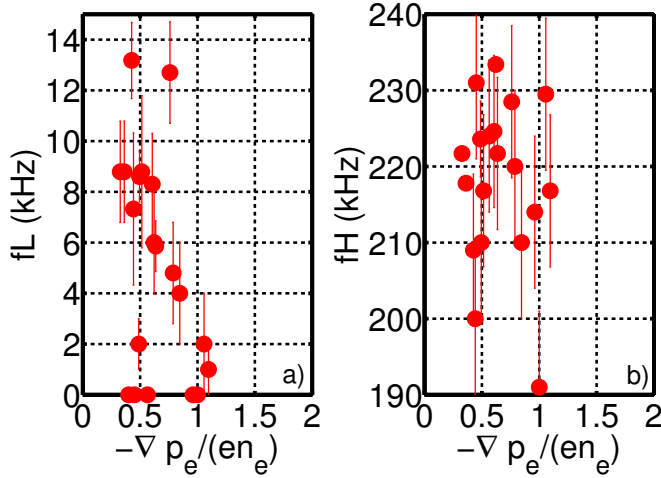


Figure 7.8: Mode frequency as a function of the  $-\nabla p_e / (en_e)$  for a) low-frequency modes and b) high-frequency modes. The pressure gradient is taken at its maximum, the electron density is evaluated at  $\rho_{\text{pol}} = 0.98$  and  $e$  is the electron charge.

#### 7.2.4 Mode frequency in relation to the global $\beta_p$

The  $f_L$  as a function of  $\beta_p$  is shown in figure 7.9 where the global  $\beta_p$  is defined as the volume averaged pressure across the whole plasma, normalized by the average squared poloidal magnetic field. For higher values of  $\beta_p$  the frequencies of the low-frequency modes decrease. From the PB theory, the value of  $\beta_p$  determines the pedestal width, and an increase in  $\beta_p$  stabilizes the pedestal (see figure 2.5). While the pedestal pressure gradient is similar for the inter-ELM cycles considered here (see figure 7.8), an increase in  $\beta_p$  leads to a widening of the pedestal. As the position of the mode is determined to be close to the pedestal top, a widening of the pedestal moves the mode further inside, towards lower values of the radial electric field. Hence the frequency of the mode decreases.

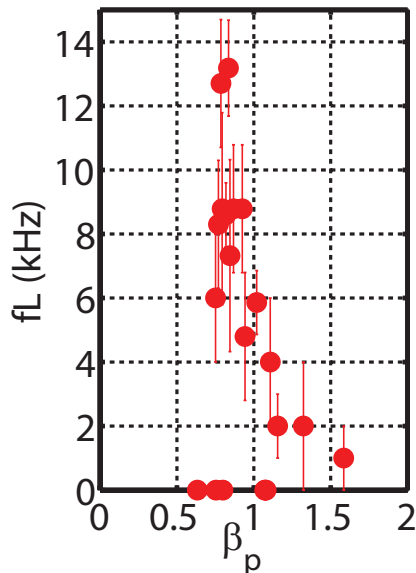


Figure 7.9: Mode frequency as a function of  $\beta_p$ .

### 7.3 Discussion

In summary, the low-frequency modes only appear in phases with low ELM repetition frequency. In phases of high  $f_{\text{ELM}}$  and concomitant increase in plasma heating, the modes are not observed. Also, as shown in chapter 6, the lifetime of the modes shortens on account of the phase of the clamped pressure gradients suggesting that modes do not have enough time to develop.

Additionally, the dependency of the frequency of low- $f$  modes is determined to be a consequence of NBI-induced toroidal rotation. Hence, the mode velocity is determined as an interplay between the core toroidal plasma flow and the value of  $\nabla p/n$  term. Within the database examined in this work, the  $\nabla p/n$  does not change significantly as the high-frequency modes, sensitive solely to this component, do not show any dependence within the dataset.

Moreover, the clear dependence of the mode frequency on global  $\beta_p$  displays the influence of the Shafranov shift on the mode position. As  $\beta_p$  increases, the pedestal widens, and the pedestal top moves further inwards while the pressure gradient

remains constant. As a consequence, the mode located at the pedestal top is shifted further inwards towards lower values of the radial electric field leading to a decrease in its frequency. Following this pattern, a further increase in Shafranov shift would lead to zero crossing of  $E_r$ , leading to a change of the sign of the rotation of the mode, as it would entirely be dominated by the  $v_{\text{tor}}B_\theta$  term. This would result in a slowing down of the mode frequency and finally a change of the sign of the mode rotation. Similar slowing-down patterns are observed for two isolated inter-ELM phases as discussed in chapter 6 (see figure 6.3). The inter-ELM modes show a decrease in frequency during their lifetime which can be interpreted as the effect of the widening of the pedestal as described above.

# Chapter 8

## Conclusions and outlook

As suggested in the outline of the thesis, in chapter 1, the core of this thesis work can be divided into two parts; one which is related to the diagnostic effects and the diagnostic performance when measuring in the pedestal, and the second one related to the identification and characterization of modes measured during the ELM cycle in the pedestal. In this chapter, the main results regarding the topics mentioned above are summarized, and suggestions for future studies conclude the thesis.

### 8.1 Conclusions

The high confinement regime is the envisaged operational regime of future fusion reactors, with its unique feature appearing in the edge of the plasma. An MHD instability, Edge Localized Mode, limits the pedestal properties and the core confinement, necessary for the required fusion gain. The ELM crash does not come alone - it is accompanied by different long- and short-lived MHD and turbulent activities announcing the coming ELM crash. Some of those instabilities might be responsible for a delay in the crash of the pedestal, as the pedestal itself evolves along the kinetic ballooning (soft) limit long before the crash, according to the predictive pedestal model.

The main diagnostic tool in this work is the upgraded Electron Cyclotron Emission Imaging diagnostic that provides a two-dimensional distribution of temperature fluctuations. The diagnostic itself has been upgraded with the second array added and

toroidally separated by about 40 cm from the first array. Due to spatial constraints, both arrays have an additional toroidal viewing angle that is superimposed onto poloidally distributed angles of each line of sight. With this toroidal angle, a new set of diagnostic effects emerged. To provide an accurate characterization of inter-ELM instabilities, locality and sensitivity of the ECE imaging when measuring in the pedestal is examined thoroughly. This is done with the electron cyclotron radiation transport forward model which includes the realistic geometry of the ECE Imaging and its beam properties. In the following, the research questions posed in chapter 1, are presented.

*Are the measurements in the Scrape-Off Layer with the ECEI system feasible? Is it possible to associate relevant temperature fluctuations to the filamentary structures expelled during an ELM crash?*

As shown in chapter 4, relativistic downshift of the electrons is an important feature appearing almost in every H-mode discharge taken into analysis. This effect is known as the 'shine-through' effect and comes from non-absorbed down shifted emission, hence causes the radiation temperature to exceed/differ from the electron temperature in the Scrape-off layer region. Indeed, the radiation temperature of channels with cold resonance in the SOL depends on the pedestal electron temperature and can be used as a constraint for reconstructing  $T_e$ . However, due to this effect, the ECE imaging measurements in the SOL region are not feasible in steady state conditions, i.e., during the inter-ELM interval. Moreover, in chapter 5 studies on transient effects were presented. In this study, the 2D profiles of density and temperature during an ELM crash from the non-linear MHD code JOREK are used as an input for the electron cyclotron radiation transport forward model. It is shown that the presence of ELM filaments in the SOL region can change the optical depth locally, due to the locally higher density and temperature. Therefore both, shine-through as well as the local emission can be observed simultaneously along the flux surface. Nevertheless, in this case, it is difficult to distinguish between the two contributions without additional local density measurements.

*Are the main kinetic broadening mechanisms like relativistic, and Doppler shift-broadening enhanced due to the toroidal observation angle, and how do they reflect*

*in the radial resolution of the system? How are the measurement positions affected by this change in the geometry of the system?*

Another study performed and discussed in chapter 4 shows how the toroidal angle affects the radial resolution and channel position of the ECE Imaging system. The radial resolution is decreased as the plasma volume contributing to the measurements increases due to the Doppler broadening. Additionally, the measurement positions of the channels resonant inside the confined region are Doppler-shifted further outside, towards lower magnetic field values. For the inner-most channels, this shift is about 1.5 cm and has to be taken into account when mapping the measurements onto the normalized radius. So-called warm resonant positions have to be used instead of the cold resonances. When measuring at the plasma edge, the forward modeling is necessary for every channel of the ECE Imaging system at ASDEX Upgrade in order to obtain the correct location of the measurement.

*How much of the fluctuation signal measured with ECE imaging, which is considered a temperature diagnostic, is affected by the variation of the density at the plasma edge?*

The effects of density are studied for the case of ECE Imaging and profile ECE diagnostics. It is shown that both diagnostics are sensitive to the presence of density modulation. Even in the complete absence of temperature fluctuations, both diagnostics are measuring up to 5 % modulation in temperature for assumed 10 % density fluctuations in the model. Hence, the real electron temperature fluctuations can be assessed with neither ECE imaging nor ECE nor CECE, and they all suffer from the density effect in the presence of large density fluctuations. Additionally, the phase measurements with the CECE can be affected as the density effect can also modify the phase by shifting the channels towards a lower magnetic field value.

In summary, when addressing the electron temperature fluctuations in the pedestal with ECE imaging & ECE two things are essential: Forward modeling of the electron cyclotron radiation and the knowledge on the amplitude and phase of the density fluctuations. Only then a correct localization and amplitudes of the electron temperature fluctuations can be assessed.

Furthermore, the ELM cycle of type-I ELMs is diagnosed with the highest possible accuracy using the variety of available edge diagnostics at ASDEX Upgrade. The inter-ELM instabilities are identified evolving along the P-B limit where the pressure gradients are clamped. Alongside previously identified modes in the high-frequency part of the spectrum (see references [Bolzonella et al., 2004, Lagner et al., 2016, Mink et al., 2016]), the measurements have shown the dominant inter-ELM mode in the low-frequency part of the spectrum on both ECE and ECE Imaging measurements. This mode is denoted as the low-frequency mode.

*What is the experimental signature of the low-frequency mode?*

As discussed in chapter 5 and chapter 6, the low-frequency mode appears in multiple H-mode discharges featuring low-frequency type-I ELMs, which have low heating powers ( $< 7\text{MW}$ ). It is identified at the bad curvature region (low-field side) in a variety of edge diagnostics: magnetic measurement, temperature fluctuations, density fluctuations. The frequency of detected modes is in the range of 2-14 kHz. Within the lifetime of a single mode, a distinct slowing down frequency pattern is observed (see figure 6.3). The measurements of the magnetic coils distributed toroidally and poloidally around the vessel, have shown the same activity but only when the plasma is closest to the wall. The same modulation is simultaneously measured in the Li-BES diagnostic that is sensitive solely to density fluctuations.

*What are characteristics of the mode regarding its position, mode velocity, spatial structure?*

The mode is localized in the upper part of the steep gradient region towards the pedestal top of the electron density. The poloidal mode velocity, for isolated inter-ELM cases discussed in chapter 5 and chapter 6 is changing from  $1.5 \pm 0.5$  to  $3 \pm 0.5$  km/s and their toroidal mode number changes. Furthermore, as demonstrated in chapter 7, the mode frequency is shown to be driven by the NBI-induced toroidal rotation of the plasma. Hence the mode velocity should be expressed as:

$$v_{mode} = v_{E \times B} + v_{ph} \approx \frac{1}{B}(\nabla p/en - v_{tor}B_{pol}) + v_{ph}. \quad (8.1)$$

A comparison with the measured  $E \times B$  velocity for two isolated inter-ELM cases mentioned above and discussed in chapter 6 leads to the conclusion that the phase velocity of the mode is close to 0, and the mode rotates with the  $E \times B$  velocity at its location. As the low-frequency modes are visible in the magnetic signal in short time intervals with the plasma being close to the wall, the mode analysis is not systematically performed. However, the identified range of toroidal mode numbers spans between  $n=11-14$ .

*What is the nature of the mode, is it resistive or ideal?*

As explained in the Summary section of chapter 6, the theory allows for the existence of an island with the characteristics of the low-frequency mode. However, from the observations of the adjacent ECE channels, it is seen that the amplitudes are in phase (see figure 6.5) which points toward an ideal mode rather than a resistive mode. Nevertheless, as the amplitude of the mode is not assessed and compared with parameters driving the instabilities, this question remains unanswered.

*How does the mode behave when changing plasma parameters such as pressure gradient, plasma heating? Is it possible to identify the upper and the lower threshold in plasma parameters where modes are not visible for the diagnostic?*

The low-frequency modes appear in phases with low ELM repetition frequency. In phases of high  $f_{\text{ELM}}$  and at the high power levels, the modes are not visible in the data. Also, as shown in chapter 6, the lifetime of modes shortens on account of the phase of the clamped pressure gradients suggesting that, for short inter-ELM cycles, modes do not have enough time to develop. As explained in chapter 7, the variation of the pressure gradient within the database does not largely influence the mode frequency. Within the database examined in this work, the  $\nabla p/n$  does not change significantly as the high-frequency modes, sensitive solely to this component, do not show any dependence within the dataset. Moreover, a clear dependence of the mode frequency on global  $\beta_p$  displays the influence of the Shafranov shift on the mode position. As  $\beta_p$  increases, the pedestal widens. Therefore, the pedestal top moves further inwards while the pressure gradient remains constant. As a consequence, the mode located at the pedestal top is shifted further inwards towards lower values of the radial electric field leading to a decrease in its frequency. Following this pattern,



a further increase in Shafranov shift while keeping the low heating of the plasma would lead to zero crossing of the  $E_r$  (see figure 7.7), leading to a change of the sign in the rotation of the mode as the mode would completely be dominated by the  $v_{\text{tor}}B_\theta$  term. Similar slowing-down patterns are observed during isolated inter-ELM phases discussed in chapter 5 and chapter 6 (see figure 6.3). In this framework, the inter-ELM modes show a decrease in frequency during their lifetime, suggesting a similar mechanism of pedestal widening within the inter-ELM cycle.

Characterization of this low-frequency mode regarding its location, structure and mode numbers is performed using a variety of diagnostics, giving an accurate input for MHD or gyrokinetic codes. Moreover, the MHD inter-ELM modes identified so far at ASDEX Upgrade are shown in figure 8.1. The mode identified within this work is of the highest mode numbers and localized in the upper half of the pedestal towards the pedestal top. This increase in toroidal mode number with the decrease in  $\rho_{\text{pol}}$  of the mode location is in-line with previously identified mid- and high-frequency modes, reported in [Laggner et al., 2016] and [Mink et al., 2016] respectively.

## 8.2 Outlook

Further improvements to the diagnostic system and new research questions have arisen during this work. With that in mind, in the following, some of the new and old ideas, that have not been addressed in this work are listed.

As discussed and concluded, the correct interpretation of the ECE imaging measurements in the plasma edge requires a forward model of the electron cyclotron radiation as well as accurate measurements of density fluctuations. Improvements in the diagnostic geometry such as an observation angle perpendicular to the magnetic field would yield more local measurements of the radiation temperature with the Doppler shift being negligible. Thus the warm resonances could coincide and be approximated with the cold resonances, as is the case for the standard ECE system. Further improvements in the diagnostic direction involve expanding the range of available local oscillator (LO) frequencies, such that also scenarios with the lower magnetic field are accessible. This would extend the applicability range of the ECE imaging system towards the ELM suppression and mitigation discharges. Those

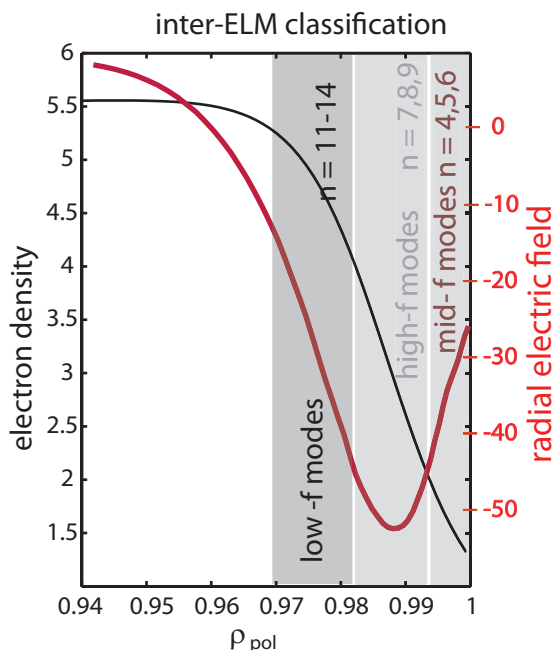


Figure 8.1: Inter-ELM instabilities identified during the type-I ELM cycle at ASDEX Upgrade. The subject of this thesis is the modes located close to the density pedestal top, with the largest identified toroidal mode numbers. The common feature of all three types of modes is their appearance in the phase of the clamped pressure gradient. Their velocity is governed by the values of the radial electric field  $E_r$  at respective locations, indicated as the solid red line. The density profile typical for the H-mode discharges featuring low-frequency inter-ELM modes is shown as the solid black line.

discharges are performed at low magnetic fields ( $\sim 2$  T on axis), such that the externally applied perturbation fields can affect the plasma boundary. The work presented here explores the ELM cycle of type-I ELMs. No other scenarios are explored. Especially attractive are ELM-free regimes like QH-mode or I-mode scenarios. With the ECE imaging system, the mode structure of related instabilities can be assessed, and a unique feature of mode velocity measurements with the ECE imaging system can be exploited following the same procedure as performed for the low-frequency inter-ELM modes described in this thesis.

Moreover, further analysis in the direction of the mode analysis can include causality relation between high- and low-frequency modes. It has already been indicated with bicoherence analysis that mode coupling is taking place during the inter-ELM cycle. The low-frequency modes appear at the same times as the high-frequency modes, and their lifetime is the same. From here, it is concluded that similar pedestal conditions are responsible for the appearance of both. In the work of Laggner et al. [Laggner et al., 2016], the high-frequency modes are measured on both LFS and HFS hence the ballooning character is not conclusive. On the other hand, the low-frequency modes are measured only on the LFS. Furthermore, both modes appear at established 'critical' pressure gradients.

The ECE Imaging measurements can be mapped one-to-one to the output of the non-linear MHD code JOREK. This is of the significant advantage as the results can be directly compared and visualized in the same manner. Hence, as the complete ELM cycle has not been modeled with JOREK yet, the direct comparison between modeling and experiment opens up a whole new topic.

Furthermore, the existence of an island in the pedestal top during the inter-ELM phase has been suggested in chapter 6, as a possible explanation of the nature of the low-frequency mode. To probe an island in the pedestal top, CECE and thermal He beam measurements could be used for phase measurements of both density and temperature simultaneously.

While this work has demonstrated how the unique capabilities of the ECE imaging system in combination with careful diagnostic forward modeling as well as other edge diagnostics can be used to characterize the pedestal, it has also brought up several suggestions to improve the diagnostics and to extend such investigations as a contribution to other plasma scenarios. In combination with non-linear modeling, this is a promising path towards a quantitative description of pedestal transport.

# Bibliography

- [ASDEX Upgrade web page, ] ASDEX Upgrade web page. Magnetic measurements.
- [Ayub et al., 2017] Ayub, M. K., Yun, G. S., Lee, W., and Park, H. K. (2017). Interpretation of the electron cyclotron emission signal from optically marginal plasmas. *Journal of the Korean Physical Society*, 70(3):268–275.
- [Baylor et al., 2013] Baylor, L. R., Commaux, N., Jernigan, T. C., Brooks, N. H., Combs, S. K., Evans, T. E., Fenstermacher, M. E., Isler, R. C., Lasnier, C. J., Meitner, S. J., Moyer, R. A., Osborne, T. H., Parks, P. B., Snyder, P. B., Strait, E. J., Unterberg, E. A., and Loarte, A. (2013). Reduction of edge-localized mode intensity using high-repetition-rate pellet injection in tokamak H-mode plasmas. *Phys. Rev. Lett.*, 110:245001.
- [Bickerton et al., 1971] Bickerton, R. J., Connor, J. W., and Taylor, J. B. (1971). Diffusion driven plasma currents and bootstrap tokamak. *Nature Physical Science*, 229(4):110–112.
- [Biglari et al., 1990] Biglari, H., Diamond, P. H., and Terry, P. W. (1990). Influence of sheared poloidal rotation on edge turbulence. *Physics of Fluids B: Plasma Physics*, 2(1):1–4.
- [Bolzonella et al., 2004] Bolzonella, T., Zohm, H., Maraschek, M., Martinez, E., Saarelma, S., Günter, S., and Upgrade Team, A. (2004). High frequency MHD activity related to type I ELMs in ASDEX Upgrade. *Plasma Physics and Controlled Fusion*, 46(5A):A143.
- [Boom et al., 2011] Boom, J., Classen, I., de Vries, P., Eich, T., Wolfrum, E., Suttrop, W., Wenninger, R., Donné, A., Tobias, B., Domier, C., Jr, N. L., Park, H., and the ASDEX Upgrade Team (2011). 2D ECE measurements of type-I edge localized modes at ASDEX Upgrade. *Nuclear Fusion*, 51(10):103039.
- [Bornatici et al., 1983] Bornatici, M., Cano, R., Barbieri, O. D., and Engelmann, F. (1983). Electron cyclotron emission and absorption in fusion plasmas. *Nuclear Fusion*, 23(9):1153.

- [Burckhart et al., 2010] Burckhart, A., Wolfrum, E., Fischer, R., Lackner, K., Zohm, H., and the ASDEX Upgrade Team (2010). Inter-ELM behaviour of the electron density and temperature pedestal in ASDEX Upgrade. *Plasma Physics and Controlled Fusion*, 52(10):105010.
- [Burrell et al., 2016] Burrell, K. H., Barada, K., Chen, X., Garofalo, A. M., Groebner, R. J., Muscatello, C. M., Osborne, T. H., Petty, C. C., Rhodes, T. L., Snyder, P. B., Solomon, W. M., Yan, Z., and Zeng, L. (2016). Discovery of stationary operation of quiescent H-mode plasmas with net-zero neutral beam injection torque and high energy confinement on DIII-D. *Physics of Plasmas*, 23(5):056103.
- [Carthy, 2012] Carthy, P. J. M. (2012). Identification of edge-localized moments of the current density profile in a tokamak equilibrium from external magnetic measurements. *Plasma Physics and Controlled Fusion*, 54(1):015010.
- [Cavedon et al., 2017] Cavedon, M., Pütterich, T., Viezzer, E., Dux, R., Geiger, B., McDermott, R. M., Meyer, H., and Stroth, U. (2017). A fast edge charge exchange recombination spectroscopy system at the ASDEX Upgrade tokamak. *Review of Scientific Instruments*, 88(4):043103.
- [Chankin et al., 2007] Chankin, A., Coster, D., Asakura, N., Bonnin, X., Conway, G., Corrigan, G., Erements, S., Fundamenski, W., Horacek, J., Kallenbach, A., Kaufmann, M., Konz, C., Lackner, K., Müller, H., Neuhauser, J., Pitts, R., and Wischmeier, M. (2007). Discrepancy between modelled and measured radial electric fields in the scrape-off layer of divertor tokamaks: a challenge for 2d fluid codes? *Nuclear Fusion*, 47(5):479.
- [Chen, 1984] Chen, F. (1984). *Introduction to Plasma Physics and Controlled Fusion*. Number Bd. 1 in Introduction to Plasma Physics and Controlled Fusion. Springer.
- [Clark, 1983] Clark, W. H. M. (1983). The precision of electron cyclotron emission measurements from a tokamak. *Plasma Physics*, 25(12):1501.
- [Classen, 2007] Classen, I. (2007). *Imaging and control of magnetic islands in tokamaks*. Phd, Eindhoven University of Technology, Eindhoven, Netherlands.
- [Classen et al., 2013] Classen, I., Boom, J., Bogomolov, A., Wolfrum, E., Maraschek, M., Suttrop, W., de Vries, P., Donné, A., Tobias, B., Domier, C., Luhmann, N., and the ASDEX Upgrade Team (2013). The role of temperature fluctuations in the dynamics of type-i and type-ii edge localized modes at asdex upgrade. *Nuclear Fusion*, 53(7):073005.
- [Classen et al., 2010] Classen, I. G. J., Boom, J. E., Suttrop, W., Schmid, E., Tobias, B., Domier, C. W., Luhmann, N. C., Donné, A. J. H., Jaspers, R. J. E., de Vries, P. C., Park, H. K., Munsat, T., García-Muñoz, M., and Schneider, P. A. (2010).

- 2d electron cyclotron emission imaging at asdex upgrade (invited). *Review of Scientific Instruments*, 81(10):10D929.
- [Classen et al., 2014] Classen, I. G. J., Domier, C. W., Jr., N. C. L., Bogomolov, A. V., Suttrop, W., Boom, J. E., Tobias, B. J., and Donné, A. J. H. (2014). Dual array 3D electron cyclotron emission imaging at ASDEX upgrade. *Review of Scientific Instruments*, 85(11):11D833.
- [Colton et al., 1996] Colton, A. L., Buttery, R. J., Fielding, S. J., Gates, D. A., Hender, T. C., Hugill, J., Morris, A. W., Valovic, M., the COMPASS-D, and teams, E. (1996). ELM studies on the COMPASS-D tokamak. *Plasma Physics and Controlled Fusion*, 38(8):1359.
- [Conner and Wilson, 1994] Conner, J. W. and Wilson, H. R. (1994). Survey of theories of anomalous transport. *Plasma Physics and Controlled Fusion*, 36(5):719.
- [Coronado and Wobig, 1992] Coronado, M. and Wobig, H. (1992). On the definition of Pfirsch-Schlüter and bootstrap currents in toroidal systems. *Physics of Fluids B: Plasma Physics*, 4(5):1294–1300.
- [Costley et al., 1974] Costley, A. E., Hastie, R. J., Paul, J. W. M., and Chamberlain, J. (1974). Electron cyclotron emission from a tokamak plasma: Experiment and theory. *Phys. Rev. Lett.*, 33:758–761.
- [Denk et al., 2017] Denk, S. S., Fischer, R., Maj, O., Poli, E., Willensdorfer, M., Stober, J., Stroth, U., Suttrop, W., et al. (2017). Shine-through in electron cyclotron emission measurements. In *44<sup>th</sup> EPS Conference on Plasma Physics*. Proceedings of the 44<sup>th</sup> EPS Conference on Plasma Physics.
- [Denk, S. S. et al., 2017] Denk, S. S., Fischer, Rainer, Maj, Omar, Poli, Emanuele, Stober, Jorg K., Stroth, Ulrich, Vanovac, Branka, Suttrop, Wolfgang, Willensdorfer, Matthias, and ASDEX Upgrade Team (2017). Radiation transport modelling for the interpretation of oblique ECE measurements. *EPJ Web Conf.*, 147:02002.
- [Diallo et al., 2015] Diallo, A., Groebner, R. J., Rhodes, T. L., Battaglia, D. J., Smith, D. R., Osborne, T. H., Canik, J. M., Guttenfelder, W., and Snyder, P. B. (2015). Correlations between quasi-coherent fluctuations and the pedestal evolution during the inter-edge localized modes phase on DIII-D. *Physics of Plasmas*, 22(5):056111.
- [Dickinson et al., 2012] Dickinson, D., Roach, C. M., Saarelma, S., Scannell, R., Kirk, A., and Wilson, H. R. (2012). Kinetic instabilities that limit  $\beta$  in the edge of a tokamak plasma: A picture of an H-mode pedestal. *Phys. Rev. Lett.*, 108:135002.
- [Dickinson et al., 2013] Dickinson, D., Roach, C. M., Saarelma, S., Scannell, R., Kirk, A., and Wilson, H. R. (2013). Microtearing modes at the top of the pedestal. *Plasma Physics and Controlled Fusion*, 55(7):074006.

- [Dickinson et al., 2011] Dickinson, D., Saarelma, S., Scannell, R., Kirk, A., Roach, C. M., and Wilson, H. R. (2011). Towards the construction of a model to describe the inter-ELM evolution of the pedestal on MAST. *Plasma Physics and Controlled Fusion*, 53(11):115010.
- [Eddington, 1920] Eddington, A. S. (1920). The internal constitution of the stars. *The Scientific Monthly*, 11(4):297–303.
- [EUROfusion, 2011] EUROfusion (2011). Figure of tokamak principle.
- [F. Romanelli, 2015] F. Romanelli, a. a. (2015). Overview of the jet results. *Nuclear Fusion*, 55(10):104001.
- [Fischer et al., 2010] Fischer, R., Fuchs, C. J., Kurzan, B., Suttrop, W., Wolfrum, E., and the ASDEX Upgrade Team (2010). Integrated data analysis of profile diagnostics at ASDEX Upgrade. *Fusion Science and Technology*, 58(2):675–684.
- [Fitzpatrick, 1995] Fitzpatrick, R. (1995). Helical temperature perturbations associated with tearing modes in tokamak plasmas. *Physics of Plasmas*, 2(3):825–838.
- [Freethy et al., 2016] Freethy, S. J., Conway, G. D., Classen, I., Creely, A. J., Happel, T., Köhn, A., Vanovac, B., and White, A. E. (2016). Measurement of turbulent electron temperature fluctuations on the ASDEX Upgrade tokamak using correlated electron cyclotron emission. *Review of Scientific Instruments*, 87(11):11E102.
- [Freidberg, 1987] Freidberg, J. (1987). *Ideal magnetohydrodynamics*. Modern Perspectives in Energy Series. Plenum Publishing Company Limited.
- [Frieman et al., 1980] Frieman, E. A., Rewoldt, G., Tang, W. M., and Glasser, A. H. (1980). General theory of kinetic ballooning modes. *The Physics of Fluids*, 23(9):1750–1769.
- [Gernhardt, 1992] Gernhardt, J. (1992). Magnetic diagnostic on ASDEX Upgrade with internal and external pick-up coils. Technical report, Max-Planck-Institut für Plasmaphysik.
- [Gohil et al., 1988] Gohil, P., Ali Mahdavi, M., Lao, L., Burrell, K. H., Chu, M. S., DeBoo, J. C., Hsieh, C. L., Ohya, N., Snider, R. T., Stambaugh, R. D., and Stockdale, R. E. (1988). Study of giant edge-localized modes in DIII-D and comparison with ballooning theory. *Phys. Rev. Lett.*, 61:1603–1606.
- [Griener et al., 2018] Griener, M., noz Burgos, J. M. M., Cavedon, M., Birkenmeier, G., Dux, R., Kurzan, B., Schmitz, O., Sieglin, B., Stroth, U., Viezzer, E., Wolfrum, E., and the ASDEX Upgrade Team (2018). Qualification and implementation of line ratio spectroscopy on helium as plasma edge diagnostic at ASDEX Upgrade. *Plasma Physics and Controlled Fusion*, 60(2):025008.

- [H. Meyer, 2013] H. Meyer, e. a. (2013). Overview of physics results from MAST towards ITER/DEMO and the MAST Upgrade. *Nuclear Fusion*, 53(10):104008.
- [Hartfuss et al., 1997] Hartfuss, H. J., Geist, T., and Hirsch, M. (1997). Heterodyne methods in millimetre wave plasma diagnostics with applications to ECE, interferometry and reflectometry. *Plasma Physics and Controlled Fusion*, 39(11):1693.
- [Hoelzl, 2010] Hoelzl, M. (2010). *Diffusive Heat Transport across Magnetic Islands and Stochastic Layers in Tokamaks*. Dissertation, Technische Universität München, München.
- [Höelzl et al., 2018] Höelzl, M., Huijsmans, G., Orain, F., Artola, F., Pamela, S., Becoulet, M., van Vugt, D., Liu, F., Futatani, S., Lessig, A., Wolfrum, E., Mink, F., Trier, E., Dunne, M., Viezzer, E., Eich, T., Vanovac, B., Frassinetti, L., Guenter, S., Lackner, K., and Krebs, I. a. (2018). Insights into type-I edge localized modes and edge localized mode control from JOREK non-linear magneto-hydrodynamic simulations. *Contributions to Plasma Physics*, 0(0).
- [Höelzl et al., 2012] Höelzl, M., Merkel, P., Huysmans, G. T. A., Nardon, E., Strumberger, E., McAdams, R., Chapman, I., Günter, S., and Lackner, K. (2012). Coupling JOREK and STARWALL codes for non-linear resistive-wall simulations. *Journal of Physics: Conference Series*, 401(1):012010.
- [Hu et al., 2015] Hu, J. S., Sun, Z., Guo, H. Y., Li, J. G., Wan, B. N., Wang, H. Q., Ding, S. Y., Xu, G. S., Liang, Y. F., Mansfield, D. K., Maingi, R., Zou, X. L., Wang, L., Ren, J., Zuo, G. Z., Zhang, L., Duan, Y. M., Shi, T. H., Hu, L. Q., and team, E. (2015). New steady-state quiescent high-confinement plasma in an experimental advanced superconducting tokamak. *Phys. Rev. Lett.*, 114:055001.
- [Huysmans and Czarny, 2007] Huysmans, G. and Czarny, O. (2007). MHD stability in X-point geometry: simulation of ELMs. *Nuclear Fusion*, 47(7):659.
- [I. B. Bernstein, 1958] I. B. Bernstein, E. A. Frieman, M. D. K. R. M. K. (1958). An energy principle for hydromagnetic stability problems. *Proceedings of the Royal Society of London A: Mathematical, Physical and Engineering Sciences*, 244(1236):17–40.
- [International Energy Agency, 2017] International Energy Agency (2017). *World Energy Outlook 2017*.
- [ITER Physics Basis Editors et al., 1999] ITER Physics Basis Editors, Chairs, I. P. E. G., Co-Chairs, Team, I. J. C., and Unit, P. I. (1999). Chapter 1: Overview and summary. *Nuclear Fusion*, 39(12):2137.
- [J W Connor, 1998] J W Connor (1998). Edge-localized modes - physics and theory. *Plasma Physics and Controlled Fusion*, 40(5):531.



- [Jiang et al., 2013] Jiang, M., Shi, Z. B., Che, S., Domier, C. W., Luhmann, N. C., Hu, X., Spear, A., Liu, Z. T., Ding, X. T., Li, J., Zhong, W. L., Chen, W., Che, Y. L., Fu, B. Z., Cui, Z. Y., Sun, P., Liu, Y., Yang, Q. W., and Duan, X. R. (2013). Development of electron cyclotron emission imaging system on the hl-2a tokamak. *Review of Scientific Instruments*, 84(11):113501.
- [Kallenbach et al., 2001] Kallenbach, A., Carlson, A., Pautasso, G., Peeters, A., Seidel, U., and Zehrfeld, H.-P. (2001). Electric currents in the scrape-off layer in ASDEX Upgrade. *Journal of Nuclear Materials*, 290-293(Supplement C):639 – 643. 14th Int. Conf. on Plasma-Surface Interactions in Controlled Fusion Devices.
- [Keilhacker, 1987] Keilhacker, M. (1987). H-mode confinement in tokamaks. *Plasma Physics and Controlled Fusion*, 29(10A):1401.
- [Kim et al., 2015] Kim, M., Lee, J., Park, H., Yun, G., Lee, W., Domier, C., Jr., L. N., and team, K. (2015). Multimode excitation during the inter-ELM-crash periods in KSTAR H-mode plasma. *Nuclear Fusion*, 55(7):073001.
- [Kosłowski et al., 2005] Kosłowski, H., Alper, B., Borba, D., Eich, T., Sharapov, S., Perez, C., Westerhof, E., and contributors, J.-E. (2005). Observation of the palm tree mode, a new MHD mode excited by type-I ELMs on JET. *Nuclear Fusion*, 45(3):201.
- [Krebs et al., 2013] Krebs, I., Hölzl, M., Lackner, K., and Günter, S. (2013). Nonlinear excitation of low-n harmonics in reduced magnetohydrodynamic simulations of edge-localized modes. *Physics of Plasmas*, 20(8):082506.
- [Kurzan and Murmann, 2011] Kurzan, B. and Murmann, H. D. (2011). Edge and core thomson scattering systems and their calibration on the ASDEX Upgrade tokamak. *Review of Scientific Instruments*, 82(10):103501.
- [Laggner et al., 2017] Laggner, F. M., Wolfrum, E., Cavedon, M., Mink, F., Bernert, M., Dunne, M. G., Schneider, P. A., Kappatou, A., Birkenmeier, G., Fischer, R., Willensdorfer, M., and Aumayr, F. (2017). Pedestal structure and inter-ELM evolution for different main ion species in ASDEX upgrade. *Physics of Plasmas*, 24(5):056105.
- [Laggner et al., 2016] Laggner, F. M., Wolfrum, E., Cavedon, M., Mink, F., Viezzer, E., Dunne, M. G., Manz, P., Doerk, H., Birkenmeier, G., Fischer, R., Fietz, S., Maraschek, M., Willensdorfer, M., Aumayr, F., the EUROfusion MST1 Team, and the ASDEX Upgrade Team (2016). High frequency magnetic fluctuations correlated with the inter-ELM pedestal evolution in ASDEX upgrade. *Plasma Physics and Controlled Fusion*, 58(6):065005.
- [Lawson, 1957] Lawson, J. D. (1957). Some criteria for a power producing thermonuclear reactor. *Proceedings of the Physical Society. Section B*, 70(1):6.

- [Leonard, 2014] Leonard, A. W. (2014). Edge-localized-modes in tokamaks. *Physics of Plasmas*, 21(9):090501.
- [Loarte et al., 2007] Loarte, A., Saibene, G., Sartori, R., Riccardo, V., Andrew, P., Paley, J., Fundamenski, W., Eich, T., Herrmann, A., Pautasso, G., Kirk, A., Counsell, G., Federici, G., Strohmayer, G., Whyte, D., Leonard, A., Pitts, R. A., Landman, I., Bazylev, B., and Pestchanyi, S. (2007). Transient heat loads in current fusion experiments, extrapolation to iter and consequences for its operation. *Physica Scripta*, 2007(T128):222.
- [Maggi, 2010] Maggi, C. (2010). Progress in understanding the physics of the H-mode pedestal and ELM dynamics. *Nuclear Fusion*, 50(6):066001.
- [Maggi et al., 2007] Maggi, C., Groebner, R., Oyama, N., Sartori, R., Horton, L., Sips, A., Suttrop, W., the ASDEX Upgrade Team, Leonard, A., Luce, T., Wade, M., the DIII-D Team, Kamada, Y., Urano, H., the JT-60U Team, Andrew, Y., Giroud, C., Joffrin, E., de la Luna, E., for the Pedestal, E.-J. C., Physics, E., and the Steady State Operation Topical Groups of the ITPA (2007). Characteristics of the H-mode pedestal in improved confinement scenarios in ASDEX Upgrade, DIII-D, JET and JT-60U. *Nuclear Fusion*, 47(7):535.
- [Manz et al., 2014] Manz, P., Boom, J. E., Wolfrum, E., Birkenmeier, G., Classen, I. G. J., Jr, N. C. L., Stroth, U., and the ASDEX Upgrade Team (2014). Velocimetry analysis of type-I edge localized mode precursors in ASDEX upgrade. *Plasma Physics and Controlled Fusion*, 56(3):035010.
- [Martin et al., 2008] Martin, Y. R., Takizuka, T., and the ITPA CDBM H-mode Threshold Database Working Group (2008). Power requirement for accessing the H-mode in ITER. *Journal of Physics: Conference Series*, 123(1):012033.
- [Mink et al., 2018] Mink, A., Hoelzl, M., Wolfrum, E., Orain, F., Dunne, M., Lessig, A., Pamela, S., Manz, P., Maraschek, M., Huijsmans, G., Becoulet, M., Laggner, F., Cavedon, M., Lackner, K., Günter, S., Stroth, U., and Team, T. A. U. (2018). Nonlinear coupling induced toroidal structure of edge localized modes. *Nuclear Fusion*, 58(2):026011.
- [Mink, 2018] Mink, A. F. (2018). *Structure and Nonlinear Development of Edge Localized Magnetohydrodynamic Instabilities on the ASDEX Upgrade Tokamak*. Dissertation, Technische Universität München.
- [Mink et al., 2016] Mink, F., Wolfrum, E., Maraschek, M., Zohm, H., Horvath, L., Laggner, F. M., Manz, P., Viezzer, E., Stroth, U., and the ASDEX Upgrade Team (2016). Toroidal mode number determination of ELM associated phenomena on ASDEX upgrade. *Plasma Physics and Controlled Fusion*, 58(12):125013.

- [N. C. Luhmann Jr. et al., 2008] N. C. Luhmann Jr., Bindslev, H., Park, H., Sánchez, J., Taylor, G., and Yu, C. X. (2008). Chapter 3: Microwave diagnostics. *Fusion Science and Technology*, 53(2):335–396.
- [Orain et al., 2013] Orain, F., Bécoulet, M., Dif-Pradalier, G., Huijsmans, G., Pamela, S., Nardon, E., Passeron, C., Latu, G., Grandgirard, V., Fil, A., Ratnani, A., Chapman, I., Kirk, A., Thornton, A., Hoelzl, M., and Cahyna, P. (2013). Non-linear magnetohydrodynamic modeling of plasma response to resonant magnetic perturbations. *Physics of Plasmas*, 20(10):102510.
- [Perez et al., 2004a] Perez, C., Koslowski, H., Huysmans, G., Hender, T., Smeulders, P., Alper, B., de la Luna, E., Hastie, R., Meneses, L., Nave, M., Parail, V., Zerbini, M., and Contributors, J.-E. (2004a). Type-I ELM precursor modes in JET. *Nuclear Fusion*, 44(5):609.
- [Perez et al., 2004b] Perez, C. P., Koslowski, H. R., Hender, T. C., Smeulders, P., Loarte, A., Lomas, P. J., Saibene, G., Sartori, R., Becoulet, M., Eich, T., Hastie, R. J., Huysmans, G. T. A., Jachmich, S., Rogister, A., Schüller, F. C., and contributors, J. E. (2004b). Washboard modes as ELM-related events in JET. *Plasma Physics and Controlled Fusion*, 46(1):61.
- [Pitcher et al., 1997] Pitcher, C. S., Herrmann, A., Murmann, H., Reimerdes, H., Schweinzer, J., Suttrop, W., Salzmann, H., the ASDEX Upgrade Team, and the NBI Group (1997). Heat transport at the boundary of asdex upgrade. *Plasma Physics and Controlled Fusion*, 39(7):1129.
- [Pütterich et al., 2011] Pütterich, T., Dux, R., Janzer, M., and McDermott, R. (2011). Elm flushing and impurity transport in the h-mode edge barrier in asdex upgrade. *Journal of Nuclear Materials*, 415(1, Supplement):S334 – S339. Proceedings of the 19th International Conference on Plasma-Surface Interactions in Controlled Fusion.
- [Rathgeber et al., 2013] Rathgeber, S. K., Barrera, L., Eich, T., Fischer, R., Nold, B., Suttrop, W., Willensdorfer, M., Wolfrum, E., and the ASDEX Upgrade Team (2013). Estimation of edge electron temperature profiles via forward modelling of the electron cyclotron radiation transport at ASDEX Upgrade. *Plasma Physics and Controlled Fusion*, 55(2):025004.
- [Ryter et al., 2009] Ryter, F., Pütterich, T., Reich, M., Scarabosio, A., Wolfrum, E., Fischer, R., Adamov, M. G., Hicks, N., Kurzan, B., Maggi, C., Neu, R., Rohde, V., Tardini, G., and the ASDEX Upgrade TEAM (2009). H-mode threshold and confinement in helium and deuterium in ASDEX Upgrade. *Nuclear Fusion*, 49(6):062003.
- [S. Coda, 2017] S. Coda, e. a. (2017). Overview of the TCV tokamak program: scientific progress and facility upgrades. *Nuclear Fusion*, 57(10):102011.

- [Saarelma et al., 2013] Saarelma, S., Beurskens, M., Dickinson, D., Frassinetti, L., Leyland, M., Roach, C., and Contributors, E.-J. (2013). MHD and gyro-kinetic stability of JET pedestals. *Nuclear Fusion*, 53(12):123012.
- [Saarelma et al., 2017] Saarelma, S., Martin-Collar, J., Dickinson, D., McMillan, B. F., Roach, C. M., team1, M., and Contributors4, T. J. (2017). Non-local effects on pedestal kinetic ballooning mode stability. *Plasma Physics and Controlled Fusion*, 59(6):064001.
- [Schirmer et al., 2006] Schirmer, J., Conway, G., Zohm, H., Suttrop, W., and the ASDEX Upgrade Team (2006). The radial electric field and its associated shear in the ASDEX Upgrade tokamak. *Nuclear Fusion*, 46(9):S780.
- [Snyder et al., 2011] Snyder, P., Groebner, R., Hughes, J., Osborne, T., Beurskens, M., Leonard, A., Wilson, H., and Xu, X. (2011). A first-principles predictive model of the pedestal height and width: development, testing and iter optimization with the eped model. *Nuclear Fusion*, 51(10):103016.
- [Snyder et al., 2009] Snyder, P. B., Groebner, R. J., Leonard, A. W., Osborne, T. H., and Wilson, H. R. (2009). Development and validation of a predictive model for the pedestal height. *Physics of Plasmas*, 16(5):056118.
- [Snyder et al., 2012] Snyder, P. B., Osborne, T. H., Burrell, K. H., Groebner, R. J., Leonard, A. W., Nazikian, R., Orlov, D. M., Schmitz, O., Wade, M. R., and Wilson, H. R. (2012). The EPED pedestal model and edge localized mode-suppressed regimes: Studies of quiescent H-mode and development of a model for edge localized mode suppression via resonant magnetic perturbations. *Physics of Plasmas*, 19(5):056115.
- [Snyder et al., 2002] Snyder, P. B., Wilson, H. R., Ferron, J. R., Lao, L. L., Leonard, A. W., Osborne, T. H., Turnbull, A. D., Mossessian, D., Murakami, M., and Xu, X. Q. (2002). Edge localized modes and the pedestal: A model based on coupled peeling ballooning modes. *Physics of Plasmas*, 9(5):2037–2043.
- [Spitzer and Harm, 1953] Spitzer, L. and Harm, R. (1953). Transport phenomena in a completely ionized gas. *Physical Review*, 89(5):977–981.
- [Stangeby, 2000] Stangeby, P. (2000). *The Plasma Boundary of Magnetic Fusion Devices*. Series in Plasma Physics and Fluid Dynamics. Taylor & Francis.
- [Streibl et al., 2003] Streibl, B., Lang, P. T., Leuterer, F., Noterdaeme, J.-M., and Stähler, A. (2003). Chapter 2: Machine design, fueling, and heating in ASDEX Upgrade. *Fusion Science and Technology*, 44(3):578–592.
- [Suttrop et al., 1996] Suttrop, W., Büchl, K., de Blank, H. J., Schweinzer, J., Zohm, H., team, A. U., group, N., and group, I. (1996). Characteristics of edge localized modes in ASDEX upgrade. *Plasma Physics and Controlled Fusion*, 38(8):1407.

- [Suttrop et al., 2011] Suttrop, W., Eich, T., Fuchs, J. C., Günter, S., Janzer, A., Herrmann, A., Kallenbach, A., Lang, P. T., Lunt, T., Maraschek, M., McDermott, R. M., Mlynek, A., Pütterich, T., Rott, M., Vierle, T., Wolfrum, E., Yu, Q., Zammuto, I., and Zohm, H. (2011). First observation of edge localized modes mitigation with resonant and nonresonant magnetic perturbations in ASDEX Upgrade. *Phys. Rev. Lett.*, 106:225004.
- [Suttrop and Peeters, 1996] Suttrop, W. and Peeters, A. (1996). Practical limitations to plasma edge electron temperature measurements by radiometry of electron cyclotron emission. *IPP report*.
- [Tang et al., 1980] Tang, W., Connor, J., and Hastie, R. (1980). Kinetic-ballooning-mode theory in general geometry. *Nuclear Fusion*, 20(11):1439.
- [Tobias et al., 2010] Tobias, B., Domier, C. W., Liang, T., Kong, X., Yu, L., Yun, G. S., Park, H. K., Classen, I. G. J., Boom, J. E., Donné, A. J. H., Munsat, T., Nazikian, R., Van Zeeland, M., Boivin, R. L., and Luhmann, N. C. (2010). Commissioning of electron cyclotron emission imaging instrument on the DIII-D tokamak and first data. *Review of Scientific Instruments*, 81(10):10D928.
- [Tobias et al., 2012] Tobias, B. J., Austin, M. E., Boom, J. E., Burrell, K. H., Classen, I. G. J., Domier, C. W., Jr., N. C. L., Nazikian, R., and Snyder, P. B. (2012). ECE-imaging of the H-mode pedestal (invited). *Review of Scientific Instruments*, 83(10):10E329.
- [Told et al., 2008] Told, D., Jenko, F., Xanthopoulos, P., Horton, L. D., and Wolfrum, E. (2008). Gyrokinetic microinstabilities in ASDEX Upgrade edge plasmas. *Physics of Plasmas*, 15(10):102306.
- [Urano, 2014] Urano, H. (2014). Pedestal structure in H-mode plasmas. *Nuclear Fusion*, 54(11):116001.
- [van Milligen et al., 1995] van Milligen, B. P., Hidalgo, C., and Sánchez, E. (1995). Nonlinear phenomena and intermittency in plasma turbulence. *Phys. Rev. Lett.*, 74:395–398.
- [Vanovac et al., 2016] Vanovac, B., Classen, I., Denk, S., Wolfrum, E., Hoelzl, M., Lessig, A., Orain, F., Luhmann, N. C. J., et al. (2016). ELM filaments on ASDEX Upgrade: ECEI observations and modelling. In *43<sup>th</sup> EPS Conference on Plasma Physics*. Proceedings of the 43<sup>th</sup> EPS Conference on Plasma Physics.
- [Vanovac et al., 2018a] Vanovac, B., Denk, S. S., Wolfrum, E., Willensdorfer, M., Suttrop, W., Fischer, R., Luhmann, N. C., and the ASDEX Upgrade team (2018a). Mode analysis limitations of ECEI & ECE measurements at the plasma edge. *20th Joint Workshop on ECE and ECRH, Greifswald, May 14-17, 2018 (to appear on EPJ Web of Conferences)*.

- [Vanovac et al., 2018b] Vanovac, B., Wolfrum, E., Denk, S. S., Mink, F., Laggner, F. M., Birkenmeier, G., Willensdorfer, M., Viezzer, E., Hoelzl, M., Freethy, S. J., Dunne, M. G., Lessig, A., Jr, N. C. L., the ASDEX Upgrade Team, and the EUROfusion MST1 Team (2018b). Effects of density gradients and fluctuations at the plasma edge on ECEI measurements at ASDEX Upgrade. *Plasma Physics and Controlled Fusion*, 60(4):045002.
- [Vanovac et al., 2018c] Vanovac, B., Wolfrum, E., Hoelzl, M., Willensdorfer, M., Cavedon, M., Harrer, G., Mink, F., Denk, S., Freethy, S., Dunne, M., Manz, P., Jr, N. L., and Team, T. A. U. (2018c). Characterization of low-frequency inter-elm modes of H-mode discharges at ASDEX Upgrade. *Nuclear Fusion*, 58(11):112011.
- [Viezzer, 2013] Viezzer, E. (2013). *Radial electric field studies in the plasma edge of ASDEX Upgrade*. PhD thesis, Ludwig-Maximilians-Universität München.
- [Viezzer et al., 2014] Viezzer, E., Pütterich, T., Angioni, C., Bergmann, A., Dux, R., Fable, E., McDermott, R., Stroth, U., Wolfrum, E., and the ASDEX Upgrade Team (2014). Evidence for the neoclassical nature of the radial electric field in the edge transport barrier of ASDEX upgrade. *Nuclear Fusion*, 54(1):012003.
- [Viezzer et al., 2013] Viezzer, E., Putterich, T., Conway, G., Dux, R., Happel, T., Fuchs, J., McDermott, R., Ryter, F., Sieglin, B., Suttrop, W., Willensdorfer, M., Wolfrum, E., and the ASDEX Upgrade Team (2013). High-accuracy characterization of the edge radial electric field at ASDEX Upgrade. *Nuclear Fusion*, 53(5):053005.
- [Viezzer et al., 2012] Viezzer, E., Pütterich, T., Dux, R., and McDermott, R. M. (2012). High-resolution charge exchange measurements at asdex upgrade. *Review of Scientific Instruments*, 83(10):103501.
- [Wagner et al., 1985] Wagner, F., Bartiromo, R., Becker, G., Bosch, H., Eberhagen, A., Fussmann, G., Gehre, O., Gernhardt, J., Gierke, G., Clock, E., Gruber, O., Haas, G., Janeschitz, G., Karger, F., Keilhacker, M., Kislyakov, A., K"uber, O., Kornherr, M., Kotzé, P., Lackner, K., Lenoci, M., Lisitano, G., Mahdavi, A., Mayer, H.-M., McCormick, K., Meisel, D., Mertens, V., Müller, E., Murmann, H., Niedermeyer, H., Poschenrieder, W., Rapp, H., Ryter, F., Roth, J., Schneider, F., Siller, G., Smeulders, P., Söldner, F., Speth, E., Steinmetz, K., Steuer, K.-H., and Vollmer, O. (1985). Experimental evidence for neoclassical ion transport effects in the H-transition of ASDEX. *Nuclear Fusion*, 25(10):1490.
- [Wagner et al., 1982] Wagner, F., Becker, G., Behringer, K., Campbell, D., Eberhagen, A., Engelhardt, W., Fussmann, G., Gehre, O., Gernhardt, J., Gierke, G. v., Haas, G., Huang, M., Karger, F., Keilhacker, M., Kluber, O., Kornherr, M., Lackner, K., Lisitano, G., Lister, G. G., Mayer, H. M., Meisel, D., Muller, E. R.,

- Murmann, H., Niedermeyer, H., Poschenrieder, W., Rapp, H., Rohr, H., Schneider, F., Siller, G., Speth, E., Stabler, A., Steuer, K. H., Venus, G., Vollmer, O., and Yu, Z. (1982). Regime of improved confinement and high beta in neutral-beam-heated divertor discharges of the ASDEX tokamak. *Phys. Rev. Lett.*, 49:1408–1412.
- [Walk et al., 2014] Walk, J. R., Hughes, J. W., Hubbard, A. E., Terry, J. L., Whyte, D. G., White, A. E., Baek, S. G., Reinke, M. L., Theiler, C., Churchill, R. M., Rice, J. E., Snyder, P. B., Osborne, T., Dominguez, A., and Cziegler, I. (2014). Edge-localized mode avoidance and pedestal structure in I-mode plasmas. *Physics of Plasmas*, 21(5):056103.
- [Wenninger et al., 2013] Wenninger, R., Reimerdes, H., Sauter, O., and Zohm, H. (2013). Non-linear magnetic perturbations during edge-localized modes in TCV dominated by low n mode components. *Nuclear Fusion*, 53(11):113004.
- [Wesson and Campbell, 1997] Wesson, J. and Campbell, D. (1997). *Tokamaks*. Oxford Engineering Science Series. Clarendon Press.
- [Wikipedia contributors, 2018] Wikipedia contributors (2018). Deuterium — Wikipedia, the free encyclopedia. [Online; accessed 26-November-2018].
- [Willensdorfer et al., 2014] Willensdorfer, M., Birkenmeier, G., Fischer, R., Laggner, F. M., Wolfrum, E., Veres, G., Aumayr, F., Carralero, D., Guimaraes, L., Kurzan, B., and the ASDEX Upgrade Team (2014). Characterization of the LIBES at ASDEX upgrade. *Plasma Physics and Controlled Fusion*, 56(2):025008.
- [Willensdorfer et al., 2016] Willensdorfer, M., Denk, S. S., Strumberger, E., Suttrop, W., Vanovac, B., Brida, D., Cavedon, M., Classen, I., Dunne, M., Fietz, S., Fischer, R., Kirk, A., Laggner, F. M., Liu, Y. Q., Odstrcil, T., Ryan, D. A., Viezzer, E., Zohm, H., Luhmann, I. C., Team, T. A. U., and Team, T. E. M. (2016). Plasma response measurements of external magnetic perturbations using electron cyclotron emission and comparisons to 3D ideal MHD equilibrium. *Plasma Physics and Controlled Fusion*, 58(11):114004.
- [Willensdorfer et al., 2012] Willensdorfer, M., Wolfrum, E., Fischer, R., Schweinzer, J., Sertoli, M., Sieglin, B., Veres, G., Aumayr, F., and the ASDEX Upgrade Team (2012). Improved chopping of a lithium beam for plasma edge diagnostic at ASDEX upgrade. *Review of Scientific Instruments*, 83(2).
- [Wolfrum et al., 2015] Wolfrum, E., Viezzer, E., Burckhart, A., Dunne, M., Schneider, P., Willensdorfer, M., Fable, E., Fischer, R., Hatch, D., Jenko, F., Kurzan, B., Manz, P., Rathgeber, S., and the ASDEX Upgrade Team (2015). Overview of recent pedestal studies at ASDEX Upgrade. *Nuclear Fusion*, 55(5):053017.
- [Yu et al., 2012] Yu, L., Domier, C. W., Kong, X., Che, S., Tobias, B., Park, H., Yu, C. X., and Jr, N. C. L. (2012). Recent advances in ECE imaging performance. *Journal of Instrumentation*, 7(02):C02055.

- [Yun et al., 2014] Yun, G. S., Lee, W., Choi, M. J., Lee, J., Kim, M., Leem, J., Nam, Y., Choe, G. H., Park, H. K., Park, H., Woo, D. S., Kim, K. W., Domier, C. W., Luhmann, N. C., Ito, N., Mase, A., and Lee, S. G. (2014). Quasi 3D ECE imaging system for study of MHD instabilities in KSTAR. *Review of Scientific Instruments*, 85(11):11D820.
- [Zohm, 1996] Zohm, H. (1996). Edge localized modes (ELMs). *Plasma Physics and Controlled Fusion*, 38(2):105.
- [Zohm, 2014] Zohm, H. (2014). *Magnetohydrodynamic Stability of Tokamaks*. Wiley.
- [Zohm et al., 2017] Zohm, H., Träuble, F., Biel, W., Fable, E., Kemp, R., Lux, H., Siccino, M., and Wenninger, R. (2017). A stepladder approach to a tokamak fusion power plant. *Nuclear Fusion*, 57(8):086002.





# Acknowledgments

The past four years of my PhD project are very profitable years in terms of my personal growth as a scientist and as a team player. All of it was achievable because of my personal strengths combined with the strengths of amazing people surrounding me professionally and personally. I am grateful to all of you.

I am especially grateful to Elisabeth Wolfrum, my co-promotor, my daily supervisor and my coach who inherited me from the year # 2 of my project. I am enormously grateful for our Monday afternoon meetings where we discussed physics, life and everything else. Her physics expertise, enthusiasm for science and novelty in leadership makes her my role model.

I want to express my gratitude to my promotor Tony Donnè for always finding time for me: be it reading my not-so-well-written chapter or fill in the forms or participate in our frequent progress meetings. My chapters have seen the world travelling with Tony. He was always keeping track of time and making sure I do get my stuff done. Apart from my PhD project he was enormously supportive of me taking part in the NGO activity that promotes fusion in Balkan countries. His overall involvement means a lot for the whole FOM team.

I want to thank to my project leader Marco de Baar, for giving me the opportunity to work on this topic. I also want to express my thanks to Jonathan Citrin, my group leader at DIFFER, for his feedback, comments and interest in my work. Jonathan is always an infinite source of refreshing and great ideas. With Jonathan being on board of our Integrated Modeling and Transport group, with Loes sending me postcards for my birthday every year, Jolanda, Ans and Henk being on board for my email - tax office challenges and travel arrangement questions, it was much easier to keep the connections with my home institute DIFFER.

Coming back to the ASDEX Upgrade ground there are numerous people without whom the work and life would not be complete: I want to thank Matthias Hölzl for all scientific discussions, and all the help he provided me when working with JOREK data. I want to thank Emanuele Poli for helping me with TOREBEAM code at the early stage of my PhD. I want to thank Severin Denk for providing me with his ECFM/ECRad code, however he likes to call it. My entire diagnostic work has a solid ground thanks to Severin's work.

I want to thank the ECE team: Simon Freethy, Matthias Willendsorfer and Wolfgang Suttrop for all the ideas and knowledge shared with me about the workflow of the ECE diagnostic; for all the smart questions and comments that largely improved my understanding and performance as a microwave diagnostician.

I want to thank reflectometry people - Luis Guimaraes and Garrard Conway for providing me with the necessary diagnostic tools when needed.

I want to thank Hendrik Mayer for his colorful comments and suggestions that improved my first ever paper significantly. My big thank you goes to Gabriele Dörch. Following Lisl's idea, Gabi provided me with an escape office where I had my solitude while writing this thesis. She even made sure that I do not have any neighbours to be distracted from. I want to thank Ana Kostić for being there for me at any point in time and space. Thank you for cracking down pedestal puzzles, human behaviour and what not with me throughout our PhD road.

I want to thank my friends from far away: Vladica Nikolić, Ioana Arapoglou, Camila de Conto, Jovana Simšić, Tijana Čevriz, Danka Gavrilović, Petar Kostić, Tijana Randjelović, Dušan Randjelović for all your rational and advices when I needed them.

I want to thank the ladies - AUG productions 'senior' team: Rachael McDermott, Athina Kappatou, Sina Fietz, Eleonora Viezzer for all the fun time while making Christmas musicals.

I want to thank Sola Volta members: Till Sehmer (drums), Chris Rapson (base), Dario de Michela (keyboard), Florian Penzel (guitar). Our Thursday evenings after work are so valuable to me. It was a vent of emotions and creativity. Our music sessions in the music room showed me the teamwork behind making music: from an idea to a fully developed album that we have created in less than a year.

I want to thank FOM team - Ana Kostić, Miloš Vlainić, Vladica Nikolić, Maša

Šćepanović for all the great ideas and our workshops. My engagement in FOM thought me what to focus on when working in a team with friends, how not to take things personally, how to digest critics, how to write a project proposal, how to better read legal documents, how to write efficient to-the-point emails, how to organize a summer school/workshop, how to appreciate enthusiasm of others.

I want to thank Andreas Burkhart, Dr Schneider, Athina Kappatou, Rachael McDermott, Alex Bock, George Harrer, Ondrej Kudlacek, Filip Janky, Thomas Hayward-Schneider, Felician Mink, Matthias Bernet, Mike Dunne, Marco Cavedon, Thilmann Lunt, Michael Faitsch, Vitali Brack, Tim Oppermann, Matthias Kahl for pleasant coffee times, food times, cinema times, cycling times, music times, skiing times, swimming in-the-lake-during-lunch times, moving-houses times.

My enormous gratitude goes to my parents who in reality do not have much to do with my PhD but rather are my giants who helped me climb the ladder towards starting it. Thank you for being so supportive and non-judgemental.

I want to thank Michael Faitsch for stepping into my life. Finishing up my thesis work is kind of a soft landing with you.



# Curriculum Vitae

I was born on 16<sup>th</sup> of February 1986 in the city of Zenica in Bosnia and Herzegovina. In 2005 I graduated from Gymnasium Ivo Andrić in Višegrad. In 2011 I obtained my physics diploma at University Novi Sad in Serbia, at the Faculty of Natural Sciences. During my Bachelor studies, I spent one year at Università degli Studi di Trento in Italy as a part of the student exchange program.

I continued my education in science and engineering by entering the Joint European Master in Nuclear Fusion Science and Engineering Physics (FUSION-EP) for which I was awarded an Erasmus Mundus Scholarship.

My PhD at DIFFER starts on 1<sup>st</sup> of January 2015. For the entire duration of my contract, I am a guest researcher at Max Planck Institute of Plasma Physics in Garching, Germany where I conducted the experiments and performed the analysis that are summarized in this dissertation.



# List of publications

## Journal articles

First author:

- B Vanovac et al, *Effects of density gradients and fluctuations at the plasma edge on ECEI measurements at ASDEX Upgrade*, 2018 Plasma Phys. Control. Fusion 60 045002
- B Vanovac et al, *Characterization of low-frequency inter-ELM modes at the pedestal top of H-mode discharges at ASDEX Upgrade*, 2018 Nucl. Fusion 58 11201
- B Vanovac et al, *Mode analysis limitations of ECEI and ECE measurements at the plasma edge*, submitted to EPJ Web of Conferences

Co-author

- M Hoelzl et al, *Insights into type-I edge localized modes and edge localized mode control from JOREK non-linear magneto-hydrodynamic simulations*, Contribution to Plasma Physics (2018)
- H. Meyer et al, *Overview of progress in European medium sized tokamaks towards an integrated plasma-edge/wall solution*, 2017 Nucl. Fusion 57 102014
- M. Willensdorfer et al, *Field-Line Localized Destabilization of Ballooning Modes in Three-Dimensional Tokamaks*, August 2017 Physical Review Letters 119(8)



- S. S. Denk et al, *Radiation transport modelling for the interpretation of oblique ECE measurements*, EPJ Web of Conferences 147, 02002 (2017)
- M. Willensdorfer et al, *Plasma response measurements of external magnetic perturbations using electron cyclotron emission and comparisons to 3D ideal MHD equilibrium*, 2016 Plasma Phys. Control. Fusion 58 114004
- S. Freethy et al, *Measurement of turbulent electron temperature fluctuations on the ASDEX Upgrade tokamak using correlated electron cyclotron emission*, Review of Scientific Instruments 87, 11E102 (2016)

## Conference contributions

- B. Vanovac *Pedestal modes during the ELM cycle*, FuseNet PhD event, ITER headquarters, France 2019, PechaKucha talk
- B. Vanovac et al, *Effects of the density on ECEI at the plasma edge of ASDEX Upgrade tokamak*, Physics@Veldhoven Conference, Veldhoven, The Netherlands 2018, talk
- B. Vanovac et al, *ECEI and magnetic measurements during inter-ELM mode*, Workshop on H-mode Physics and Transport Barriers, St Petersburg, Russia, Poster A7 (09/2017)
- F. Mink et al, *Influence of plasma parameters onto the toroidal structure of ELM related pedestal modes*, Workshop on H-mode Physics and Transport Barriers, St Petersburg, Russia, Poster A5 (09/2017)
- B. Vanovac et al, *Effects of strong density fluctuations at the plasma edge on ECEI measurements at ASDEX Upgrade*, 44th EPS Conference P4.122, Belfast Northern Ireland 2017
- E. Trier et al, *ELM-induced cold pulses propagation in ASDEX Upgrade*, 44th EPS Conference P1.163, Belfast Northern Ireland 2017

- 
- F. Orain et al, *Interplay between ELMs and resonant magnetic perturbations in ASDEX Upgrade*, WE-Heraeus-Seminar: Impact of 3D Magnetic Fields on Hot Plasmas, Bad Honnef, Germany (05/2017)
  - F. Orain et al, *Modeling edge MHD instabilities and their interaction with Magnetic Perturbations in ASDEX Upgrade*, 44th EPS Conference O4.127, Belfast Northern Ireland 2017
  - B. Vanovac et al, *ELM filaments on ASDEX Upgrade: ECEI observations and modelling*, 43rd EPS Conference P1.014, Leuven Belgium 2016
  - S. Freethy et al, *Measurement of turbulent electron temperature fluctuations on the ASDEX Upgrade tokamak using correlated Electron Cyclotron Emission*, 43rd EPS Conference P1.024, Leuven Belgium 2016
  - B. Vanovac et al, *Edge temperature fluctuation measurements with the upgraded ECEI diagnostics on ASDEX Upgrade*, Physics@FOM Conference, Veldhoven, The Netherlands 2016
  - S. Freethy et al, *Development progress of Correlation ECE and n-T cross-phase angle diagnostics for ASDEX Upgrade*, PS Division of Plasma Physics Meeting 2015
  - B. Vanovac et al, *3D edge temperature fluctuation measurements with upgraded ECEI diagnostic on ASDEX Upgrade*, FuseNet PhD event, Prague, 2016
  - I. Classen et al, *3D ELM fluctuation measurements with the new dual array ECE-Imaging diagnostic on ASDEX Upgrade*, PS Division of Plasma Physics Meeting 2015